

Collegio di Ingegneria Energetica

Master of Science Course in Energy and Nuclear Engineering



Master of Science Thesis

CERAMIC COATINGS FOR SOCs INTERCONNECTS
PROCESSED BY ELECTROPHORETIC DEPOSITION:
ELECTRICAL CHARACTERIZATION

Tutor:
Federico Smeacetto

Candidate:
Riccardo Presta

March 2021

Alla mia famiglia, in particolare ai miei piccoli

Preface

This work is based on the experiments I performed from October 2020 to March 2021 in Politecnico di Torino, supported by Elisa Zanchi and headed and supervised by Prof. Federico Smeacetto.

The thesis is a joint research among Politecnico di Torino, Gdansk University of Technology. The samples production and the experimental characterizations were carried out by at POLITO, afterwards characterizations were partially performed in Gdansk under the supervision of Prof. Sebastian Molin. Transmission electron microscopy characterization was conducted by Dr. Gregorz Cempura in the International Centre of Electron Microscopy for Materials Science at University of Science and Technology – AGH in Krakow.

Further experiments could assess the long-term effects of EPD deposited protective coatings on the overall efficiency.



Abstract

The integration of renewable energy (RE) sources in the power system is a key strategy to reduce fossil fuel consumption and promote the transition towards a sustainable energy system. To this purpose, hydrogen as energy vector will be a key instrument for meeting the EU Green Deal objectives.

In this context, solid oxide cells (SOCs) are promising electrochemical devices for the conversion of chemical energy into electrical energy and vice versa. Solid oxide cells devices are of great interest for efficient and clean power generation and for highly efficient conversion of electricity to hydrogen, fuels and chemicals using high temperature electrolysis. High-performance advanced ceramic materials are at the core of the technological innovations needed to reach a sustainable and climate-neutral economy and society.

Due to working temperature between 650-850 °C, ferritic stainless steels are the most widely used for interconnects (IC) in SOC technology. At high oxygen partial pressures and in the presence of steam, volatile chromium species form, $CrO_2(OH)_2$, thus poisoning the electrochemical activity with detrimental consequences on the SOC performance.

Manganese-cobalt based spinels are the widest commercial solution, used as a protective coating due to their thermomechanical compatibility with IC and high electric conductivity. These ceramic-based coatings are used to protect metallic IC from oxidation and to limit chromium release and poisoning of the oxygen electrode; both effects can compromise the durability and the efficiency of the SOC stack. The doping of MnCo spinels with transition metals (*Fe* and *Cu*) has been previously evaluated as an interesting approach to obtain modification of electric and thermomechanical properties of the manganese cobaltite pure spinels.

This work focuses on iron and copper doped *MnCo* based coatings, deposited by electrophoretic deposition method. The steel considered is CROFER 22 APU. Samples of four different compositions were produced by electrophoretic co-deposition of $Mn_{1,5}Co_{1,5}O_4$, Fe_2O_3 and CuO in different amounts. As deposited samples were sintered in reductive and oxidizing atmosphere in a two-step heat treatment, obtaining a dense and compact coating. After each step XRD and SEM analyzes were carried out, in order to verify properties of each deposition. Oxidation kinetics were tested on each coating by thermogravimetric test, at 750 °C for 1000 h. The mass gain was monitored over time to assess the oxygen uptake caused by metal oxidation. TEM-SAED characterization was carried out on $5Fe5CuMCO$ and $10Fe10CuMCO$ samples at AGH University of Science and Technology, in Krakow. In parallel, pellets of different compositions of *Cu* and *Fe* doped MCO were produced by pressing pre-sintered powders, then sintered again to obtain a dense and uniform material. Pellets were used for dilatometric measurements, to investigate the effect of doping on the thermomechanical properties; doped samples did not exhibit the cubic to tetragonal transition. High *Cu* concentration leads to a higher CTE, while *Fe* has the opposite effect.

The research findings reported in the MSc thesis demonstrated the feasibility of achieving a mixed spinel structure by a fast and low cost production method. Coatings obtained were dense, stable and had shown compatible thermomechanical properties with CROFER 22 APU. Thus, they were performant in reducing oxygen partial pressure on the scale. By properly balancing the microstructural, thermomechanical and electrical properties of *Cu* and *Fe* doped spinels it will be possible to further optimize EPD deposited ceramic obtaining the proper functional requirements.



Contents

1	Introduction	1
1.1	Solid Oxide Cells	6
1.1.1	Electrolyte	11
1.1.2	Fuel electrode	11
1.1.3	Oxygen electrode	11
1.1.4	Interconnect	12
1.2	Work Overview	13
1.2.1	The interconnect corrosion problem	13
1.2.2	Thesis outline	13
1.3	Experimental methods	15
1.3.1	Electrophoretic deposition	15
1.3.2	Sintering	17
1.3.3	Thermogravimetric test	18
1.3.4	ASR test	22
2	Experimental	24
2.1	Samples preparation	24
2.1.1	Preliminary deposition experiments -EPD parameters and morphological and compositional characterization	25
2.1.2	Optimized deposition experiments	27
2.2	Pellets preparation	29
3	Results and discussion	30
3.1	Dilatometry	30
3.2	X-Ray diffraction	34
3.3	SEM	36
3.4	Characterization of as-sintered coating by transmission electron microscopy . .	42
3.5	Thermogravimetric test	43
3.6	ASR test	45
3.7	Post-mortem microstructural characterization	50
4	Conclusions and future perspectives	53
5	Bibliography	55

List of Acronyms

10Fe10CuMCO	Manganese cobalt spinel doped with 10 wt.% of Fe and 10 wt.% of Cu
10Fe5CuMCO	Manganese cobalt spinel doped with 10 wt.% of Fe and 5 wt.% of Cu
10CuMCO	Manganese cobalt spinel doped with 10 wt.% of Cu
10FeMCO	Manganese cobalt spinel doped with 10 wt.% of Fe
5Fe5CuMCO	Manganese cobalt spinel doped with 5 wt.% of Fe and 5 wt.% of Cu
5Fe10CuMCO	Manganese cobalt spinel doped with 5 wt.% of Fe and 10 wt.% of Cu
ASR	Area specific resistance
CCS	Carbon capture and sequestration
CTE	Coefficient of thermal expansion
EPD	Electrophoretic deposition
FSS	Ferritic stainless steel
GHG	Greenhouse gases
IC	Interconnect
IPCC	International Panel on Climate Change
MCO	$Mn_{1.5}Co_{1.5}O_4$
OCV	Open circuit voltage
R1000	Reduced samples
R1000 Reox900	Reduced and re-oxidized samples
SEM	Scanning electron microscopy
SMR	Steam methane reforming
SDR	Steam dry reforming
SOC	Solid oxide cell
SOEC	Solid oxide electrolyzer cell
SOFC	Solid oxide fuel cell
TEM	Transmission electron microscopy
TPB	Triple phase boundary
WGS	Water gas shift
XRD	X-ray diffraction
YSZ	Yttria stabilized zirconia

List of Figures

1	Present day warming (2018) [47]	1
2	Energy production by source (2018) [47]	2
3	Annual time series on weekly average that illustrate the seasonal relationship of electricity demand and solar generation for Europe (normalized values) [55]	2
4	Energy efficiencies and hydrogen selling prices of different production technologies [57]	4
5	General layout of a Power-to-X plant with inflows of water (H_2O), electricity and carbon dioxide (CO_2), and outflows of PtX product, by-product oxygen (O_2) and side products [58]	5
6	SOC layout and reactions [62]	6
7	Typical Polarization V-I Curve of SOFC [68]	7
8	Schematic combined gas turbine power plant with SOFC [70]	8
9	Comparison of typical electrolyzer polarization curve ranges [63]	9
10	Artificially colored SEM micrograph of cross-section of a DTU-manufactured anode supported SOC of 350 μm [64]	10
11	Thesis overview	14
12	Linear dependence of the BCY10 film thickness in 1 min as a function of the EPD voltage (30–60 V) [10]	16
13	Relationship between deposit thickness and time of deposition for ZnO coatings on copper electrode at different applied potential [11]	17
14	SEM backscatter electron images of $MnCo_{1.7}F_{0.3}O_4$ coated Crofer 22 APU after sintering heat treatments [16]	18
15	Ellingham Diagram for metal oxides [25]	19
16	Oxide scale formation phases, adapted from [22]	20
17	Chromium evaporation curves for different steels in air + 3% H_2O at 850°C [30]	21
18	Electrical resistances overview of a coated steel core [72]	22
19	Illustrations of the four-point set-up for ASR measurement [24]	23
20	wt.% CROFER 22 APU [44]	24
21	Physical properties of CROFER 22 APU [44]	24
22	Co-deposition mechanism illustration	25
23	Preliminary samples overview	26
24	5Fe5CuMCO R1000 Reox900 sample	27
25	Number and type of samples according to different heat treatments	27
26	EPD layout	28
27	Uniaxial press for the production of pellets	29
28	Dilatometric measurements	31
29	Coefficients of thermal expansion calculated for all compositions in different temperature ranges	31
30	Mean trends of dilatometric measurements, errorbars refer to standard deviation	32
31	CTEs comparison in the range 150 - 900 °C	33
32	CTEs variation in function of temperature	34
33	Comparison of XRD patterns after reduction	35
34	Comparison of XRD patterns after complete sintering process	35
35	Cross section SEM images and EDS of reduced samples: a) 10Fe10CuMCO b) 5Fe5CuMCO c) 10Fe5CuMCO d) 5Fe10CuMCO	37
36	Top view SEM images of reduced samples	38
37	Top view SEM image of a 5Fe10CuMCO R1000 coating	38
38	Cross section SEM images and EDS of as-sintered samples: a) 10Fe10CuMCO b) 5Fe5CuMCO c) 10Fe5CuMCO d) 5Fe10CuMCO	40

39	Top view SEM images of as-sintered samples	41
40	Top view SEM image of a 5Fe10CuMCO R1000 Reox900 coating	41
41	TEM images of as-sintered 10Fe10CuMCO coating on Crofer 22 APU: overview of the FIB lamella (a), CROFER 22 APU and coating interface (b), outer part of the coating (c), EDS elemental analysis of coating/Crofer 22 APU interface (d)	42
42	Mean mass gain of coated samples with error bars related to the standard deviations	43
43	Parabolic rate plot with regression lines	44
44	Overall mass gain after 1000 h, parabolic oxidation rate and oxide scale thickness . .	45
45	ASR over temperature (200 - 700 °C) of as-sintered samples	46
46	ASR measurements at operating temperature (750°C) of as-sintered samples	47
47	Natural logarithm of ASR/T plotted over the inverse of T with trend lines (600-750 °C) of as-sintered samples	47
48	ASR (Pt contacts) over the inverse of T (200-700 °C) of 1000 h samples	48
49	ASR measurements at operating temperature (750°C) of 1000 h samples	48
50	Natural logarithm of ASR/T plotted over the inverse of T with trend lines (600-750 °C) of 1000 h samples	49
51	Activation energy overview	49
52	Comparison of XRD patterns of 1000 h aged coatings	50
53	Top-view SEM images and EDS of 10Fe10CuMCO aged coating	51
54	Top-view SEM images and EDS of 5Fe5CuMCO aged coating	51
55	Top-view SEM images and EDS of 10Fe5CuMCO aged coating	52
56	Top-view SEM images and EDS of 5Fe10CuMCO aged coating	52

1 Introduction

In the last few years, record temperatures and extreme weather events are have been registered all over the world [46]. International Panel on Climate Change (IPCC) reports that human activities have caused approximately $1\text{ }^{\circ}\text{C}$ of global warming and temperatures are still increasing at a rate of $0.2\text{ }^{\circ}\text{C}$ per decade [47]. These changes result in severe alterations to human and natural systems, mainly affecting vulnerable populations and generating instability, such as migration and poverty [47]. The actual warming relative to the pre-industrial level is presented in Fig. 1.

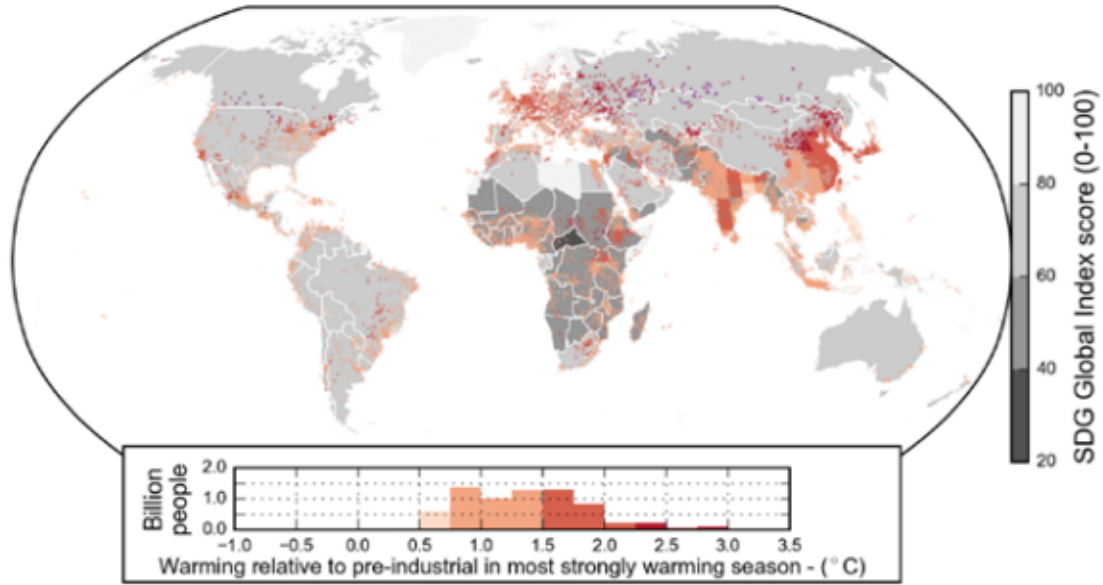


Figure 1: Present day warming (2018) [47]

The emission of greenhouse gases (GHGs) is a key driver of global warming, in particular carbon dioxide has the largest contribution. CO₂ concentration in atmosphere is continuously increasing from pre-industrial period. In 2019 it has reached the level of 409.8 ppm, the highest value in the past 800,000 years, at least [50].

Most of GHG emissions are caused by fossil fuels combustion for energy production; moreover, advancements in economy and technologies are drastically increasing the energy requirements, especially in emergent countries.

However, the general awareness of the climate change problem and the fossil fuels shortage are increasing the interest in environmental protection and energy saving. Some strategies to reduce the dependence on fossil resources are found to be either the reduction of the energy demand or the increase of energy production efficiency and a wider use of renewable energy sources (RES) [52].

Fig. 2 shows a clear overview of the global energy scenario of 2019. In electricity production low-carbon sources (nuclear and renewable energy) amount is about 1/3 of the total, while the remaining is produced with use of fossil fuels (oil, coal and gas). Taking into account the heat production and the transportation sector, fossil fuels are even more relevant.

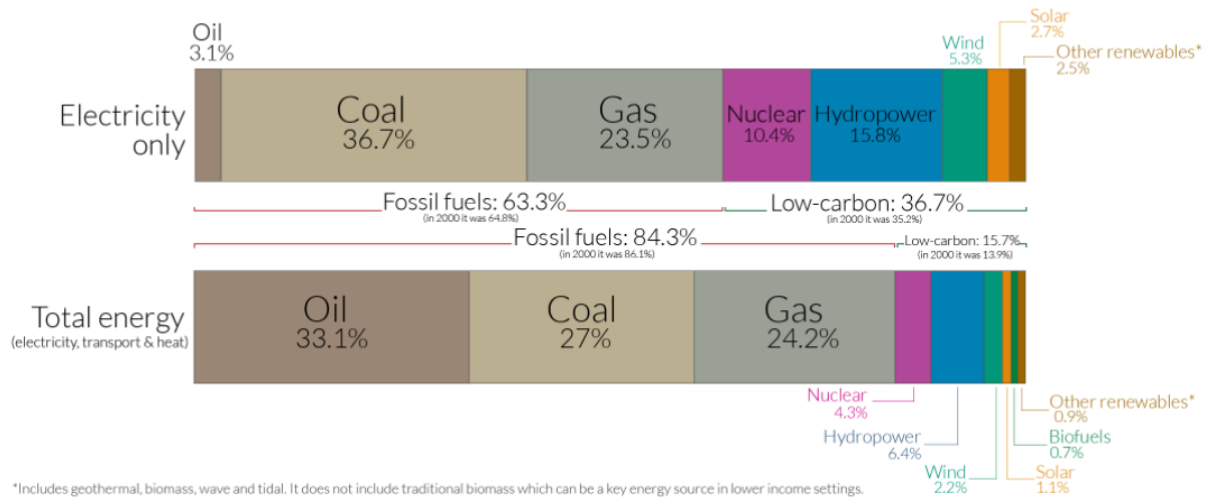


Figure 2: Energy production by source (2018) [47]

According to the European Green Deal, one of the main goals of European Union is to be climate neutral in 2050 [54]; this goal can be fulfilled by progressively reducing the greenhouse gases emissions until reaching 0.

From this point of view, the low GHGs emissions and the renewable nature of the energy sources make renewable energy technologies very promising.

However, one of the issues undermining a widespread development of renewable energy technologies is the lower economical competitiveness than traditional power plants due to intermittency of energy production and the relatively high maintenance cost [52].

To deal with the discontinuity of production and the energy demand, advancement in energy storage technology is necessary on different scales, from seasonal to hourly [55]. An example of correlation between solar energy production and demand during the year is presented in Fig. 3.

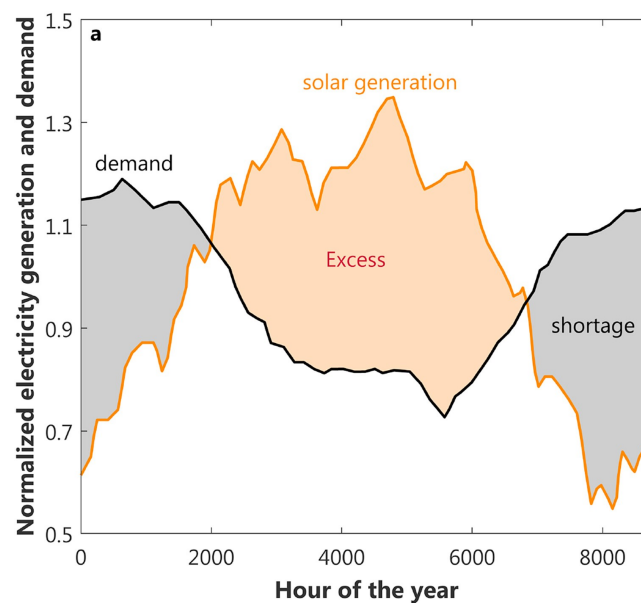


Figure 3: Annual time series on weekly average that illustrate the seasonal relationship of electricity demand and solar generation for Europe (normalized values) [55]

When in excess, renewable energy can be stored if capacity is available; when in deficit, reserve capacity has to be activated as alternative to the grid support from traditional power plants.

In a daily perspective, closed batteries may be enough, but other technologies must be investigated for a long-term storage.

In this context, hydrogen technologies are some of the most promising solutions.

The Green Deal has presented “A Hydrogen Strategy for a climate neutral Europe” [56], in which EU highlights the importance of hydrogen technologies in order to reduce the carbon emissions and reach the climate neutrality. According to their programs, from 2030 onwards renewable hydrogen will be deployed at a large scale, thus hydrogen technologies will be strongly promoted and developed.

Storage is only one of the possible applications: indeed, hydrogen is recognized for its potential to revolutionize the energy value chain from generation and distribution to final application. On industrial scale, hydrogen can be produced from fossil fuels and biomass via steam methane reforming (SMR), partial oxidation (oil), gasification (coal), from water via electrolysis.

In particular, the interest is focused on the so called “green hydrogen”, obtained from the conversion of renewable energy. Green hydrogen can be produced through the decomposition of water using various processes, including electrolysis, photo-electrolysis and thermochemical cycles [57].

However, nowadays the large majority of the hydrogen produced worldwide for different markets (i.e. petrol chemical, food, chemical) derives from reaction of methane of fossil origin through processes such as steam methane reforming (SMR) with efficiencies that can reach 80%.

The production of hydrogen from solid and liquid fuels is even possible and consists in the gasification of the fuel and in the enrichment in H_2 , but this process is more capital-intensive and less efficient than SMR [57]. A comparison of some production technologies in energy efficiency and selling price is contained in Fig. 4.

Actually, SMR is the most economically convenient technology, followed by coal gasification. In the actual transition, the production from fossil fuels is important because of its affordability, but the carbon emissions will limit the use of methane and coal in future.

Production Technology	Energy Efficiency (%)	Hydrogen Selling Price (\$/kg)
Steam methane reforming (SMR)	83	0.75
Partial oxidation of methane	70–80	0.98
Autothermal reforming	71–74	1.93
Coal gasification	63	0.92
Direct biomass gasification	40–50	1.21–2.42
Electrolysis (Nuclear Fission Powered)	45–55	1.95
Photocatalytic water splitting	10–14	4.98

Figure 4: Energy efficiencies and hydrogen selling prices of different production technologies [57]

Once produced, hydrogen can be stored or converted in a specific product for different applications. This is the power-to-X (PtX) concept. A simple scheme of a PtX plant is presented in Fig. 5.

Due to the very low density (0.08409 kg/Nm^3) at ambient conditions, hydrogen needs very large storage. The best known option are salt caverns. Excess hydrogen can be fed into the natural gas grid, but the maximum fraction of H_2 allowed is actually restricted to the range 5-10 vol.%. Indeed a higher amount requires adaptations of turbines, compressors, pipelines and other components [58].

Hydrogen can be utilized to produce other storable energy carriers such as methane, liquid fuels, methanol and other chemicals, whose transport and storage is cheaper and easier compared to both hydrogen and electricity [58].

This is possible with the integration of CO_2 from carbon capture and sequestration (CCS). This technology includes CO_2 separation, its transportation and the final sequestration. The most common separation processes are the post-combustion, the pre-combustion and the oxy-fuel combustion carbon capture [59].

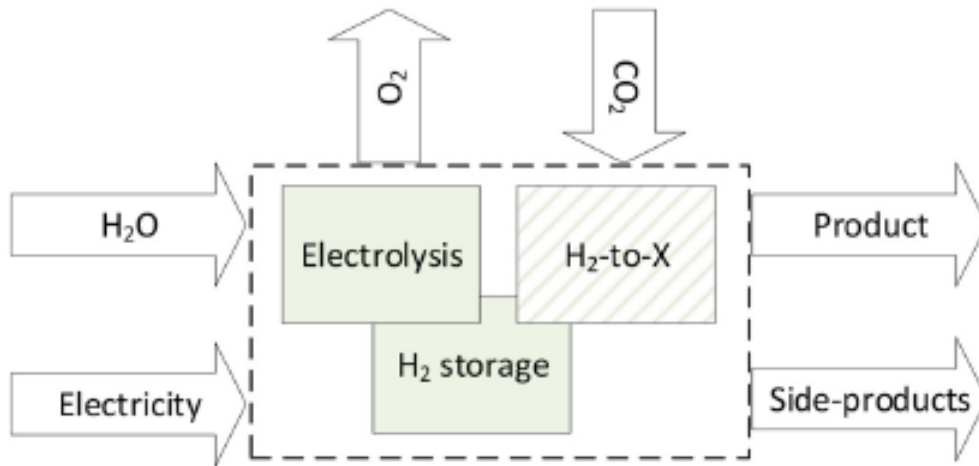


Figure 5: General layout of a Power-to-X plant with inflows of water (H_2O), electricity and carbon dioxide (CO_2), and outflows of PtX product, by-product oxygen (O_2) and side products [58]

Although the first studies on fuel cells were carried out since the nineteenth century, the first applications were seen in 1960 by NASA in the Gemini and Apollo space programs. Nowadays, they reached a commercialization phase spreading in many sectors, from transportation with portable fuel cells to power production with stationary fuel cells [60]. Today, there are many types of fuel cells in the market, commonly categorized by the electrolyte material. The most considered are the Direct Methanol Fuel Cell (DMFC), the Alkaline Fuel Cell (AFC), the Proton Exchange Membrane Fuel Cell (PEMFC), the Phosphoric Acid Fuel Cell (PAFC), the Molten Salts Fuel Cell (MSFC) and the Solid Oxide Fuel Cells (SOFC).

Among them, PEMFC and SOFC are the most promising devices.

PEMFC are very interesting for transport applications due to their high power density, low weight, low operating temperature, fast start-up and high efficiency. However, only pure hydrogen can be used in these devices due to the Pt catalyst contained in the electrodes.

Both the Proton Exchange Membrane Cell (PEMC) and the Solid Oxide Cell (SOC) can be used in reverse operation, as electrolyzers, without modifying the components and the layout of the cell, giving the possibility to produce electric energy from a fuel or the contrary according to the needs.

1.1 Solid Oxide Cells

Solid oxide cells (SOCs) devices are of great interest for efficient and clean power generation and for highly efficient conversion of electricity to hydrogen, fuels and chemicals using high temperature electrolysis.

SOCs are high temperature cells, with operating temperature between 650 °C and 850 °C. They are characterized by very high efficiency, fuel flexibility and slow startup and load following. Thus, their best application is stationary.

A SOC may be operated either as a solid oxide electrolyzer cell (SOEC) or a solid oxide fuel cell (SOFC) [61][62].

A schematic of the two options is presented in Fig. 6.

A SOC is composed by three main components: the fuel electrode, the electrolyte and the oxygen electrode. In order to reach the required voltage and power, many cells are electrically connected through an interconnect (IC) in a stack.

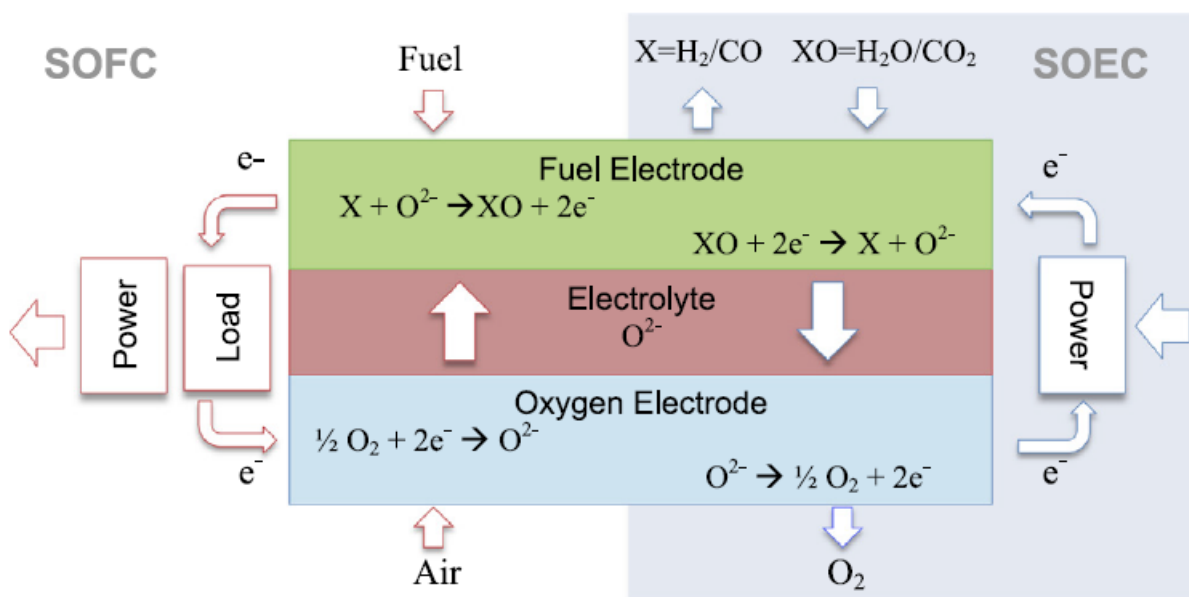
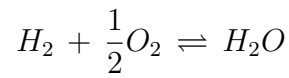


Figure 6: SOC layout and reactions [62]

SOFC

In SOFC mode the cell produces electricity and heat by the combination of air with a fuel such as H_2 , natural gas, syngas and hydrocarbons [62].

In the hydrogen case, the overall reaction is:



The output voltage is given by:

$$V_{fc} = E - V_{act} - V_{con} - V_{ohmic}$$

where E is the Nernst voltage [V], V_{act} is the activation loss, V_{con} is the concentration loss and V_{ohmic} is the ohmic loss.

The Nernst voltage is the open circuit voltage when the current is zero, the activation loss is caused by the activation energy necessary to perform the reaction, the concentration loss occur due to mass transfer resistance of reactants and products and ohmic loss is caused by resistance to the flow of ions and electrons in the SOC [69]. Fig. 7 shows the polarization curves and the effect of the losses.

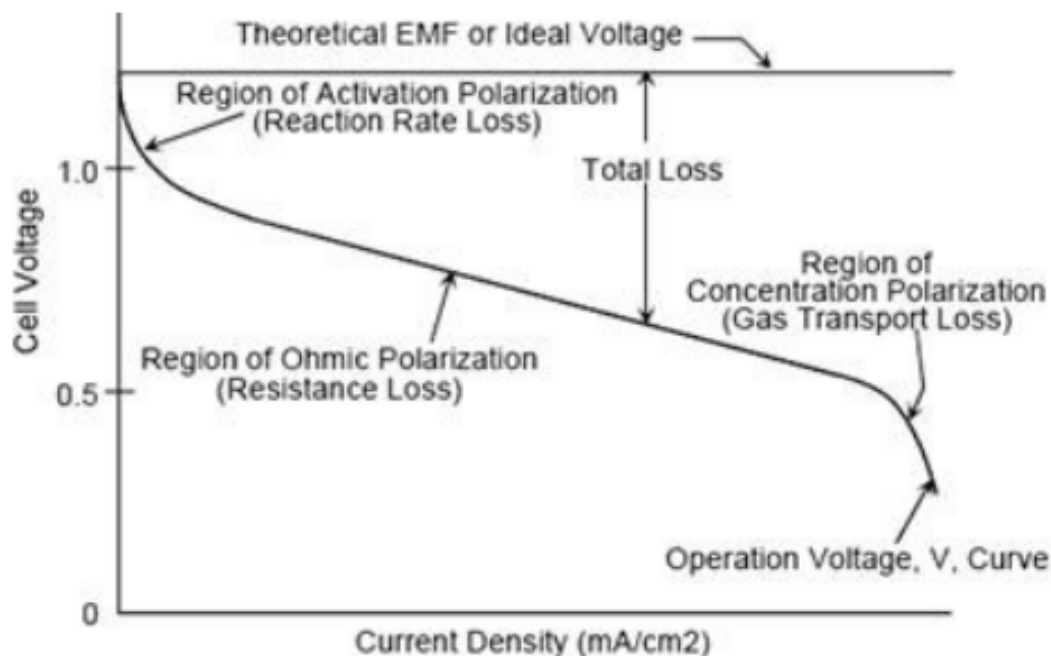


Figure 7: Typical Polarization V-I Curve of SOFC [68]

Due to high temperature and materials properties, the SOFC losses are considerably reduced compared to other fuel cells, PEMFC included. The result is a very high efficiency, beyond 60%.

The fuel flexibility is an interesting feature of SOFCs. Although H_2 shows the best performances from the electro-chemical point of view, CH_4 is better from a balance of plant (BOP, considering auxiliary components) point of view.

When CH_4 is used as fuel, 4 reactions occur:

- Electro-oxidation of the methane: $CH_4 + 4O_2 \rightarrow 2H_2O + CO_2 + 8e^-$
- Steam methane reforming (SMR): $CH_4 + CO_2 \rightarrow 3H_2 + CO$
- Dry methane reforming (DMR): $CH_4 + CO_2 \rightarrow 2H_2 + 2CO$
- Water gas shift (WGS): $CO + H_2O \rightarrow H_2 + CO$

Once the first reaction occurs, H_2O and CO_2 start to be produced. The contemporary presence of CH_4 , H_2O and CO_2 in operational conditions result in the occurrence of SMR and DMR.

As CO is produced, it starts reacting with H_2O in the WGS reaction.

Since SMR is endothermic, the occurrence of such a reaction acts like a thermal sink. Generally, the excess heat produced by the SOFC is removed with an excess of air ($\lambda_{air}=4-6$) driven by a blower. Thus, SMR can give a contribution to reduce the auxiliaries load and save energy.

The drawback of using carbonaceous fuel is the degradation by carbon deposition, that occurs by methane cracking and Bodouard reaction. As a consequence, solid carbon deposits all over the anode surface causing the pore blocking and possible ruptures in the electrolyte.

The best way to solve this issue is to add H_2O together with the fuel by recirculation from the fuel electrode; this cause the occurrence of SMR and avoid the carbon deposition.

There are many applications of SOFCs in the power production.

Besides the stand-alone production, it can be used for industrial CHP systems with the aim of producing both electrical and thermal energy. An after-burner is foreseen to recover the remaining chemical energy in the SOFC exhaust.

Another application is hybridization with a gas turbine (GT). In this case the SOFC substitutes the conventional burner. A scheme of a layout is shown in Fig. 8, in this case the SOFC is connected to the gas cycle by a heat exchanger [73].

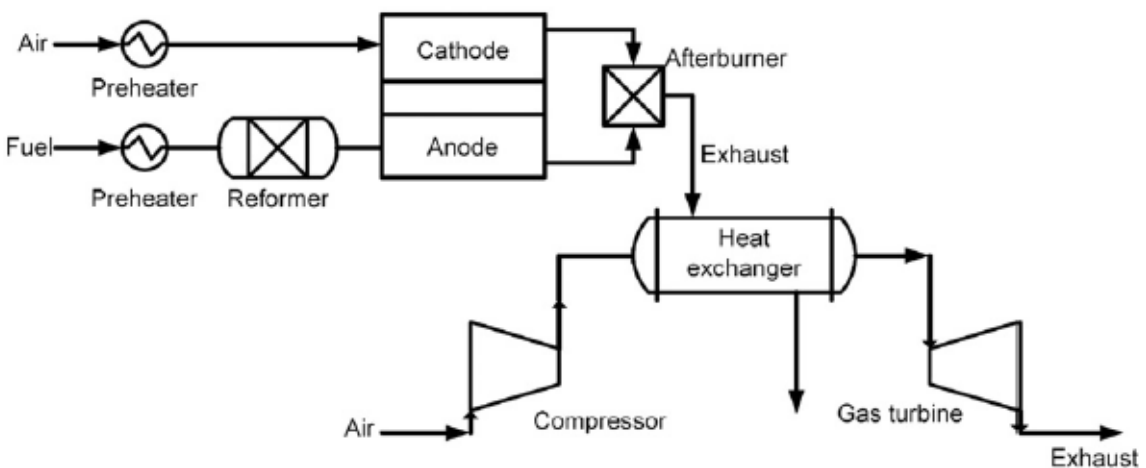


Figure 8: Schematic combined gas turbine power plant with SOFC [70]

SOEC

In SOEC mode, the cell produces chemicals by electrolysis of H_2O and/or CO_2 . If both H_2O and CO_2 take part to the electrolysis, then it is called co-electrolysis.

Due to the high operating temperature, efficiency of SOECs is higher compared to both proton exchange membrane and alkaline electrolyzers. Fig. 9 shows the behavior of the polarization curves for the three options. The open circuit voltage (OCV) is lower in the SOEC case due to the effect of high temperatures, furthermore the ohmic and activation losses are reduced. For a given current of operation, a SOEC requires a lower voltage.

In co-electrolysis, a SOEC is able to produce a mixture of H_2 and CO , called syngas, which is the starting point for the production of chemicals, such as synthetic methane by methanation:

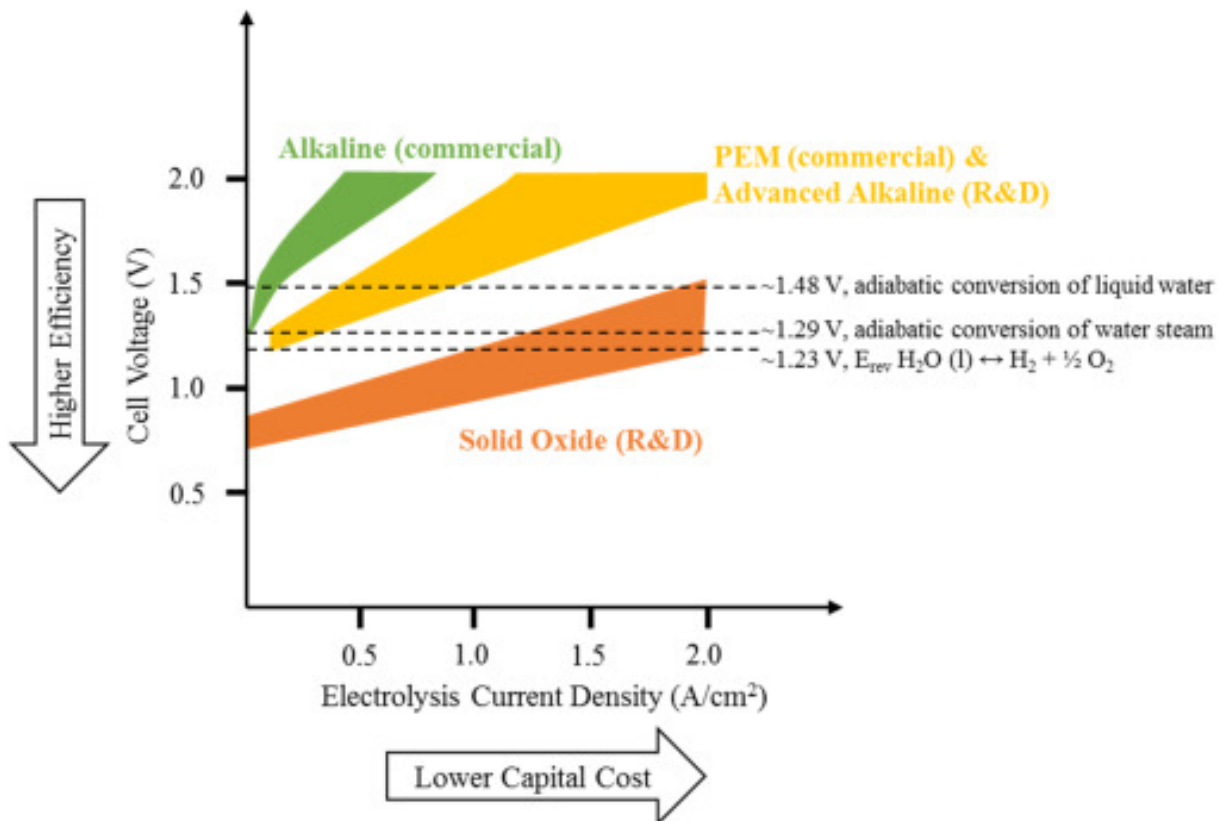
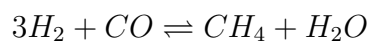
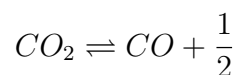
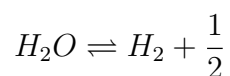
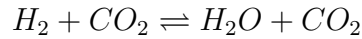


Figure 9: Comparison of typical electrolyzer polarization curve ranges [63]

The overall reversible reactions of co-electrolysis are shown below:



In the co-electrolysis case, H_2 reacts with CO_2 to produce CO via reverse water gas shift :



Ideally, a SOEC can work at efficiency of 100% if it works in thermoneutrality voltage. With respect to the heat demand, the thermoneutral voltage, is the voltage at which neither heating nor cooling takes place.

Usually, the operating point is often above the thermoneutrality in order to produce some extra heat to compensate the heat losses and feed the auxiliaries [71].

The following sub-sections are focused on the materials used for the components of the SOC. An example is shown in Fig. 10.

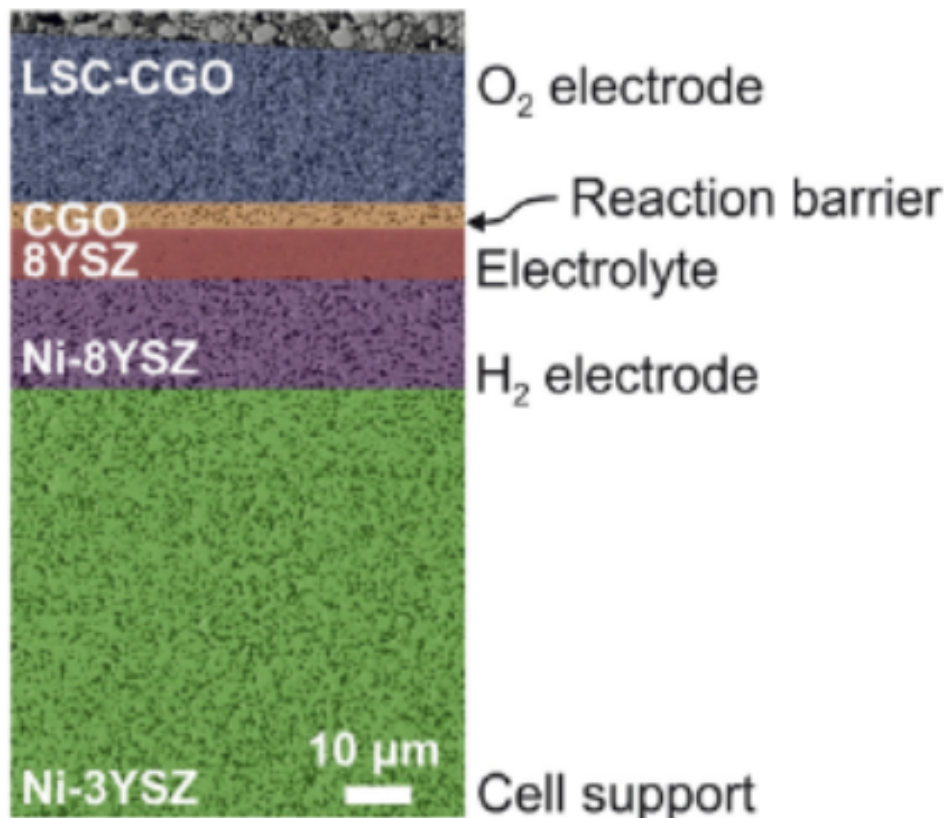


Figure 10: Artificially colored SEM micrograph of cross-section of a DTU-manufactured anode supported SOC of $350 \mu m$ [64]

There are three options to provide mechanical support to the SOC:

- anode-supported cell
- electrolyte-supported cell
- cathode-supported cell

Anode-supported cell is the best solution because offers high triple phase boundary (TPB: the interface among fuel, ions and electrons, where the reaction occur) and involves thin layer of electrolyte which means low ohmic drop.

1.1.1 Electrolyte

The electrolyte must have high ionic conductivity, sufficiently low electric conductivity; it must be fully dense and stable in both reducing and oxidizing environments [64]. Its performances are mainly influenced by the operating temperature, the thickness and the material's choice.

The most common SOC electrolyte is yttria-stabilized zirconia, that consists of $(Y_2O_3)_{0.08}(ZrO_2)_{0.92}$ called 8YSZ. Zirconia presents stable cubic fluorite or tetragonal structure [64].

This material has optimal properties at high temperature, it is quite cheap and available, stable and non-toxic; however it shows performance limitations at intermediate temperatures in ionic conductivity, since it is a thermally activated process [62]. That means that they have to be operated at higher temperatures (750 - 900 °C) to achieve a good performance.

Indeed, YSZ is not fully phase stable at temperatures below 800 °C, because tetragonal zirconia with lower yttria content tends to precipitate at the grain boundaries. Tetragonal zirconia has a considerably lower conductivity than cubic zirconia [64]. Many other solutions were studied, such as other Zirconia-based, $LaGaO_3$ -based, ceria-based and proton conduction electrolytes. The best ionic conductivity for intermediate temperature applications was found to be scandia-stabilized zirconia. This electrolyte shows two main drawbacks: it presents a degradation of ionic conductivity over time at high temperature due to the formation of a Sc scale and it is quite expensive [62].

1.1.2 Fuel electrode

The fuel electrode must be both an electrical and ionic conductor. Moreover, it must be highly porous in order to allow the diffusion of the fuel and have an high catalytic activity. Furthermore, thermos-physical and thermomechanical properties must be compatible with those of the electrolyte.

The most used solution material is the Ni-YSZ cermet, a composite of a metallic nickel and a ceramic yttria stabilized zirconia. The metal provides the necessary electric conductivity while the ceramic the ionic conductivity.

The cermet is obtained by sintering NiO-YSZ with high densification and by reducing the NiO to Ni in order to reach the required porosity (22%). In this way the longest possible TPB is obtained [64].

Ni-YSZ suffers of degradation mainly due to adsorbed impurities, such as the presence of Zr-oxide that reduce the TPB and poison the electrode. This degradation effect is higher in SOEC than in SOFC mode. Other drawbacks are carbon deposition and sulfur poisoning [62].

In order to completely solve these issues many other studies are being carried out. Recent promising electrodes are 10 mol.% Gd-doped Ceria (CGO10) and the perovskite structured strontium iron molybdenum oxide (SFM), but more long-term studies are necessary to determine their validity [64].

1.1.3 Oxygen electrode

As seen for the fuel electrode, the oxygen electrode must be characterized by high electronic conductivity, high electric conductivity, high porosity and high catalytic activity [64].

The most widespread material was $\text{La}_{1-x}\text{Sr}_x\text{MnO}_{3-\delta}$ (LSM) thanks to its high electric conductivity and the compatible thermomechanical properties with YSZ [64].

The main degradation phenomena of oxygen electrode are the electrode delamination at the interface with the electrolyte due to high oxygen partial pressure in the electrolyte and poisoning by chromium, strontium and silica [62].

Research is focusing on other types of perovskites such as $(\text{La}_{0.6}\text{Sr}_{0.4})_{0.98}\text{CoO}_3$ (LSC) and $(\text{La}_{0.6}\text{Sr}_{0.4})_{0.98}\text{CoO}_3$ (LSCF). Due to the reactions that occur at the interface of LSC and YSZ electrolyte, a barrier layer of $\text{Ce}_{0.9}\text{Gd}_{0.1}\text{O}_{1.95}$ (CGO) is commonly placed between them [64].

Despite the high performances registered by LSC, this material is categorized as carcinogenic due to the Co contained. For this reason, new solutions without Co will be investigated [64].

1.1.4 Interconnect

The IC has two main functions: to establish an electrical connection between the fuel electrode and the oxygen electrode of two different cells and to separate the reducing and oxidizing atmospheres.

The main requirements of an interconnect are listed in [66] and include:

- excellent electrical conductivity with area specific resistance below $0,1 \text{ ohm cm}^2$ [67];
- adequate stability in dimension, chemistry and microstructure at operating temperatures;
- low permeability to fuels and oxygen;
- compatible coefficient of thermal expansion;
- chemical compatibility to avoid reactions between the IC and the electrodes;
- high thermal conductivity;
- excellent oxidation resistance;
- low cost fabrication;
- high temperature strength and creep resistance.

Traditionally, ceramics such as LaCrO_3 were widely used as interconnects in SOCs due to the strong chemical stability and the high electric conductivity at temperature near to $1000 \text{ }^\circ\text{C}$. However, their production was expensive since obtaining a dense ceramic is a complex process.

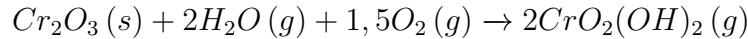
Progresses of the electrolyte materials allowed to reduce the temperature enhancing the efficiency of SOCs, introducing the possibility to use ferritic stainless steels (FSSs) as interconnect. Nowadays, metallic interconnects are preferred because of their excellent electrical conductivity, high strength, simple manufacturability, low cost, and excellent mechanical property in SOC working conditions [65][37].

1.2 Work Overview

1.2.1 The interconnect corrosion problem

Ferritic stainless steels (FSSs) used as interconnects in SOC applications face the issue of fast degradation when subjected to stack operating conditions.

FSSs form a protective Cr_2O_3 scale on the surface, offering a good compromise between electronic conductivity and corrosion protection [17]. However, the oxide scale grows during the SOC stack lifetime causing the loss of electrical conductivity. Moreover, additional degradation is caused by the cathode poisoning. Volatile chromium species can form at the IC surface because water vapor and oxygen react with the chromia scale. According to different studies, the most abundant volatile specie produced is $CrO_2(OH)_2$ [19][20][21]. The reaction that occurs is:



Volatile chromium species can reach the TPB, causing the electrochemical degradation of the electrode [18]. Cr evaporation has a low activation energy and will therefore continue to be a challenge even if the operating temperature of SOFC is further reduced [16].

Specific FSS with high concentration of manganese have been developed to reduce these degradation phenomena. They form an adherent $(Cr, Mn)_3O_4$ spinel top layer above the Cr_2O_3 -layer at about 800 °C that considerably reduces the Cr evaporation [17] [18].

Research is focusing in the development of barrier coatings to further reduce the Cr evaporation and the growth of Cr_2O_3 scale [17]. In particular $Mn_{1.5}Co_{1.5}O_4$ (MCO) spinel is one of the most promising coating materials due to its high electrical conductivity, good CTE match with the stainless steel substrate and an excellent chromium retention capability [12].

The doping of MCO spinels with transition metals (Fe and Cu) has recently previously evaluated as an interesting approach to obtain modification of electric and thermomechanical properties of the manganese cobaltite pure spinels [14][45][43].

1.2.2 Thesis outline

This work focuses on the synthesis and characterization of Fe and Cu doped Mn-Co spinel coatings obtained by electrophoretic co-deposition of $Mn_{1.5}Co_{1.5}O_4$, Fe_2O_3 and CuO .

Electrophoretic deposition (EPD) is used because it has many advantages compared to other methods, such as low costs and short deposition time.

Preliminary samples were produced in different compositions: the Fe and Cu doping level were tuned varying the precursors content in four different EPD suspensions. The morphology and microstructure of the preliminary samples was studied by X-ray diffractometry (XRD) and scanning electron microscopy (SEM) at Politecnico di Torino and by transmission electron microscopy (TEM) at AGH in Krakow, as it will be discussed in the following sections.

Then, optimized coatings were deposited and tested. In particular, the oxidation behavior at 750°C and the area specific resistance (ASR) were analyzed at Gdansk University of Technology for both as-sintered and 1000 h aged samples.

In both cases the substrate was CROFER 22 APU, a ferritic stainless steel developed for SOC interconnects.

Moreover, spinel pellets of the same compositions of the coatings were produced and tested to study the thermomechanical behavior by evaluating of the coefficient of thermal expansion (CTE).

The following scheme [Fig. 11] summarizes the contents of the thesis.

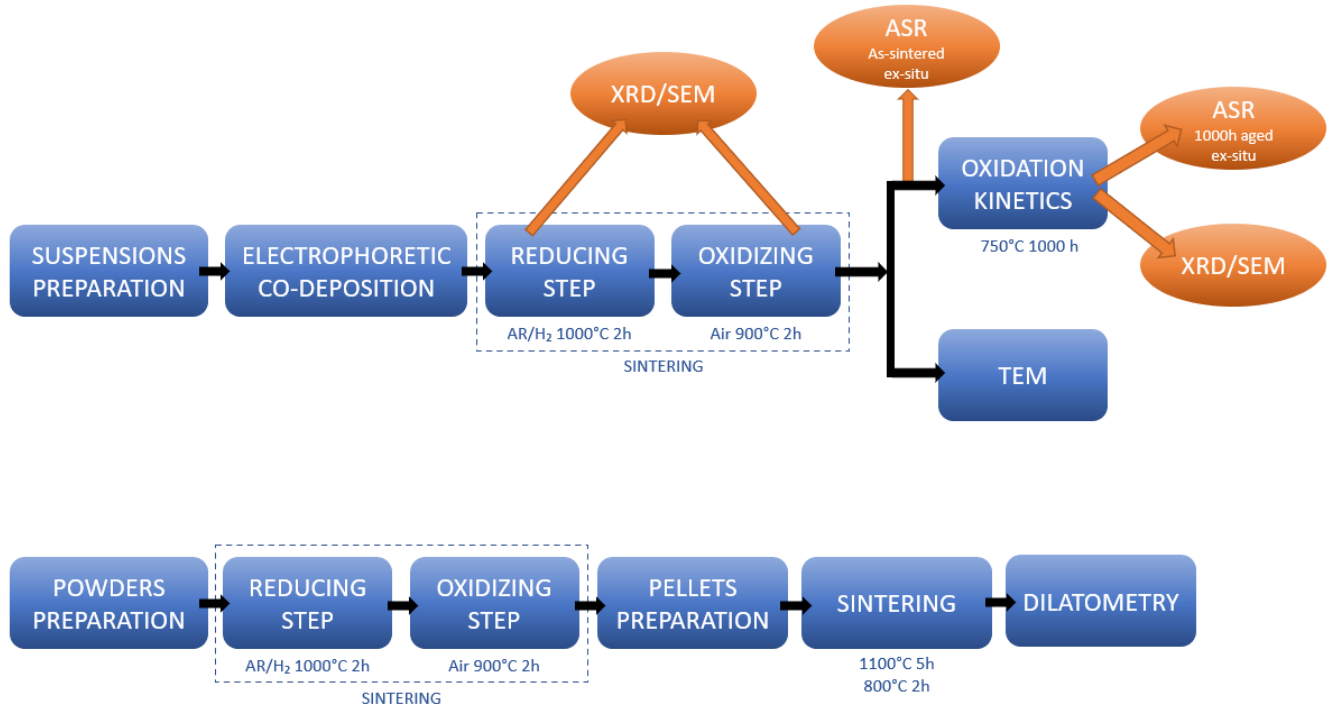


Figure 11: Thesis overview

The following part of Chapter 1 contains considerations about the methods applied for the production and characterization of samples.

Chapter 2 is dedicated to the description of all the experimental procedures carried out during the thesis.

Chapter 3 reports the results obtained from each analysis performed. Thermomechanical properties, microstructure, morphology, oxidation kinetics and electrical performances are discussed and compared.

Conclusions are proposed in Chapter 4, where the most significant results are summarized and future perspectives are pointed out.

1.3 Experimental methods

In this section, the methods of samples production and characterization are discussed relying on literature.

1.3.1 Electrophoretic deposition

Electrophoretic deposition (EPD) is defined as a colloidal process in which charged particles suspended in a liquid medium are deposited on a conductive substrate under the effect of an applied electric field. Advantages of the process are:

- fast deposition;
- apparatus simplicity;
- little restriction of the shape of substrate;
- cost-effectiveness;
- good uniformity.

Thickness and morphology can be controlled adjusting the deposition parameters. [1][2]

The first studies of the correlation between the amount of particles deposited and other deposition parameters were carried out by Hamaker and were summarized in the Hamaker's law [3]:

$$m = C_s E \mu S t$$

where $m(g)$ is the deposit weight, $C_s(g/cm^3)$ is the particle concentration, $E(V/cm)$ is the electric field strength, $\mu(cm^2/sV)$ is the electrophoretic mobility of the particles, $S(cm^2)$ is the deposition area and $t(s)$ is the deposition time.

A similar equation was then introduced by Hirata et al. using Faraday Law [4]:

$$m = 2C_s \epsilon_0 \epsilon_r \xi E t / 3\eta$$

where $C_s(g/cm)$ is the particle concentration, $\epsilon_0(F/m)$ is the permittivity of vacuum, $\epsilon_r(F/m)$ is the relative permittivity of the solvent, $\xi(V)$ is the zeta potential of the particles, $\eta(Pa s)$ is the viscosity of the solvent, $E(V/m)$ is the electric field strength and $t(s)$ is the deposition time.

As it is visible from previous equations, deposited mass depends on several variables that concern both the suspension and the deposition process.

As far as the suspension is concerned, the dispersion of particles into the liquid medium is of fundamental importance. Large particles tend to settle at the bottom of the container, resulting in inhomogeneous deposition. Even if a general rule is not fixed, optimal depositions of a wide variety of ceramic films occur for particles size in the range 1-20 μm . [5][1]

In general, the deposition rate increases with the particles concentration [6]. Particle concentration is directly related to the mass deposited. This aspect is particularly interesting for multi-component EPD because composition of the final film can be controlled. [2]

Surface charge is one of the driving factors of EPD process. It influences the intensity of repulsive forces among particles, thus the suspension stability and particles agglomeration. Indeed, stability is dependent on electrostatic and Van der Waals forces among particles. Surface charge can be increased by adding charging agents such as bases and acids to the suspension[1][2].

Properties of liquid medium determine the success of a good deposition. Dielectric constant must not be too high because the particles mobility is reduced. On the contrary, too low dielectric constant means insufficient dissociative power. According to Powers, the best range is 12-25 [8]. Even the conductivity of the liquid must be in the correct range; it can be increased adding dispersants and raising the temperature [1].

Moving to the deposition parameters, the first key factor is the applied voltage; it influences the driving force applied on suspended particles. At high voltages the driving force grows, as a consequence the deposition rate increases.

However, high voltage leads to a strong production of bubbles due to electrochemical reactions in some cases (e.g. electrolysis of water) and gas development at the electrodes [2]. Moreover, high deposition rate caused by high voltage reduces the film quality and thickness due to turbulence in the suspension. Basu et al. report that the best range for deposition is 25-100 V/cm, while over 100 V/cm worse performances are reached [9].

An example of the influence of voltage on the deposition of BCY10 is shown in Figure 12.

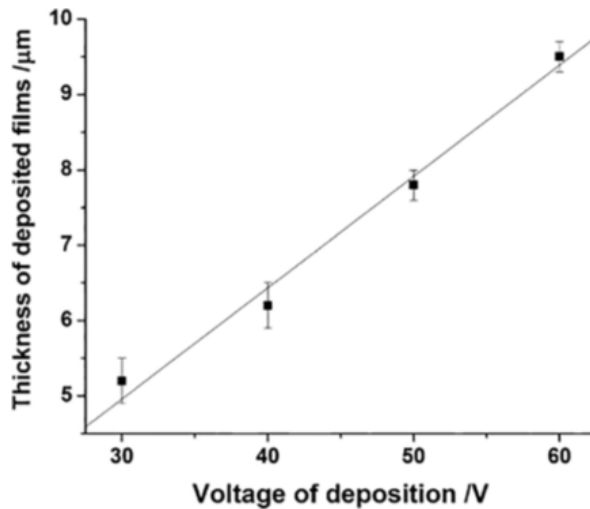


Figure 12: Linear dependence of the BCY10 film thickness in 1 min as a function of the EPD voltage (30–60 V) [10]

The coating thickness is dependent on the deposition time. Basu et al. study shows how the thickness grows increasing the deposition time at fixed applied field until it reaches a plateau [9]. This behavior for ZnO is shown in Figure 13.

Keeping a constant voltage, the electric field decreases with deposition time because of the formation of a more and more thick insulating ceramic layer on the substrate surface. This phenomenon causes the reduction of the deposition rate over time [1].

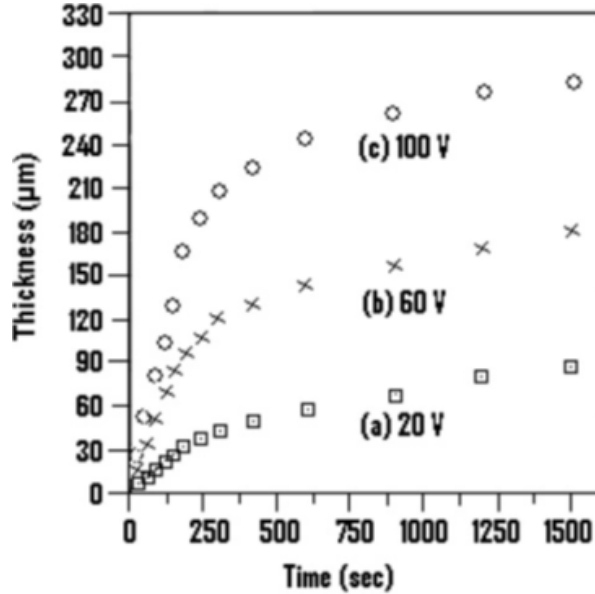


Figure 13: Relationship between deposit thickness and time of deposition for ZnO coatings on copper electrode at different applied potential [11]

EPD is collecting interest in SOC applications. Studies were carried out for the fabrication of electrodes, electrolytes, function layer, barrier layer [7]. The area of application of interest for this work is the deposition of spinel coatings onto metallic interconnects coatings.

The co-deposition of Manganese cobalt oxide (MCO), Fe_2O_3 and CuO was found to be cathodic. As discussed in [12] and [13], both MCO and CuO have positive zeta potential in $EtOH/H_2O$, thus they are attracted by the negative electrode. Instead, E. Zanchi et al. [14] show that Fe_2O_3 in $EtOH/H_2O$ develop a negative surface charge. However, due to differences in size, concentration and charge, Fe_2O_3 associate with MCO particles and the deposition is still cathodic.

This part will be discussed in more details in section 2.1.

1.3.2 Sintering

Sintering is a key process for the production of spinel coatings deposited by electrophoretic method. Heat treatment parameters must be optimized to obtain a dense and homogeneous film.

A first possible way is to perform a single-step sinter. It consists of a heat treatment in air in the range 900 – 1100 °C.

Bobruk et al. [15] shows how single step sinter of MCO at 900 °C and 1000 °C led to a diffuse open porosity and poor densification. On the other hand, coatings reduced at 1100 °C exhibited a good densification, but cracks at the chromia/spinel interface were identified after the re-oxidation step; moreover, the reduction treatment at higher temperature caused the development of a significantly thicker oxide scale.

Due to these issues a two-step sinter is preferred. The first heat treatment is performed in reducing atmosphere, while the second one in air (re-oxidation).

For pure MCO spinel, after the reduction step MnO and metallic Co are obtained. The re-oxidation leads to the formation of a new spinel phase. The densification effect was found to

be caused by the coarsening of metallic Co during the reducing step [15].

E. Zanchi et al. [14] showed how the reduction phase in case of co-deposition of MCO and Fe_2O_3 had led to the decomposition in MnO and metallic Co as seen above and an additional cobalt and iron alloy. The re-oxidation allowed to obtain a Fe-doped MCO spinel.

Fig. 14 shows the differences among the heat treatments in densification and chromia scale development of $MnCo_{1.7}F_{0.3}O_4$. It is clearly visible that the highest coating densification is reached with higher temperature of the reducing step and a subsequent oxidation. However, higher reduction temperatures also brings to the development of a thicker oxide scale.

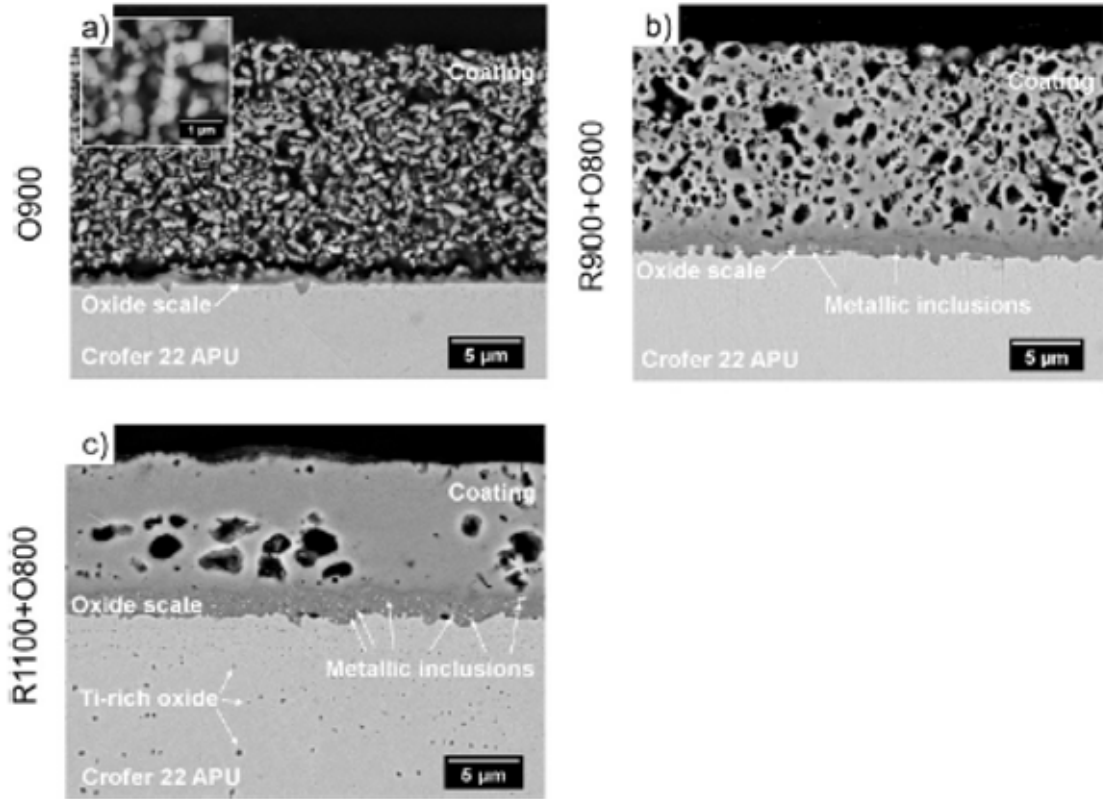


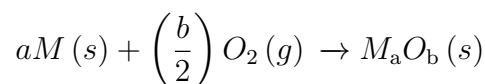
Figure 14: SEM backscatter electron images of $MnCo_{1.7}F_{0.3}O_4$ coated Crofer 22 APU after sintering heat treatments [16]

In [15][14] the best sintering procedure was found to be a reduction treatment in H_2/Ar at 1000 °C for 2 hours and a re-oxidation in air at 900 °C for 2 hours; no cracks and very good density were observed.

1.3.3 Thermogravimetric test

In section 1.2.1 the corrosion problem had been presented. In the following part the oxidation theory from both thermodynamic and kinetics point of view is reported.

When in ambient conditions most metals are thermodynamically unstable and react with gases [22][23]. The general reaction that occurs between a metal (M) and oxygen is:



If the Gibbs energy is less than 0, then the reaction is spontaneous. Gibbs energy is defined as follows:

$$\Delta G = \Delta G^0 + RT \ln \left(\frac{a_{M_a O_b}}{a_M^a + a_{O_2}^{(b/2)}} \right)$$

where ΔG_0 represents the change in free energy when all species are in their standard state, R is the universal gas constant, T is the temperature and a is the activity of each component [24].

The Ellingham-Richardson diagram (Fig. 15) relates the standard Gibbs free energy and the dissociation pressure to temperature. Practically, it allows to verify if there is the possibility of oxidation of a specific metal.

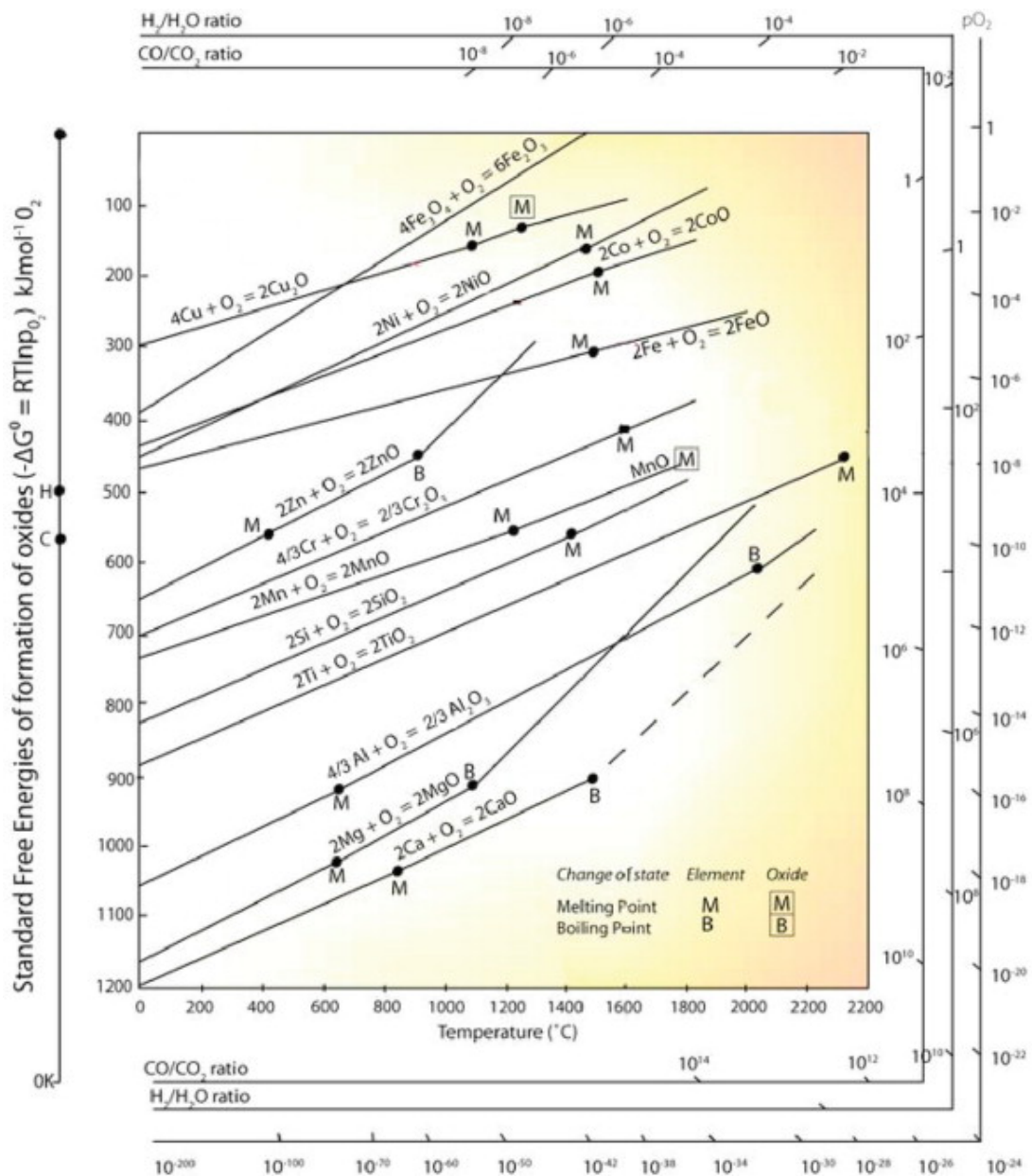


Figure 15: Ellingham Diagram for metal oxides [25]

The example of interest for this work is the oxidation of Cr to Cr_2O_3 . The diagram points out that at $800^\circ C$ and with oxygen partial pressure of about 10^{-20} atm the oxidation occurs.

Kinetics of oxidation is necessary to study the long-term behavior of the interconnects.

Phases of oxidation are shown in Fig. 16, the oxygen adsorption and the oxide nucleation are fast at high temperatures, while the oxide scale growth depends on the densification and protection of the oxide scale itself [24].

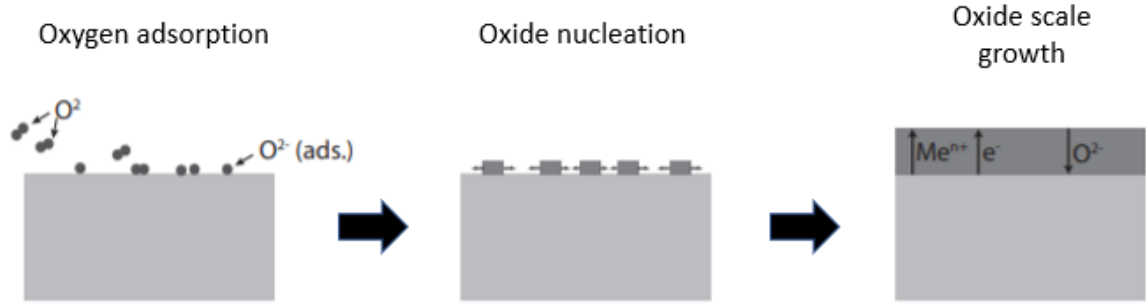


Figure 16: Oxide scale formation phases, adapted from [22]

If the oxide scale is dense and protective, the growth rate will decrease with time due to the increasing length of the diffusion paths. Thus, the resulting oxide scale growth is parabolic [26]. The thickness behavior can be expressed as:

$$\frac{dx}{dt} = k_{p,t} \cdot \frac{1}{x}$$

$$x^2 = 2k'_{p,t} \cdot t + C$$

where $x[cm]$ is the oxide scale thickness, $t[s]$ is the exposure time and $k'_{p,t} [cm^2s^{-1}]$ is the parabolic oxidation rate constant.

In general, the initial stages of oxidation (0-250 h) do not follow a parabolic behavior [22].

In case of porous and non-protective oxide scale the growth follows a linear behavior [24].

$$\frac{dx}{dt} = k_{l,t}$$

$$x = k'_{l,t} \cdot t + C$$

where $k'_{l,t}$ is the linear oxidation rate constant.

One of the practical methods applied in the evaluation of the oxidation process of both bare and coated steel is the measurement of the mass change over time at operating temperature.

Indeed, the mass change can be correlated with the oxygen uptake during oxidation. However, no others phenomena that can change the weight have to occur [26].

The parabolic oxidation rate in terms of mass change can be obtained by the conversion of the one seen in terms of thickness to the following equation:

$$k_{p,m} = \left(\frac{M_{M_aO_b}}{b \cdot M_O \cdot \rho_{M_aO_b}} \right)^2 \cdot k_{p,t}$$

where $M_{M_aO_b}$ is the molar mass of the oxide, M_O is the molar mass of oxygen and $\rho_{M_aO_b}$ is the oxide density [24].

The parabolic and linear kinetics can be expressed as follow:

$$\left(\frac{\Delta m}{A} \right)^2 = 2k_{p,m} \cdot t + C$$

$$\frac{\Delta m}{A} = k'_{p,m} \cdot t + C$$

where $\Delta m[g]$ is the mass gain and $A[cm^2]$ is the surface area.

FSSs suffer of Cr evaporation that induce a loss of weight, this phenomenon can reduce the effectiveness of mass gain measurements.

As seen in section 1.2.1, CROFER 22 APU is a special alloy for SOC applications. Due to its high Mn concentration the Cr evaporation is lower compared to other specific steels for SOC interconnects [30], as presented in Fig. 17.

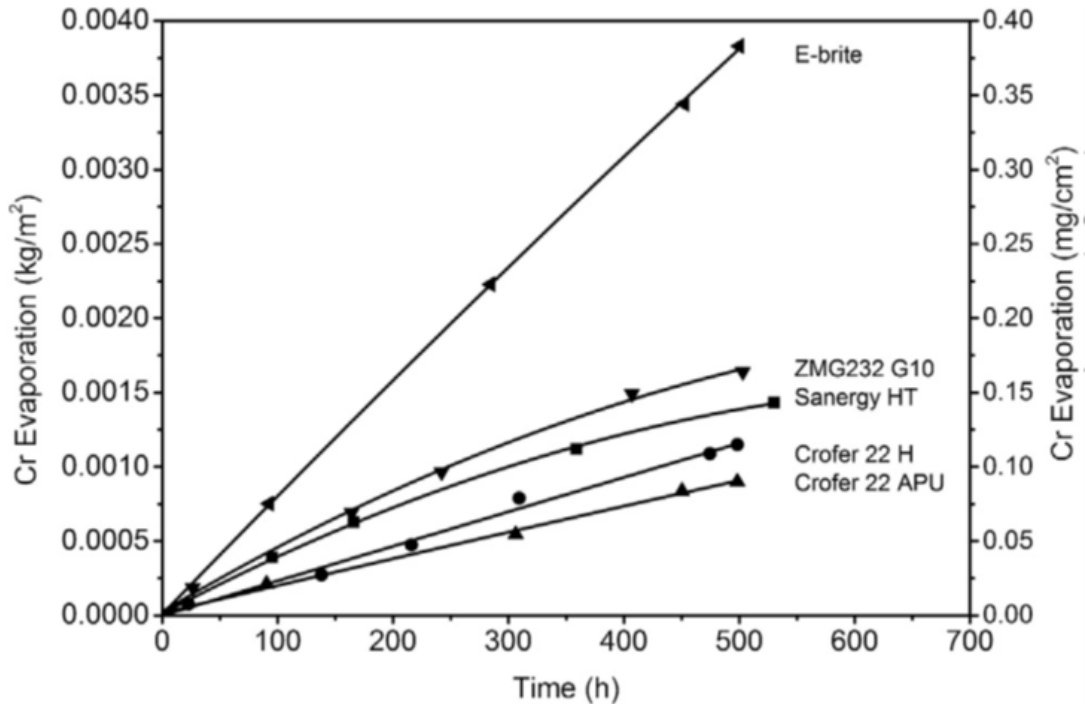


Figure 17: Chromium evaporation curves for different steels in air + 3% H_2O at 850°C [30]

Most of the studies carried out on CROFER 22 APU showed that mass change over time observed a parabolic behavior at high temperatures [27][28][29].

B. Talic et al. [16] showed how the application of MCO coatings considerably reduce both mass gain and Cr evaporation.

1.3.4 ASR test

In a SOC stack, the interconnect provides electrical connection between different cells and to the external circuit. Thus, the electrical conductivity of the interconnect material is important and must be the highest possible.

The growth of the oxide scale leads to a reduction of the interconnect electrical conductivity during its lifetime [31], because the resistance of the oxide scale is considerably higher than the resistance of the steel [24].

The application of coatings is a way to improve the performances of interconnects, even in terms of electrical conductivity [31].

The contribution to total electric resistance are shown in Fig. 18.

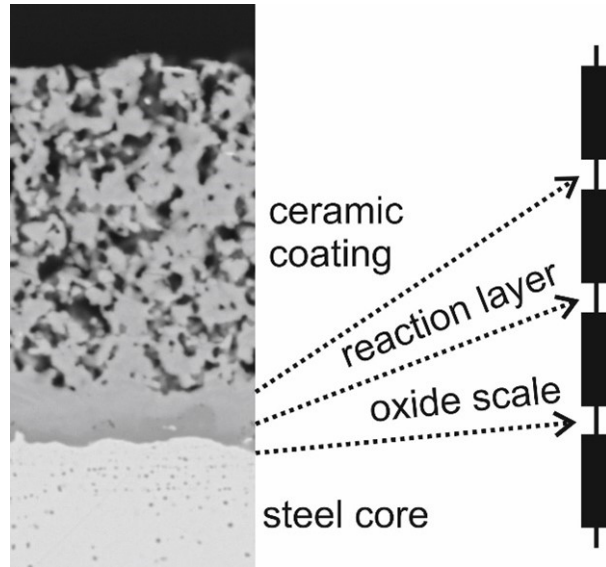


Figure 18: Electrical resistances overview of a coated steel core [72]

Four contributions to total resistance of the interconnects can be identified [72]:

- Resistance of the steel - due to very high electronic conductivity of steel is negligible ($ASR_{CORE} \sim 0$);
- Resistance of the thermally growing oxide scales (Cr_2O_3 , $(Mn, Cr)_3O_4$), with relatively low electronic conductivity (typically considered to be in the range ~ 0.005 - $0.05 S cm^{-1}$) which considerably contribute to the total ASR; thickness of the oxide increases monotonically, so an increase in ASR over time is expected. Neglecting potential composition changes influence on conductivity, ASR will be directly proportional to oxide thickness;
- Resistance of the reaction layer between the coating and the thermally grown oxide – due to diffusion of Cr from chromia into the neighbouring spinel coating, the electrical

conductivity of the formed reaction layer can be decreased in comparison to the pure initial spinel;

- Electrical resistance of the protective (e.g. $MnCo_2O_4$) coatings typically have electrical conductivity values $\gg 10 S cm^{-1}$, with a very small contribution to the resistance.

The most common way to measure the electrical resistance is the Area Specific Resistance.

Due to the great difference in orders of magnitude between the substrate and the scale electrical resistances, in ASR calculation the steel factors can be neglected [32]. The ASR of an oxidized alloy can be expressed as:

$$ASR_{interconnect} = \rho_{chromia} \cdot \tau_{chromia}$$

where $\rho[m\Omega cm]$ is the specific resistivity and $\tau[cm]$ is the thickness.

In case of application of a coating, the expression become:

$$ASR_{interconnect} = \rho_{chromia} \cdot \tau_{chromia} + \rho_{spinel} \cdot \tau_{spinel}$$

Since the specific resistivities and the coating thickness are constant, then ASR can be assumed to be proportional to the oxide scale mass gain [31].

The electrical characterization presents the contacting issue. Different materials are used as contacts and identify different characterization methods.

The first type of materials used for this application are noble metals. Platinum, gold, silver do not influence the oxide scale, thus they are interesting for a more theoretical point of view. Instead, materials that are used as oxygen electrode in SOCs such as LSM or LSC simulate the real behavior of the interconnect in a SOC stack [31][33-41].

ASR is measured by a four-point set-up, as shown in Fig. 19. ASR can be easily calculated using the following expression:

$$ASR = \frac{\Delta V_{interconnect}}{I} \cdot A_{interface}$$

where $\Delta V[V]$ is the voltage drop, $I[A]$ is the applied current and $A[cm^2]$ is the contact area.

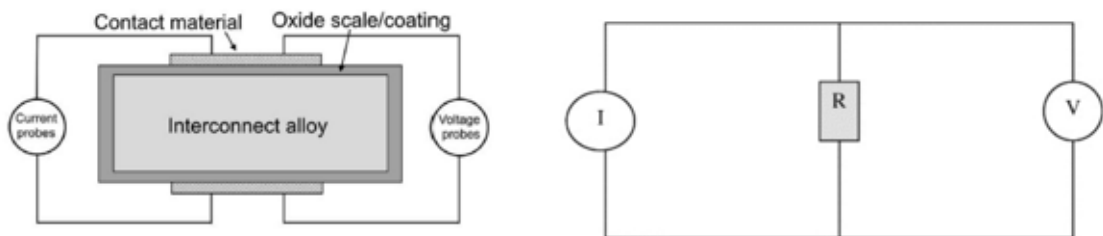


Figure 19: Illustrations of the four-point set-up for ASR measurement [24]

The two possible types of characterization are named in-situ and ex-situ. The in-situ characterization is a continuous ASR evaluation, while ex-situ consists of discontinuous measurements, following regular oxidation scales [31].

2 Experimental

In this section the experimental procedures for coatings synthesis, processing and characterization are detailed.

2.1 Samples preparation

The electrophoretic co-deposition method was used to deposit the protective layer on coupons of CROFER 22 APU (Thyssenkrupp); the steel specifications are listed in Fig.20-21.

	Cr	Fe	C	Mn	Si	Cu	Al	S	P	Ti	La
min.	20.0	bal.		0.30						0.03	0.04
max.	24.0		0.03	0.80	0.50	0.50	0.50	0.020	0.050	0.20	0.20

Figure 20: wt.% CROFER 22 APU [44]

Density	7.7 g/cm ³						0.278 lb/in. ³					
Melting range	1510 °C (Solidus) - 1530 °C (Liquidus)						2750 °F (Solidus) - 2786 °F (Liquidus)					
Temperature (T)	Specific heat		Thermal conductivity		Electrical resistivity (ρ)		Modulus of elasticity		Coefficient of thermal expansion between 20 °C/68°F and T			
	°C	°F	$\frac{J}{kg \cdot K}$	$\frac{Btu}{lb \cdot °F}$	$\frac{W}{m \cdot K}$	$\frac{Btu \cdot in.}{ft^2 \cdot h \cdot °F}$	$\mu\Omega \cdot cm$	$\frac{\Omega \cdot circ \text{ mil}}{ft}$	$\frac{kN}{mm^2}$	10 ³ ksi	$\frac{10^{-6}}{K}$	$\frac{10^{-6}}{°F}$
25	77	470	0.112	26	180	55	330	220	31.9			
200	392	520	0.124	23	160	70	421	210	30.5	10.3	5.7	
400	752	610	0.146	23	160	90	541	195	28.3	10.8	6.0	
500	932							183	26.5	11.2	6.2	
600	1112					105	632			11.4	6.3	
700	1292									11.6	6.4	
800	1472	660	0.158	24	166	115	692			11.9	6.6	
900	1652									12.3	6.8	
1000	1832	650	0.155	27	187	120	722			12.7	7.1	

Figure 21: Physical properties of CROFER 22 APU [44]

First, preliminary samples were produced and the co-deposition was characterized with afterwards analysis. Once best parameters were founded, then optimized coatings were produced and sent to Gdansk University of Technology (PL) for thermogravimetric and area specific resistance tests at 750°C.

The experimental activity demonstrated that the co-deposition of the chosen precursors proceeds in the cathodic direction. In Fig. 22 a co-deposition mechanism is proposed.

MCO and CuO are attracted by the negative electrode, due to their positive surface charge ($Z_{MCO} = +13mV$, $Z_{CuO} = +6mV$ [13]). On the other hand, Fe_2O_3 develops a negative surface charge in $EtOH/H_2O$ ($Z_{Fe_2O_3} = -9.9mV$ [14]). The little size of the particles allows

their aggregation to MCO and CuO , allowing the mutual transportation towards the cathode.

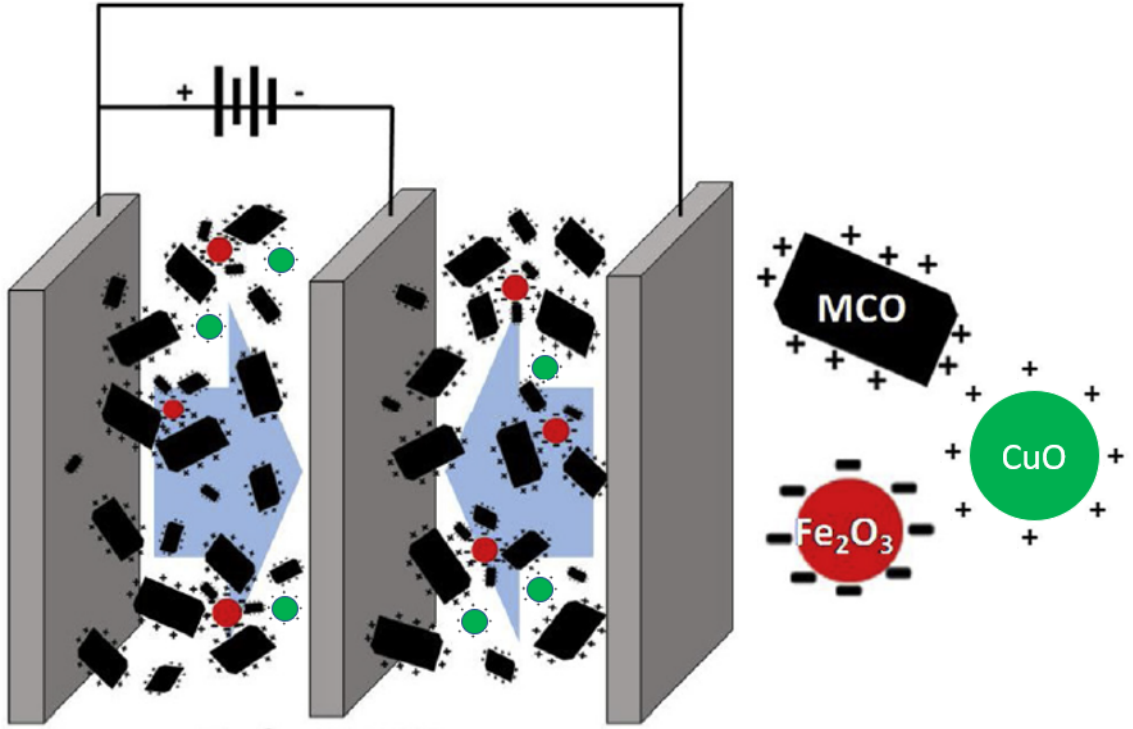


Figure 22: Co-deposition mechanism illustration

2.1.1 Preliminary deposition experiments -EPD parameters and morphological and compositional characterization

Coupons of CROFER 22 APU with dimensions of $1,5 \times 1,5 \text{ cm}^2$ were used as substrates for coating deposition. The coupons were previously washed in ethanol and acetone in the ultrasonic bath in order to remove processing residues.

The first step was the preparation of suspensions composed by 60 vol.% of ethanol and 40 vol.% of double distilled water, mixed in a becker for a total volume of 50 mL. Spinel MCO (ideally at 50% of $Mn_1Co_2O_4$ and 50% of $Mn_2Co_1O_4$ at room temperature), Fe_2O_3 and CuO are added in different compositions for a total amount of powders equal to $37,5 \text{ g/L}$ with the aim of obtaining a large number of sundry samples to test. The g/L value was inspired by other verified experiments of MCO, CuO and Fe deposition [14][12][42][43].

Five different EPD suspensions were obtained varying the percentage in mass of precursors, in this way the Fe and Cu doping level was tuned.

Before starting with the deposition, the suspension was left to stabilize with sonication and stirring for at least 30 min.

When not in use for the deposition, the suspension was kept on the magnetic stirrer to guarantee the suitable homogeneity and avoid sedimentation or aggregation of powders.

Before each deposition, the suspension was further stabilized alternating magnetic stirring

(10s) and sonication (10 s) for three times.

For these preliminary samples the electrophoretic co-deposition was performed with a two-electrode setup. A substrate of CROFER 22 APU of $2 \times 4 \text{ cm}^2$ was used as the anode, while the sample to coat was the cathode.

The distance between the two electrodes was set at 1.5 cm.

A constant voltage of 50 V was applied for thirty seconds to obtain a protective layer of thickness 10-15 μm .

In order to identify short-current events or an ineffective process of deposition, current was registered and the value obtained was about 2-3 mA.

After the deposition, the obtained samples were dried on alumina supports for at least twenty-four hours before thermal treatments.

The summary of the samples obtained, their composition and the labelling is presented in Fig. 23.

Name	Quantity	wt.% Fe_2O_3	wt.% CuO	wt.% MCO	Fe_2O_3 mass [g/L]	CuO mass [g/L]	MCO mass [g/L]
MCO	6	0	0	100	0	0	37.5
10Fe10CuMCO	6	10	10	80	3.75	3.75	30
5Fe5CuMCO	6	5	5	90	1.875	1.875	33.75
10Fe5CuMCO	6	10	5	85	3.75	1.875	31.875
5Fe10CuMCO	6	5	10	85	1.875	3.75	31.875

Figure 23: Preliminary samples overview

After the deposition, thermal treatments had been carried out on the samples to sinter and densify the powders deposited on the metal substrate. The first thermal treatment performed was the reduction in Ar/H_2 (2 vol.%) atmosphere at 1000 °C for 2 hours (10 °C/min). Samples treated in this way are labelled R1000.

The second was the re-oxidation in air at 900 °C for 2 hours (10 °C/min). Complete sintered samples are labelled R1000 Reox900.

Fig. 24 shows one of the as-sintered samples, the resulting coating of the co-deposition and the further sintering was uniform and well adherent to the substrate. Neither cracks, delamination nor visible porosity were detected.

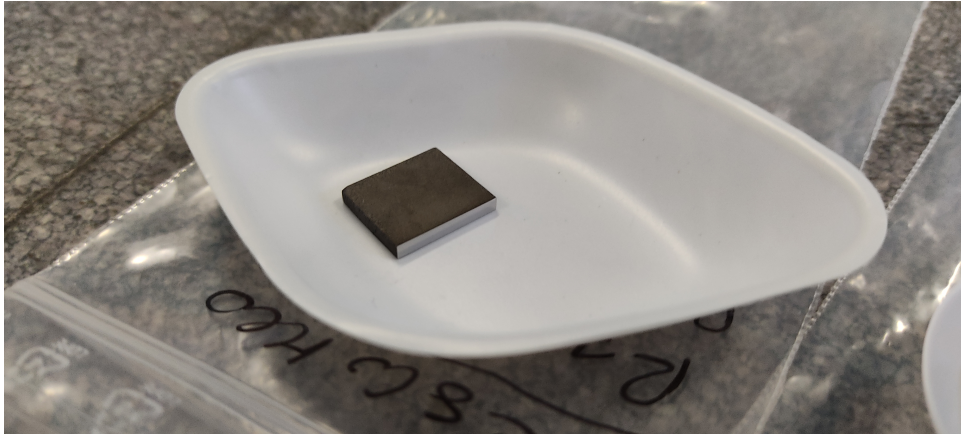


Figure 24: 5Fe5CuMCO R1000 Reox900 sample

A total of 6 samples per composition, according to different heat treatments, were produced in order to carry out microstructure and morphology analysis at each sintering step. A summary of the totality of samples produced is contained in Figure 25.

<i>Name</i>	<i>Total</i>	<i>As-deposited</i>	<i>Reduced</i>	<i>Re-oxidized</i>
MCO	6	2	2	2
10Fe10CuMCO	6	2	2	2
5Fe5CuMCO	6	2	2	2
10Fe5CuMCO	6	2	2	2
5Fe10CuMCO	6	2	2	2

Figure 25: Number and type of samples according to different heat treatments

After the preparation, samples microstructure and morphology was investigated by X-ray diffraction and scanning electron microscopy.

Crystalline phases of coatings had been evaluated by X-Ray diffraction (XRD) with a Bruker D8 instrument with Cu-K radiation.

In order to perform electronic microscopy characterization of cross sections samples were embedded epoxy and then polished with SiC paper.

2.1.2 Optimized deposition experiments

Coupons of CROFER 22 APU (1.5 x1.5 cm) cut from a 0.3 mm thick plate were used as substrates for deposition of optimized coatings. Before the deposition a 3 mm hole was punched near one edge, necessary for the thermogravimetric analysis that was carried out afterwards.

The procedure adopted for the deposition was the same seen for the preliminary samples with slight differences.

The suspension was prepared with a total volume of 100 ml due to the space needed by the electrodes. For this reason, the amounts of powders were doubled compared to the preliminary deposition.

Varying the precursors concentration four different suspensions were obtained: 10Fe10CuMCO, 5Fe5CuMCO, 10Fe5CuMCO and 5Fe10CuMCO; pure MCO spinel was not considered for the

oxidation and electrical characterization because many results have already been obtained in other studies.

In this case the protective layer had to be deposited on both side of the metal coupons, thus the EPD was performed using a three-electrode setup in which the sample to coat was placed between the two positive electrodes (anodes) at 1,5 cm distance from each of them.

Even in this case the deposition was performed in 30 seconds at a voltage of 50 V. The layout is shown in Fig. 26.

All samples were sintered both in reducing and oxidizing atmosphere as seen before, obtaining six samples for each composition for a total of 24.

All coatings were well adherent to the substrate, without any visible defect.

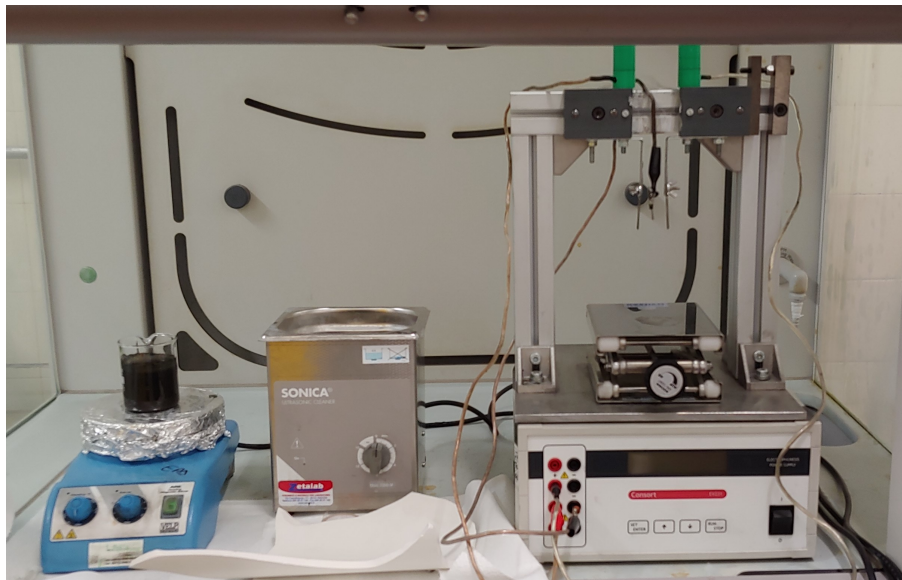


Figure 26: EPD layout

Oxidation kinetics were studied for each type of coating at Gdansk University of Technology. Four samples for each composition were employed to perform the thermogravimetric measurements.

Alumina rods were inserted in the 3 mm hole of each coupon to hang the samples in the oxidation furnace.

The test was carried out for 1000 h at 750 °C (120 °C/h ramps).

Every 250 h the samples mass change was measured. The mean value and the standard deviation of the mass gain was calculated for each composition.

ASR measurements were carried out with the ex-situ method with platinum contacts. Objects of this characterization were as-sintered and 1000 h aged coupons.

Platinum was applied over the samples and dried. Treated samples were inserted in a rig connected to an impedance measurement in order to collect data.

Starting from 750 °C, the ASR was measured during the cooling ramp until reaching 200 °C.

2.2 Pellets preparation

Pellets of Fe and Cu doped MCO were produced in order to measure the coefficient of thermal expansion (CTE) and evaluate the influence of doping for the thermomechanical properties of the spinel coating.

Powders of Fe_2O_3 , CuO and MCO were weighted and mixed in the same ratios as for the preparation of the EPD suspensions, respectively: 10Fe10CuMCO (10:10:80), 5Fe5CuMCO (5:5:90), 10Fe5CuMCO (10:5:85) and 5Fe10CuMCO (5:10:85).

Two further compositions were considered, in order to evaluate the effect of Fe or Cu doping alone on the coefficient of thermal expansion of MCO; these compositions are labelled 10FeMCO (10 wt.% of Fe_2O_3 , 90 wt.% of MCO) and 10CuMCO (10 wt.% of CuO , 90 wt.% of MCO).

Powders were weighted in proper amounts and mixed for 24h on rotating rollers. They were placed in alumina boxes and sintered in reducing (Ar/H_2 , 1000 °C, 2h) and oxidizing (air, 900 °C, 2h) atmosphere, following the same sintering treatment than the EPD coatings. The total amount of powders for each composition was 2.5 grams. Afterward, pellets were prepared pressing the sintered powders with the uniaxial press in Fig. 27.

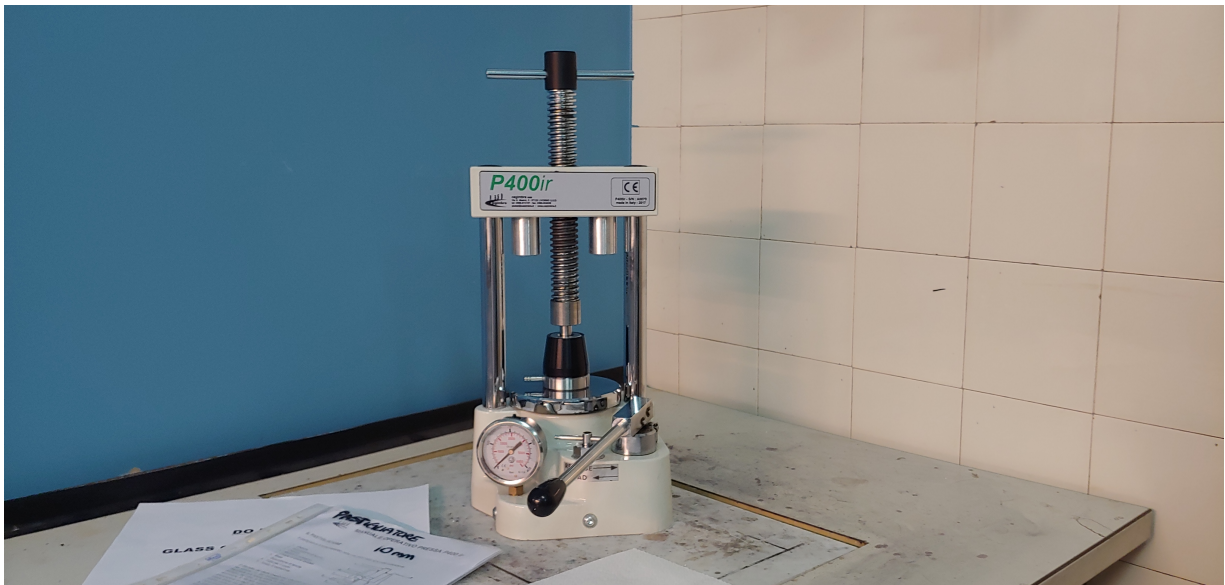


Figure 27: Uniaxial press for the production of pellets

The thickness researched was about 0.5 cm due to dilatometry tool requests. After the preparation an additional sintering in the air was performed for 5 hours at 1100 °C (3°C/min) and for 2 hours at 800°C for annealing (cooling ramp 2°C/min). Resulting pellets were without cracks and with compact surfaces.

After the preparation, thermomechanical properties of the materials produced were tested by dilatometry afterwards with a Netzsch DIL 402 PC/4 dilatometer to investigate the dilatation behavior over temperature. Results are shown in the following sections (3.1). In order to improve the precision of the results, four measurements per sample were carried out.

3 Results and discussion

3.1 Dilatometry

Thermomechanical compatibility is necessary to avoid cracks among the different materials composing the SOCs. Indeed, mechanical stresses can cause cracking or delamination during thermal cycles bringing to a break in the device. In particular, the interconnect-coating compatibility must be verified.

Dilatometric measurements had been carried out on 5 mm-thick pellets (section 2.2) to evaluate the coefficient of thermal expansion (CTE) in function of temperature, from room temperature to 900 °C.

Fig. 28 shows the dilatometric curves in function of the temperature for all samples. The behaviour of the measurements is almost linear most of the times, however a huge difference is visible in the MCO graphic.

The trend of MCO starts linearly until reaching about 450 °C, when the linear behavior is no more respected. This phenomenon happens due to the transition of MCO structure from cubic to tetragonal. This transition ends at about 650°C and the trend returns to be linear.

None of the Fe and Cu doped samples exhibit the transition, as the dilatometric curve shows a linear trend from low to high temperature.

From the measurements performed, mean coefficients of thermal expansion for different ranges of temperature are computed (Fig. 29).

In the calculation, low temperatures until 150 °C are not considered because can be affected by transitory events.

Besides the calculation of the overall CTE for each measurement, a low temperature range and a high temperature range are considered to allow a comparison of the thermomechanical properties in different conditions. Furthermore, the overall CTE take account of the cubic to tetragonal transition of the spinel.

MCO showed a mean CTE of $11.06 \times 10^{-6} K^{-1}$ while values referred to 150 - 400 °C and 650 - 900 °C were $11.73 \times 10^{-6} K^{-1}$ and $11.68 \times 10^{-6} K^{-1}$. According to these data, the difference is caused by the cubic to tetragonal transition; indeed mean CTE accounts for the range of temperature 400 - 650 °C in which the transition is verified. The other compositions did not showed this behavior.

What is visible is that CTEs are not so affected by temperature. CTEs between 150 - 400 °C are similar to those between 650 - 900 °C, even if slightly higher in all cases. This behavior is totally different from the one seen for CROFER 22 APU [44], strongly dependent on temperature. Indeed, CROFER CTEs go from $10.3 \times 10^{-6} K^{-1}$ at 200 °C to $12.7 \times 10^{-6} K^{-1}$ at 1000 °C [44].

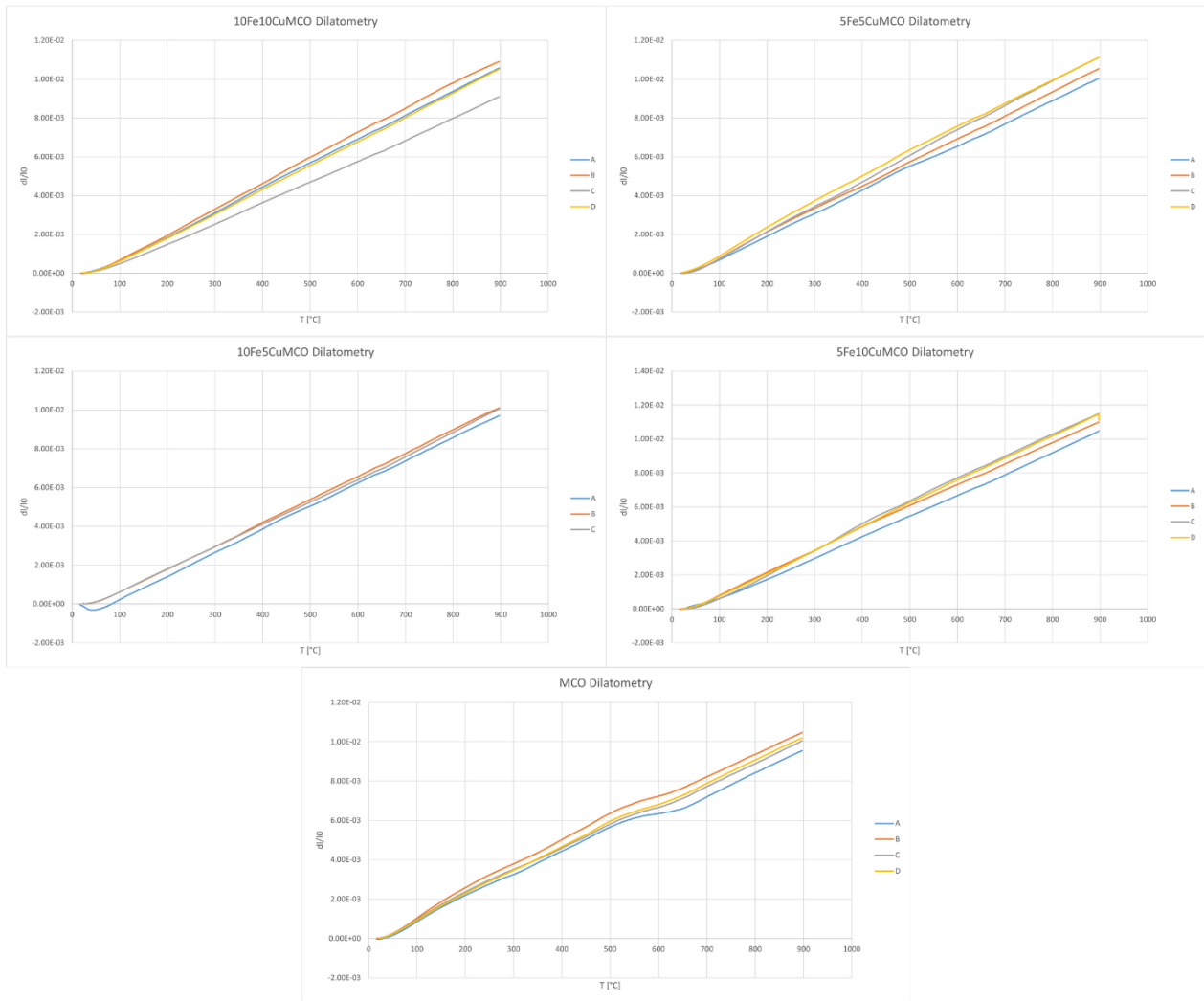


Figure 28: Dilatometric measurements

a) 10Fe10CuMCO			
Measure	CTE		
	150 - 900 °C	150-400 °C	650 - 900 °C
A	12.52E-06	12.91E-06	12.49E-06
B	12.99E-06	13.35E-06	12.54E-06
D	12.47E-06	12.44E-06	12.78E-06
Mean	12.66E-06	12.90E-06	12.60E-06

b) 5Fe5CuMCO			
Measure	CTE		
	150 - 900 °C	150-400 °C	650 - 900 °C
B	12.03E-06	12.02E-06	12.47E-06
C	12.98E-06	12.76E-06	12.73E-06
D	12.57E-06	13.42E-06	12.10E-06
Mean	12.53E-06	12.74E-06	12.43E-06

c) 10Fe5CuMCO			
Measure	CTE		
	150 - 900 °C	150-400 °C	650 - 900 °C
A	11.89E-06	12.13E-06	11.97E-06
B	11.99E-06	11.86E-06	12.14E-06
C	11.75E-06	11.50E-06	12.66E-06
Mean	11.87E-06	11.83E-06	12.26E-06

d) 5Fe10CuMCO			
Measure	CTE		
	150 - 900 °C	150-400 °C	650 - 900 °C
B	12.68E-06	13.32E-06	12.60E-06
C	13.75E-06	15.06E-06	12.85E-06
D	13.51E-06	13.87E-06	13.10E-06
Mean	13.31E-06	14.08E-06	12.85E-06

e) MCO			
Measure	CTE		
	150 - 900 °C	150-400 °C	650 - 900 °C
B	11.19E-06	12.17E-06	11.42E-06
C	10.80E-06	11.20E-06	11.78E-06
D	11.20E-06	11.83E-06	11.84E-06
Mean	11.06E-06	11.73E-06	11.68E-06

Figure 29: Coefficients of thermal expansion calculated for all compositions in different temperature ranges

The standard deviations of the measurements are shown in the following graphs (Fig 30). It can be seen from the standard deviations of each sample from the regression line that MCO shows large deviations in the cubic to tetragonal transition range, while this is not the case for other compositions. 5Fe5CuMCO has the highest standard deviations in the whole measurement, covering a wide range of CTEs due to probable inaccuracies. The other samples were stable and exhibit little deviations.

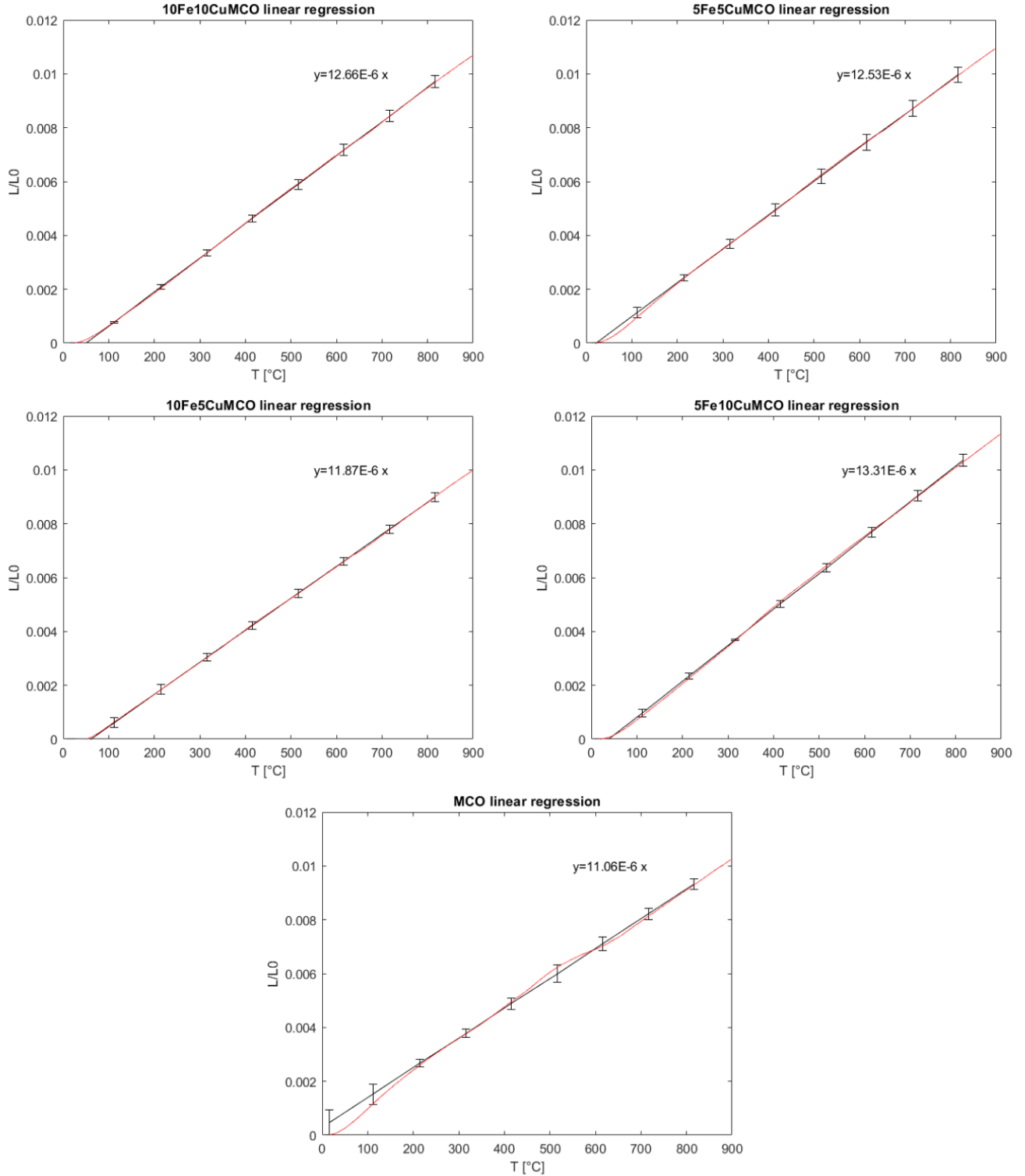


Figure 30: Mean trends of dilatometric measurements, errorbars refer to standard deviation

Fig. 31 shows the values of mean CTEs between 150 °C and 900 °C for each composition. The first important consideration concerns the difference among them.

10Fe10CuMCO and 5Fe5CuMCO have a similar value of about $12.5 \times 10^{-6} K^{-1}$, while 10Fe5CuMCO and 5Fe10CuMCO are very different especially from each other, showing respectively the following CTEs: $11.87 \times 10^{-6} K^{-1}$ and $13.31 \times 10^{-6} K^{-1}$. Increasing amounts of Fe leads to a decrease of thermal expansion coefficient, which raises at increasing amounts of Cu, instead. The same behavior and congruent values were seen in previous studies [45].

Furthermore, data suggest a possible incompatibility of 5Fe10CuMCO with the substrate due to too high CTE, while 10Fe5CuMCO and 5Fe5CuMCO are the most suitable. However, this has to be evaluated with post-mortem analysis of coated steel after aging.

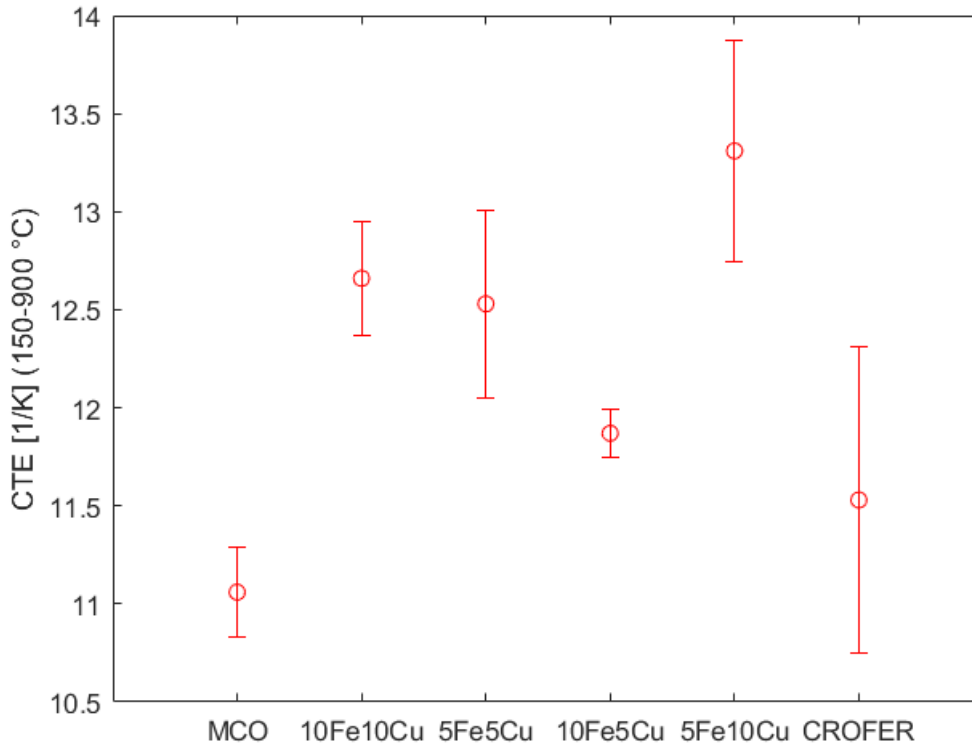


Figure 31: CTEs comparison in the range 150 - 900 °C

Fig. 23 exhibit CTEs variation vs temperature, in which 10FeMCO and 10CuMCO pellets are introduced. The most interesting aspects concern the large variation of MCO and 10FeMCO CTE in transition zone. MCO values went from a mean of $11 \times 10^{-6} K^{-1}$ below 500 °C to about $10.3 \times 10^{-6} K^{-1}$ over 650 °C, after the cubic to tetragonal transition.

The same behavior was reported by 10FeMCO. These results showed how Fe did not stabilize the cubic structure of MCO spinel, showing the cubic to tetragonal transition.

Moreover, 10FeMCO and 10CuMCO CTEs confirm the Fe and Cu influence on the thermo-mechanical properties of the spinel.

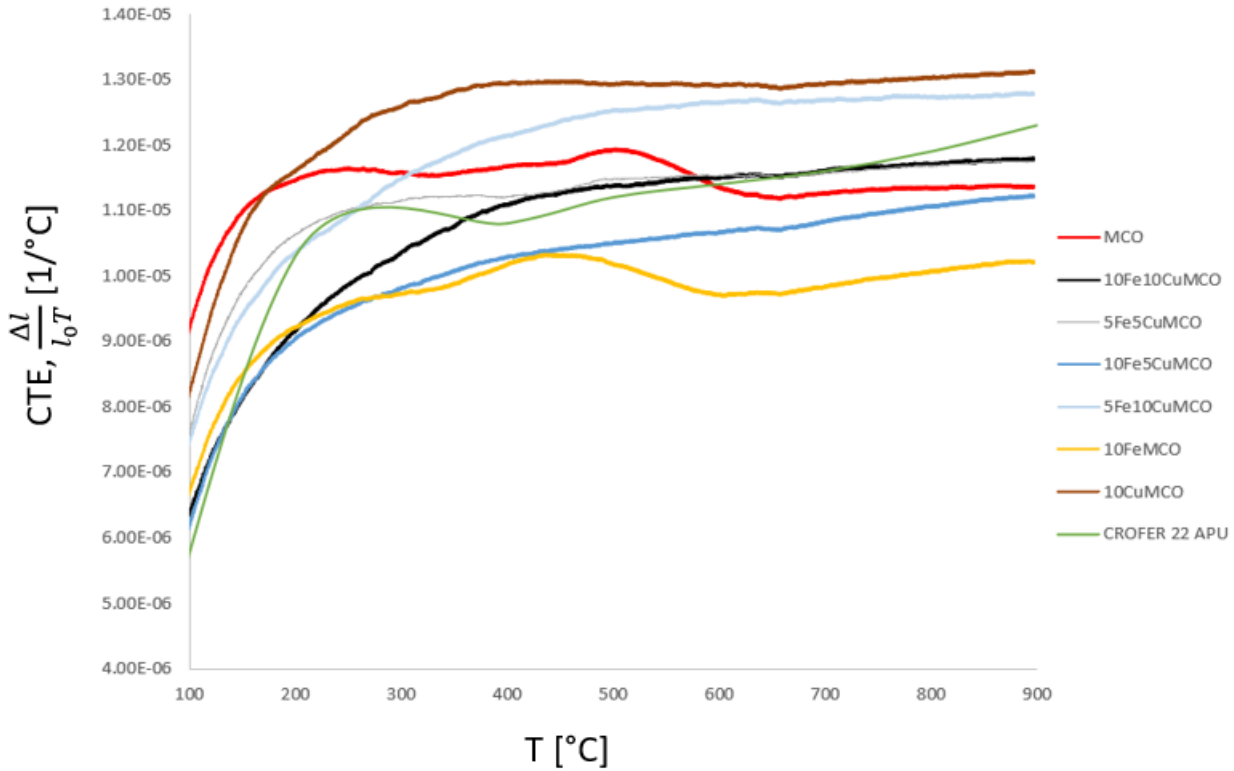


Figure 32: CTEs variation in function of temperature

3.2 X-Ray diffraction

Both reduced and re-oxidised samples were considered in the study.

Fig. 33 shows the comparison of XRD patterns of the reduced samples.

MnO peaks were detected in all the compositions while other phases have different behavior. During the reduction treatment, CuO was reduced to metallic Cu. Cu relative intensity is dependent on the amount of Cu inside the composition. 10Fe10CuMCO and 5Fe10CuMCO have the highest Cu peaks, while they are not present in pure MCO. This assessment is valid both on primary and secondary peaks. Fe phase is not visible with peaks, but its presence shifts Cobalt peaks to lower 2Theta according to the amount of Fe. 10Fe10CuMCO and 10Fe5CuMCO shows the most shifted cobalt peaks.

Fig. 34 reports XRD patterns of coatings for the as-sintered samples. Only pure MCO shows peaks of both cubic $Mn_1Co_2O_4$ and tetragonal $Mn_2Co_1O_4$.

All doped samples exhibited only the cubic structure peaks, thus meaning that Cu and Fe successfully entered the cubic structure of the MCO spinel, leading to its stabilization. Probably, this evidence is caused by high amounts of doping elements and the Cu effect. In previous studies [24] carried out on Fe-doped MCO coatings, both cubic and tetragonal structures were identified.

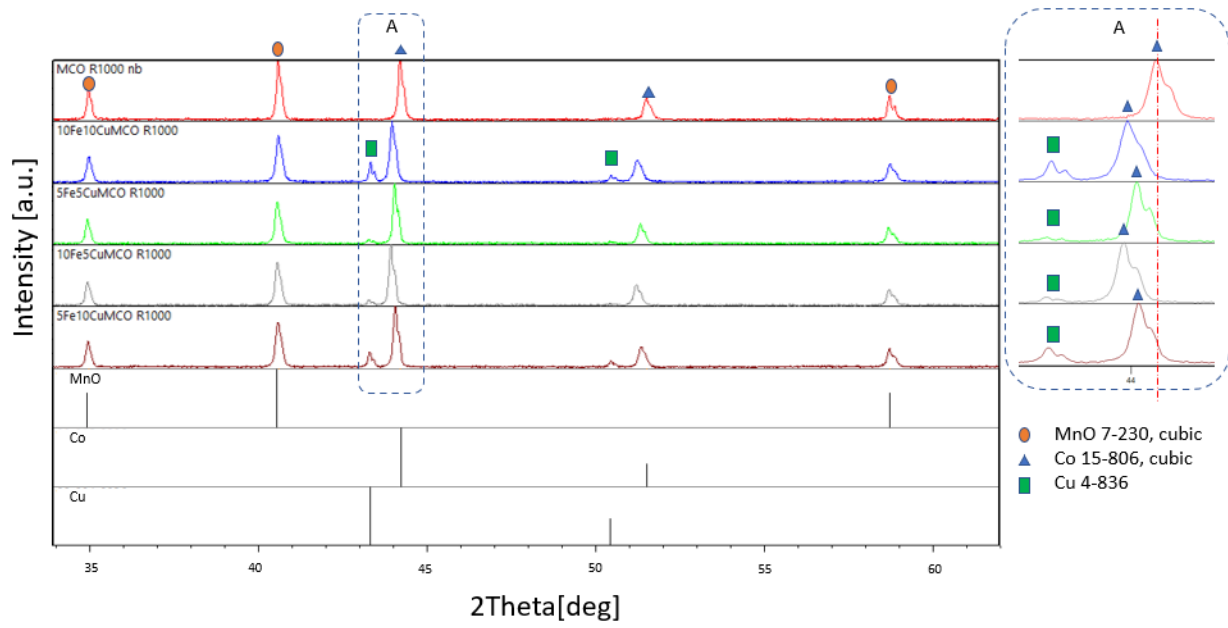


Figure 33: Comparison of XRD patterns after reduction

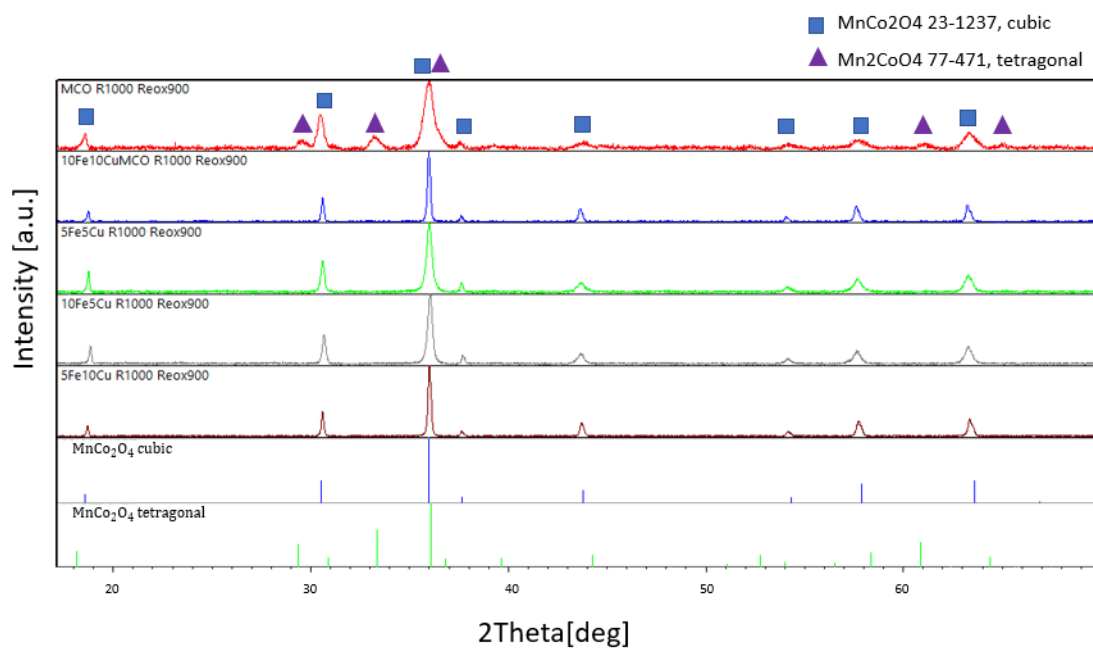


Figure 34: Comparison of XRD patterns after complete sintering process

3.3 SEM

Microstructure of both reduced and as-sintered samples were investigated by scanning electron microscopy (SEM) and energy dispersive X-ray spectroscopy (EDS).

Reduced samples

As pointed out by XRD analyses, the deposited precursors of the coating were completely reduced after the first sintering step, since no traces of MnO , Fe_2O_3 and CuO were detected.

Fig. 35 shows the cross sections of reduced samples in backscattered electrons mode. The thickness of the coating is in the range 10-15 μm , thus confirming that the co-deposition process was set in the proper way from this point of view. As confirmed by EDS analysis, black areas represent porosities, grey structures are referred to MnO and the white shapes point out metallic Co and Cu. Co particles have different sizes below 1 μm and their shape is irregular. Cu is smaller and present a spherical shape.

Fe is not detectable in metallic form, as already seen in XRD. But the Fe effect on the microstructure can be deduced. Indeed, It is apparent from the images that high at.% of Fe led to increased size of the brighter/white spots in the coatings (visible in Fig. 35 A and C). Instead, 5Fe5CuMCO R1000 and 5Fe10CuMCO R1000 (respectively in Fig. 35 B and D) show an higher amount of small particles of Co and Cu well distributed in the coating. In particular, Cu particles can be easily detected in the 5Fe10CuMCO R1000 case. It is worth mentioning that the same behavior of size increasing due to Fe was already presented in [24]. Furthermore, Fe influence on Co was already been demonstrated through the X-ray diffraction in the previous section.

Compared to the coatings that received only the oxidating thermal treatment presented in [24], metallic Co size was found larger in all coatings of this work because reduction at high temperature led to enhanced agglomeration.

Porosity was found to be quite uniform in all coatings without visible differences, but some large pores of about 2-3 μm can be detected in all cases.

Considering the EDS measurements, presented in Fig. 35 for each coating, Co mass percentage is always slightly higher than Mn. Interestingly, Fe and Cu percentages are congruent as they almost perfectly reflect the ratios between the precursors in EPD suspensions. However, they are slightly different from what expected, i.e. in 10Fe10CuMCO R1000 Fe and Cu percentages should be equal, but Fe is a little higher. This behavior is registered in all the measurements and could be likely due to a different efficiency of co-deposition.

Altogether, despite these differences the co-deposition was found to be very effective and all the elements are present in congruent percentages in the coating. The top views images of the reduced coatings shown in Fig. 38 present the microstructure from another point of view. Even in this case Cu shapes of about 0.1 μm are visible on MnO structures, while Co has different shapes and sizes. 5Fe5CuMCO R1000 (Fig. 36 B) appears to be the least dense, while in the other cases MnO structures are more defined and compact.

An additional image (Fig. 37) clearly shows the difference between Cu and Co particles; Cu is spherical and with smaller size.

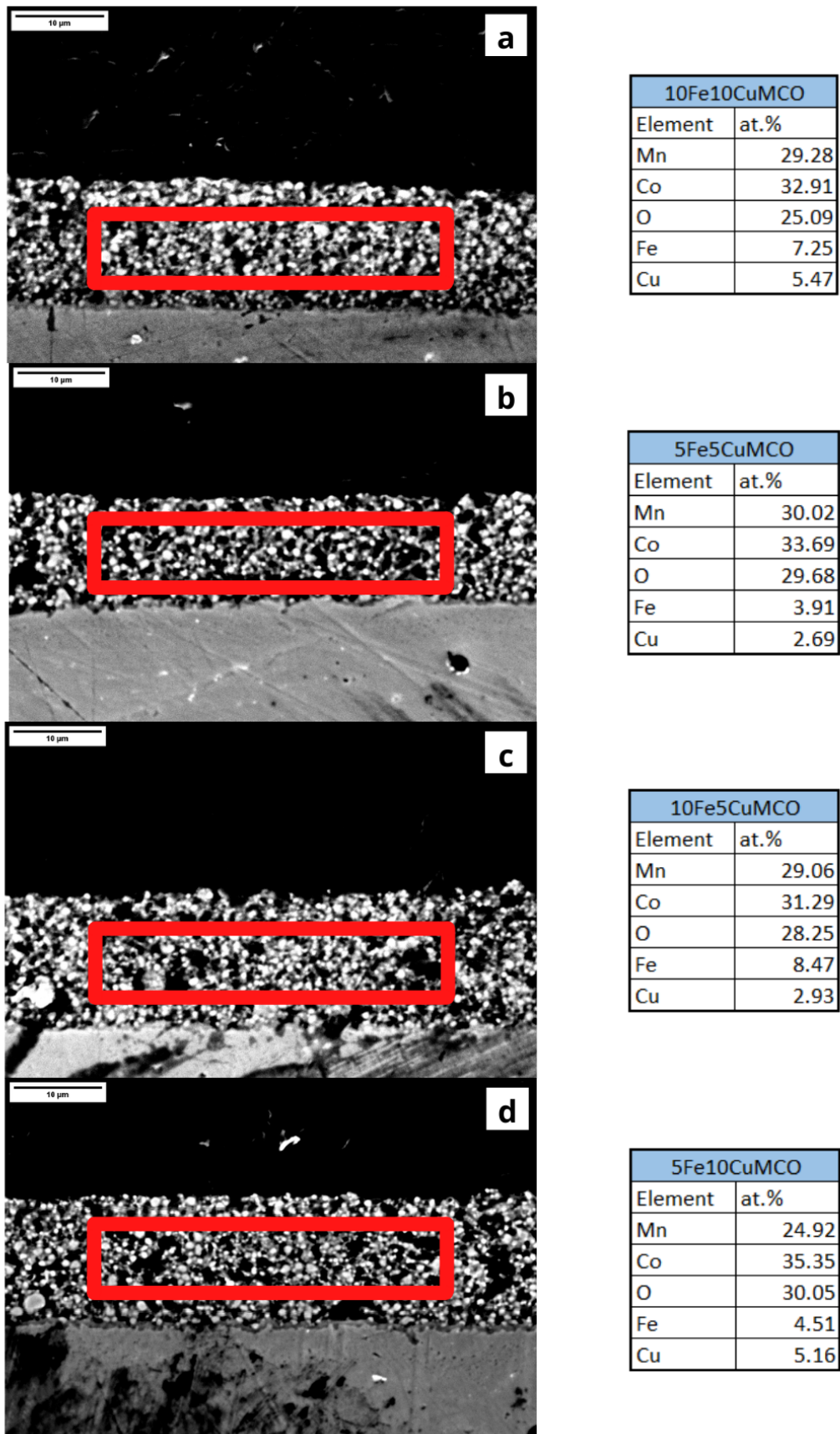


Figure 35: Cross section SEM images and EDS of reduced samples: a) 10Fe10CuMCO b) 5Fe5CuMCO c) 10Fe5CuMCO d) 5Fe10CuMCO

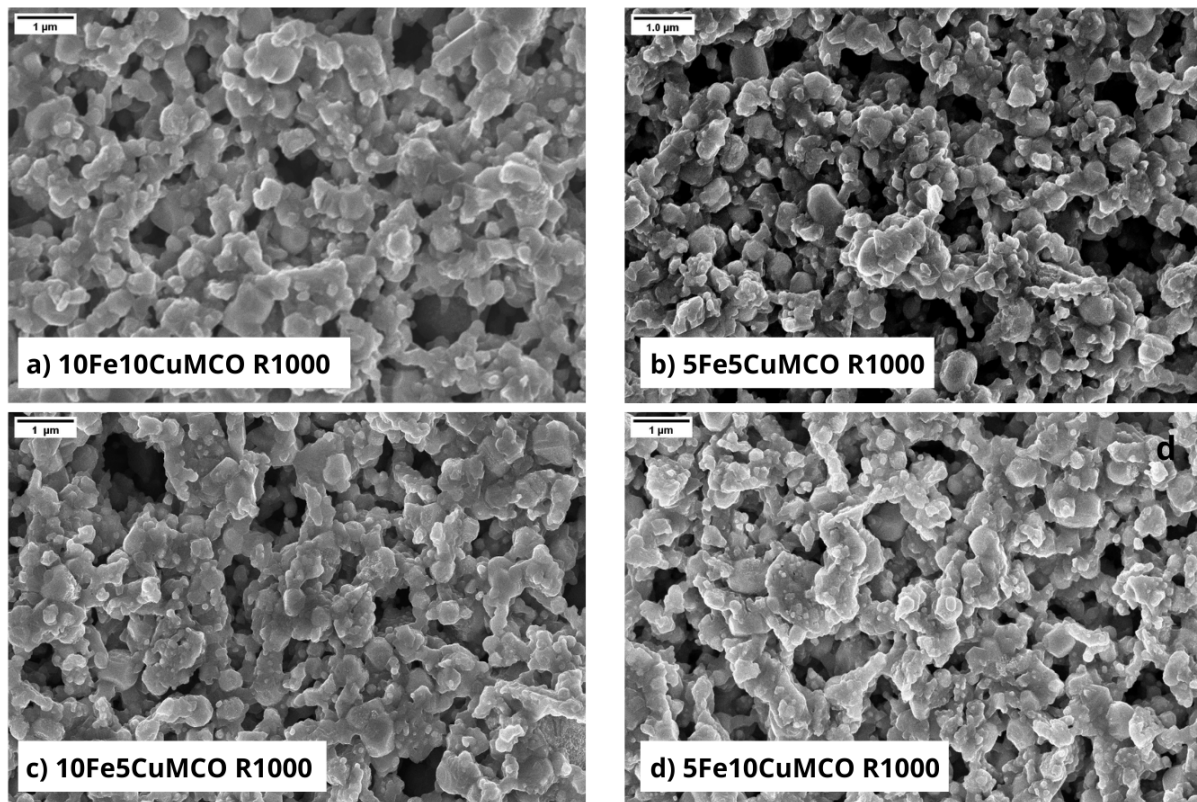


Figure 36: Top view SEM images of reduced samples

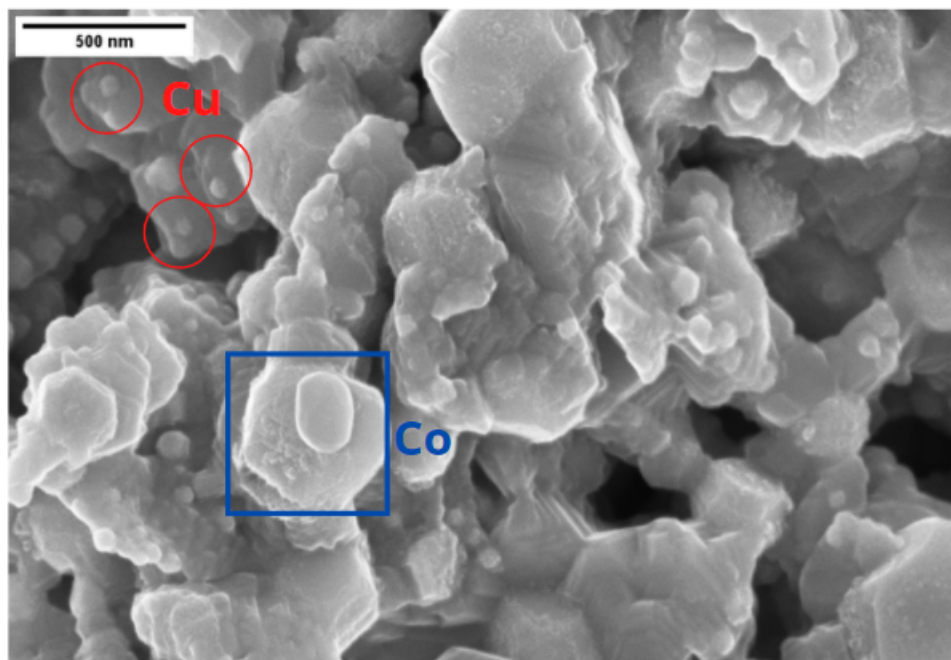


Figure 37: Top view SEM image of a 5Fe10CuMCO R1000 coating

Samples after re-oxidation step

Fig. 38 presents cross section images of the four coatings after 2 step sintering. All coatings are adherent to the substrate and do not show delamination or cracks at the interface with the steel substrate. Each of them presents a thin oxide scale at the steel-coating interface caused by high temperature oxidation during the two-step sintering. The thickness was found to be around 10 - 15 μm and it is close to the target of the electrophoretic co-deposition process, as already seen in reduced samples. Cu densification properties were reported in previous studies [2]. This behavior is confirmed in this work: the best densification is reached with the 5Cu10FeMCO R1000 Reox900 coating system.

Although in this coating the average porosity is very low, large pores of about 3 μm are present with a miscellaneous distribution. However, it is apparent that these are closed pores. The other samples show a more porous cross section, especially in presence of high amounts of Fe.

EDS presented in Fig. 38 do not exhibit the expected values. The following considerations regard all the coatings analyzed.

On contrary of what seen in reduced samples, Mn percentage is higher than the one of Co when their ratio should be by 1 to 1 ($Mn_{1.5}Co_{1.5}O_4$). This variation could be determined by Mn diffusion from the substrate to the coating during the oxidation sintering step or by residuals from the polishing. Furthermore, Fe and Cu percentages do not present exactly the expected relationship in atomic %: Fe concentration is always considerably higher than Cu foreseen. Even reduced samples showed this behavior, but the differences were less marked. Comparing EDS of different areas reported in Fig. 38, it can be noticed that Fe concentration in the coatings is respectively 9-10 at.% where the EPD suspension contained 10 at.% and 5-6 at.% when it was fixed at 5 at.% in the EPD suspensions. On the other hand, Cu reaches a maximum concentration of 5.5-6 at.% (instead of 10 at.% of EPD suspensions) and 2.5-3 at.% (instead of 5 at.%). These results are likely to be related to the lower tendency of CuO to deposit than Fe₂O₃ from the EPD suspensions. Compared to the EDS presented in Fig. 35 (reduced samples), oxygen percentage is risen due to the re-oxidation step.

The surface of coatings is presented in Fig. 39. As seen for the cross sections, the top view images show that 5Cu10FeMCO R1000 Reox900 exhibit the best densification, the surface is very compact and has few pores with heterogeneous distribution. In the other cases high porosity is detected with uniform distribution on the surface of the coatings. The worst densification is obtained in case of lower Cu relative amount (i.e. 10Fe5CuMCO coating). According to these considerations, Cu is a fundamental doping element in order to reach a good degree of densification of Mn-Co spinel coatings.

Fig. 40 is a top view image at increased magnification of the 5Cu10FeMCO R1000 Reox900 sample. It shows a compact doped MCO structure in which decomposed components (i.e. metallic Co, metallic Cu) obtained after the reduction are not visible. Fe and Cu are completely part of the spinel structure as doping elements.

Tetragonal phase is not detected in all samples, as already seen in sections 3.1 and 3.2. Thus, Fe and Cu doping and the high temperature two-step sintering stabilize the cubic phase.

For long-term operation, any possible microstructural changes of the coatings should be considered (at least after 1000 h).

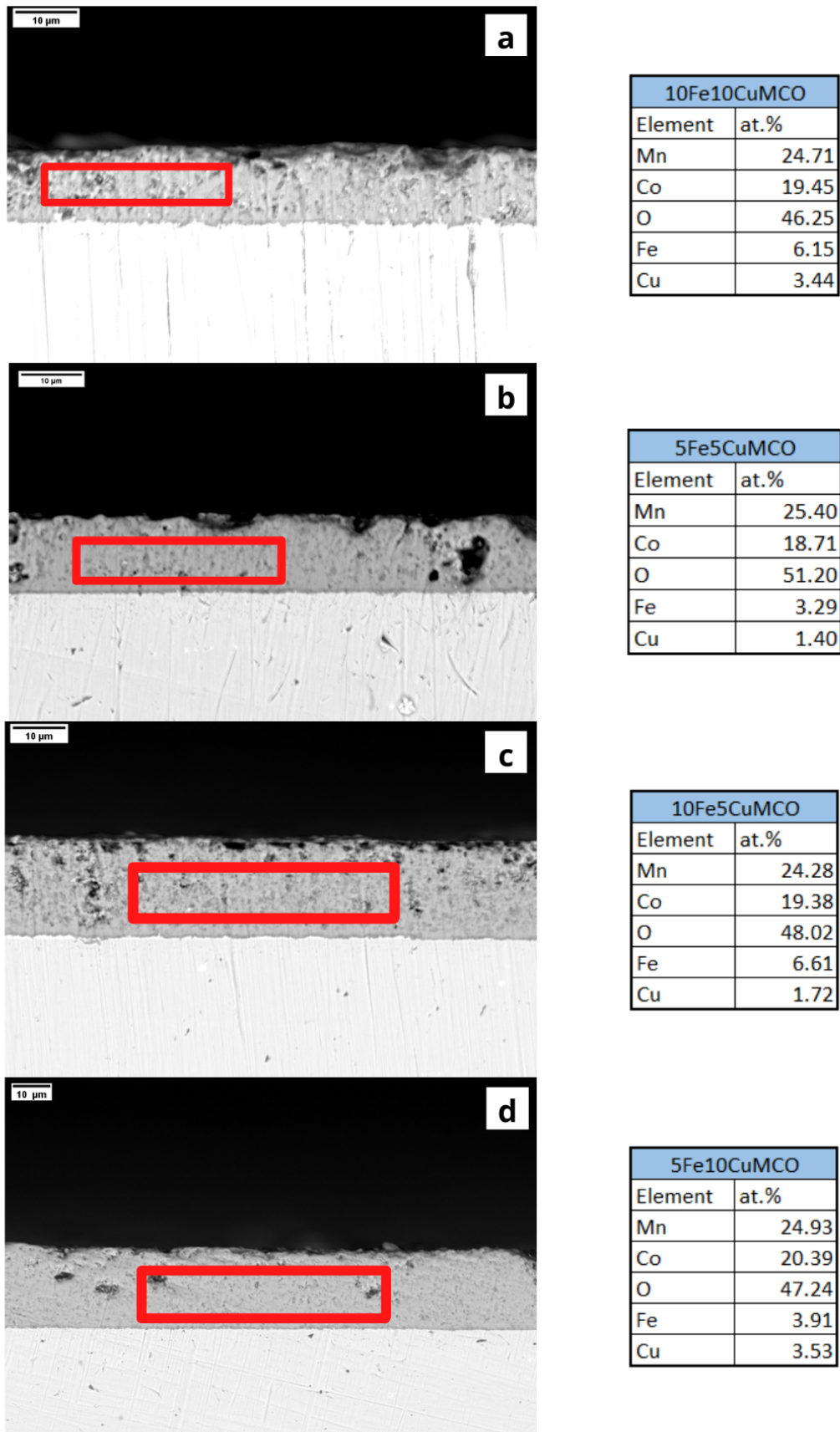


Figure 38: Cross section SEM images and EDS of as-sintered samples: a) 10Fe10CuMCO b) 5Fe5CuMCO c) 10Fe5CuMCO d) 5Fe10CuMCO

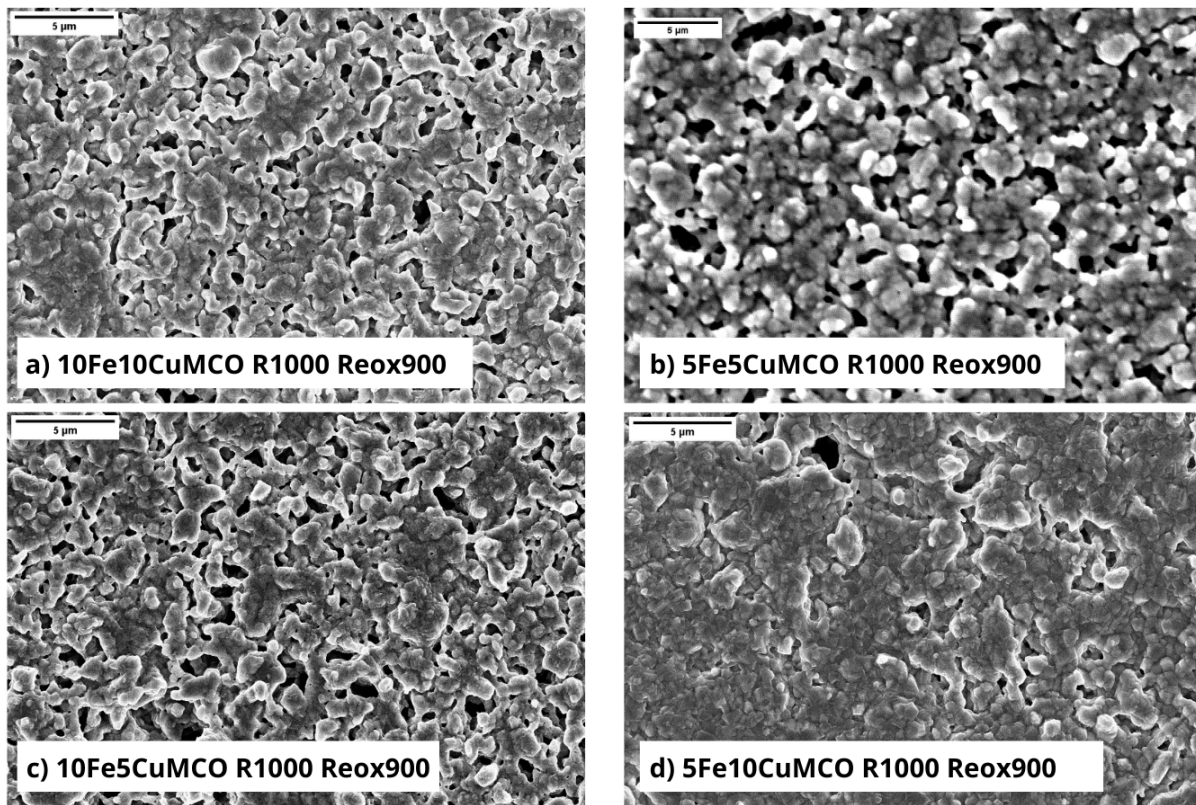


Figure 39: Top view SEM images of as-sintered samples

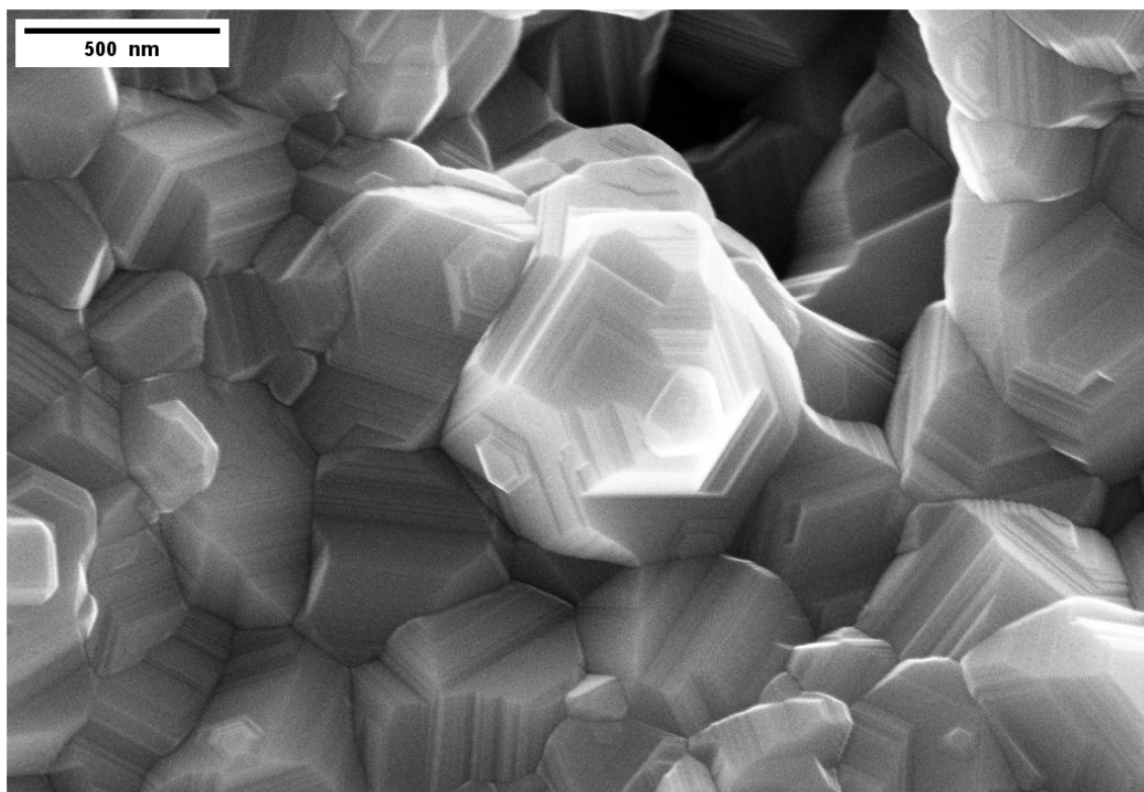


Figure 40: Top view SEM image of a 5Fe10CuMCO R1000 Reox900 coating

3.4 Characterization of as-sintered coating by transmission electron microscopy

Transmission electron microscopy (TEM) was performed on an ultrathin section (lamella) of the 10Fe10CuMCO in as-sintered state in order to investigate the nature of the interface between the metal substrate and the coating. The section was obtained by focused ion beam (FIB). TEM characterization was conducted in the International Centre of Electron Microscopy for Materials Science and Technology – AGH in Krakow (PL). Fig. 41 shows the TEM images obtained from the FIB lamella. In particular, Fig. 41 B presents the interface between the steel substrate and the coating.

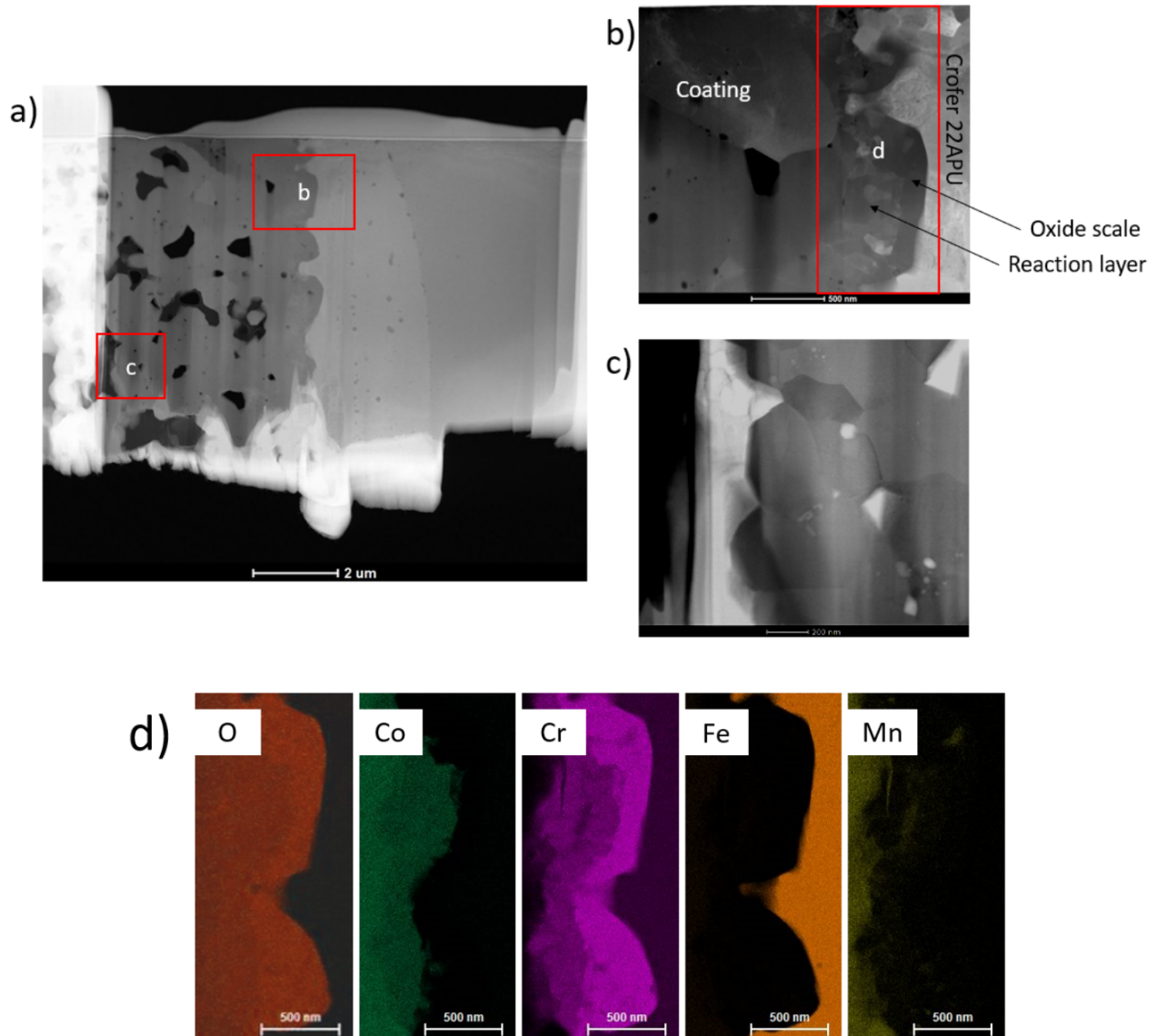


Figure 41: TEM images of as-sintered 10Fe10CuMCO coating on Crofer 22 APU: overview of the FIB lamella (a), CROFER 22 APU and coating interface (b), outer part of the coating (c), EDS elemental analysis of coating/Crofer 22 APU interface (d)

The darkest layer indicates the chromia scale, while a reaction layer can be found between the oxide scale and the coating. This is better visible in the insight of Fig. 41 D, where EDS elemental maps are reported. As visible in the maps, the reaction layer is rich in Cr and Co.

Fig. 41 C shows spinel grains in the outer part of the coating.

3.5 Thermogravimetric test

Data obtained from the thermogravimetric measurements are presented in Fig. 42, where the mean mass gain trends over time for all compositions is shown. Indeed, each point represents the mean among 4 samples measurements of the same type. Mass measurements were carried out every 250 h until reaching 1000 h.

A parabolic trend is expected as seen in 1.3.3, according to the following expression:

$$\left(\frac{\Delta m}{A}\right)^2 = 2k_{p,m} \cdot t + C$$

where $\Delta m [g]$ is the mass change, $A [cm^2]$ is the surface area, $k_{p,m} [g^2 cm^{-4} s^{-1}]$ is the parabolic oxidation rate, $t [s]$ is time and C is the integration constant.

The mass gain of the coatings is quite different. 10Fe10CuMCO shows a parabolic shape and the highest mass gain. 10Fe5CuMCO has the same behavior with a little lower values. 5Fe5CuMCO has a linear mass gain over time in this range, maybe more time is needed to reach a parabolic behavior. 5Fe10CuMCO has the lowest values near 1000 h, with a very variable trend.

The standard deviation is low for the 10Fe10CuMCO and 10Fe5CuMCO measurements, while quite high for the other 2 coatings.

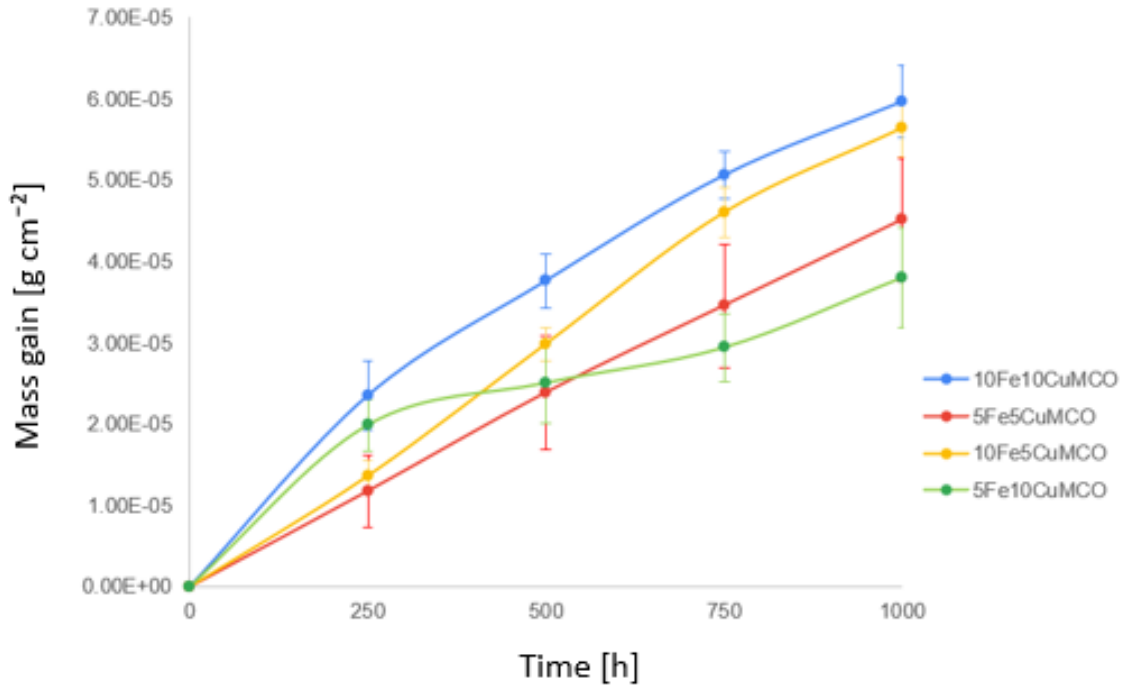


Figure 42: Mean mass gain of coated samples with error bars related to the standard deviations

To perform a better comparison among the coatings, the oxidation kinetics is studied as presented in 1.3.3.

To evaluate the parabolic behavior of the oxidation, the mass gain measurements are squared to obtain parabolic units; in this way, samples that exhibit a parabolic oxidation can be well approximated by a straight line. The resulting graph is shown in Fig. 43; parabolic units over time are reported for each composition and a regression line is calculated to fit the values.

Due to a low amount of data, the regression is not perfect for some of the coatings. 10Fe10CuMCO and 10Fe5CuMCO report $R^2 > 0,98$ (R^2 is the square of the correlation coefficient). Instead, 5Fe5CuMCO is slightly lower than the threshold value and 5Fe10CuMCO reach only an $R^2 = 0,94$. From these considerations it could be suggested that the oxidation trend is not fully parabolic; however, this set of samples is also the one exhibiting the lowest mass gain till 1000h. The calculation was performed above 250 h in order to avoid possible transient phenomena in the first 250 hours of the measurements.

From these considerations one can prove that the oxidation trend is not parabolic.

The calculation was performed above 250 h in order to avoid possible transient phenomena in the first hours of the measurements.

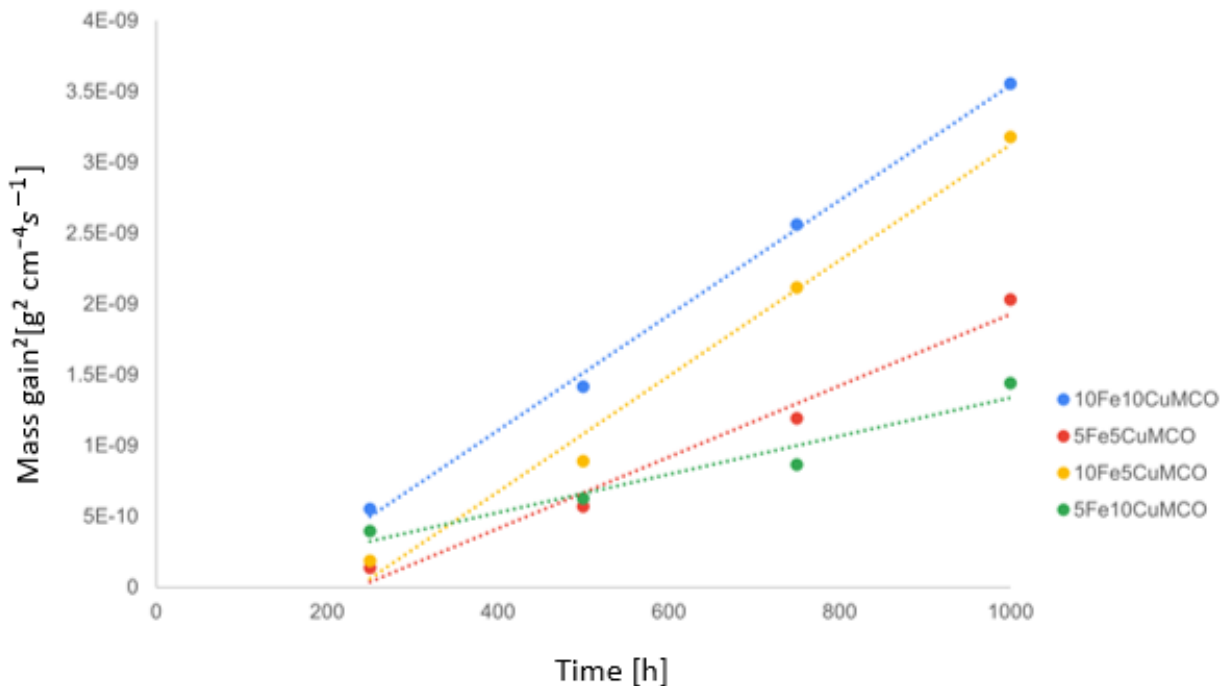


Figure 43: Parabolic rate plot with regression lines

From the regression lines the oxidation rates are calculated and presented in the table in Fig. 44.

The overall mass gain after the 1000 h test are shown in the same table.

Based on the mass gain till 1000 h aging, the theoretical oxide scale thickness can be calculated

with the following expression:

$$\tau_{\text{Cr}_2\text{O}_3} = \frac{MW_{\text{Cr}_2\text{O}_3}}{48 \cdot \rho_{\text{Cr}_2\text{O}_3}} \cdot \frac{\Delta m}{A}$$

where $\tau_{\text{Cr}_2\text{O}_3}$ is the oxide scale thickness, $MW_{\text{Cr}_2\text{O}_3}$ is the molar weight of Cr_2O_3 , 48 is the conversion factor that relate oxygen mass to the one of chromia and $\frac{\Delta m}{A}$ is the mass gain at 1000 h.

The use of this formula is related to the assumption that all the mass gain is caused by the oxygen uptake due to Cr oxidation. The other phenomena that could influence the mass gain are neglected in this calculation.

Calculated oxide scale thickness is reported in Fig 44.

Sample	Mass gain [mg cm^{-2}]	$k_{p,m}$ [$\text{g}^2 \text{cm}^{-4} \text{s}^{-1}$]	Oxide scale [μm]
10Fe10CuMCO	0.171	1.129E-15	0.104
5Fe5CuMCO	0.115	0.700E-15	0.070
10Fe5CuMCO	0.146	1.134E-15	0.089
5Fe10CuMCO	0.112	0.375E-15	0.068

Figure 44: Overall mass gain after 1000 h, parabolic oxidation rate and oxide scale thickness

The oxidation rates ($K_{p,m}$) of such coatings are very low compared to those seen in literature for similar applications [24][43]. Fe-doped MCO with 10 wt.% of Fe_2O_3 reached 3.3×10^{-15} after 2000h aging at 750°C , while the lowest value obtained in this work is 0.375×10^{-15} .

The best value is reached by the 5Fe10CuMCO coating, that even shows the lowest overall mass gain and the thinner oxide scale. The worst performances are obtained by the coatings with a high Fe concentration.

These results provide further support for the hypothesis that dense coatings provide a better oxidation resistance.

3.6 ASR test

This section presents the results obtained by the ASR test with Pt contacts of as-sintered and 1000 h aged samples.

Data obtained by the measurements from 200 to 750°C of the as-sintered samples are shown in Fig. 45.

All curves revealed a similar behavior with high ASR at low temperatures and progressively decreasing resistance with increasing temperature, as expected. 10Fe5CuMCO shows the highest values at low temperatures, 10Fe10CuMCO the lowest, 5Fe5CuMCO and 5Fe10CuMCO are almost overlapped.

From this graph it is not possible to detect correlations between the Fe and Cu contents and the ASR.

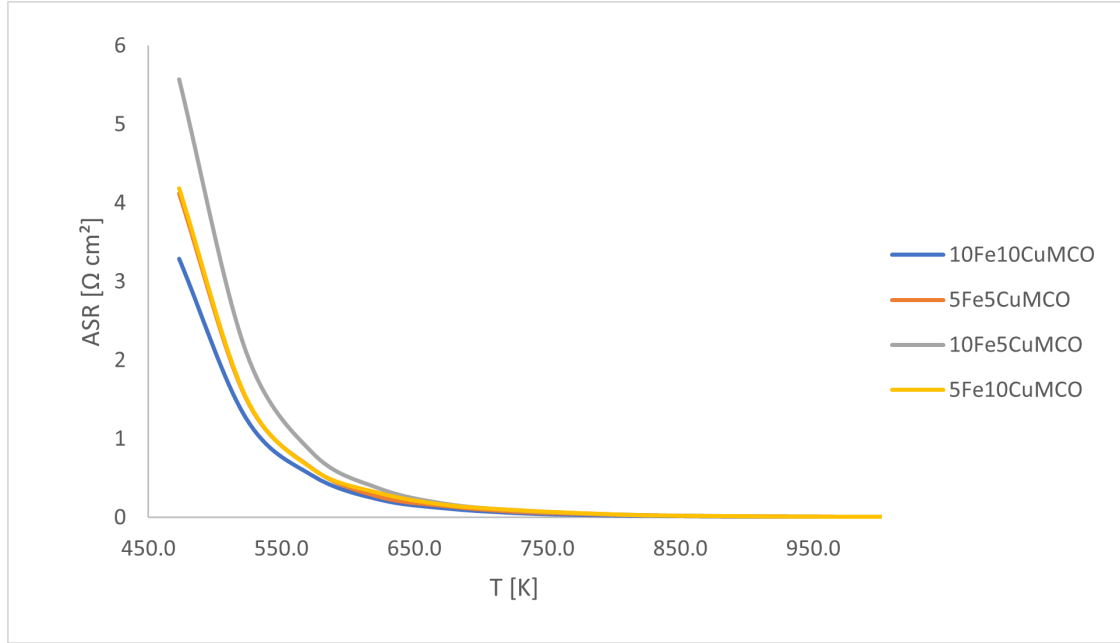


Figure 45: ASR over temperature (200 - 700 °C) of as-sintered samples

The ASR values at 750 °C of as-sintered samples are shown in Fig. 46.

The results show a different behavior at high temperature with respect to the trends at low temperature seen before. Indeed, 5Fe5CuMCO shows the lowest ASR ($5.6 \text{ m}\Omega \text{ cm}^2$) while 5Fe10CuMCO the highest value ($12.4 \text{ m}\Omega \text{ cm}^2$) and the other 2 compositions have intermediate values (i.e. $9.7 \text{ m}\Omega \text{ cm}^2$ for 10Fe5CuMCO and $5.6 \text{ m}\Omega \text{ cm}^2$ for 5Fe10CuMCO).

Interestingly, the lowest ASR values are reached by the compositions with the ratio Fe/Cu equal to 1, i.e. 10Fe10CuMCO and 5Fe5CuMCO; moreover, the best result is obtained by the coating with the lowest amount of doping elements, 5Fe5CuMCO.

In order to perform a more accurate analysis, the natural logarithm of ASR/T was plotted over the inverse of T and it reported in Fig. 47. In this way data can be characterized by a straight line and the slope can be used to calculate the activation energy for electrical conductivity (E_a), according to the Arrhenius law:

$$k = A e^{\frac{-E_a}{k_B T}}$$

where k is the rate constant, A is the pre-exponential factor, E_a is the activation energy, k_B is the Boltzmann constant and T is the temperature.

Only the temperature range of 600 - 750 °C was considered because other values deviate from the linear behavior. The activation energy computed for each sample is shown in Fig. 52.

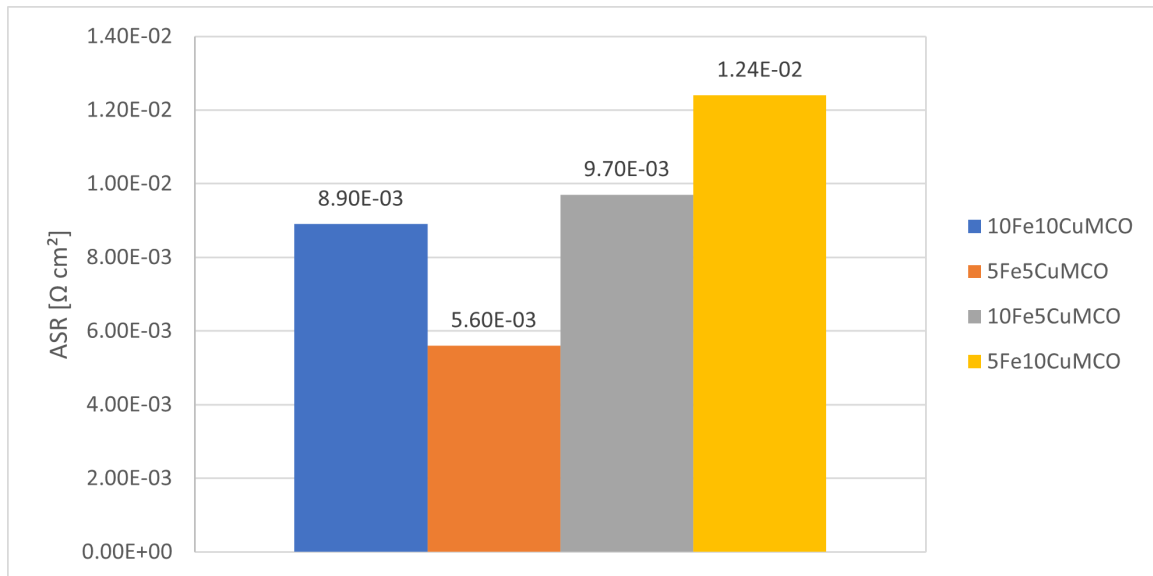


Figure 46: ASR measurements at operating temperature (750°C) of as-sintered samples

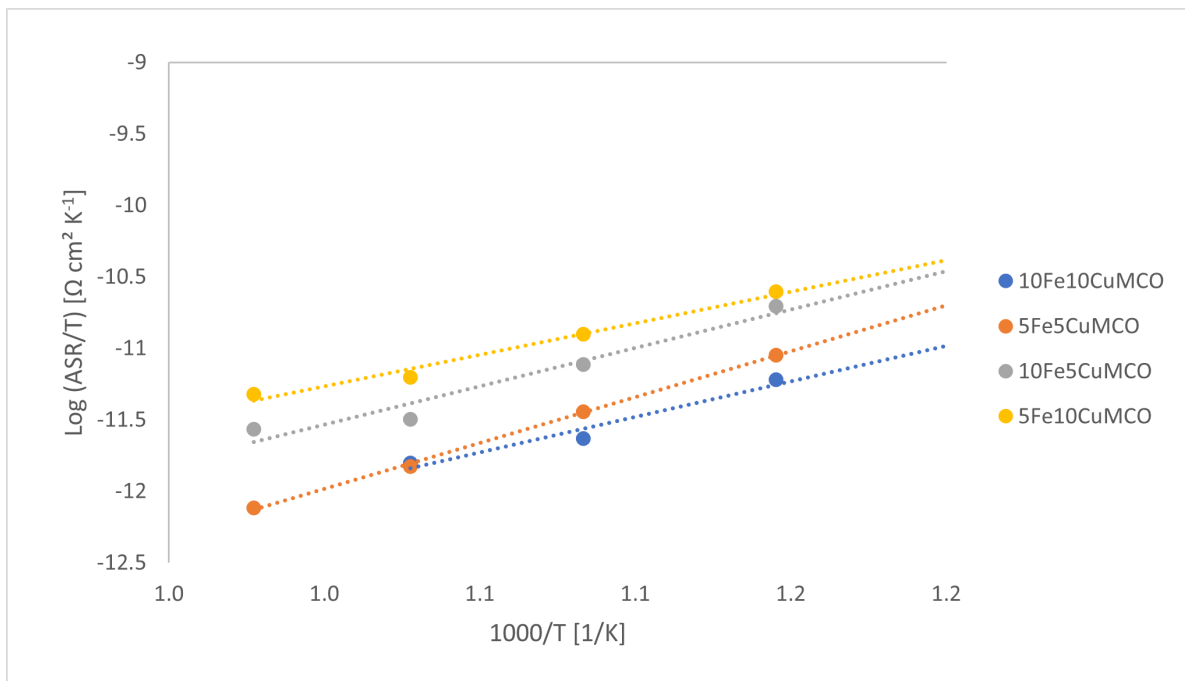


Figure 47: Natural logarithm of ASR/T plotted over the inverse of T with trend lines (600-750 °C) of as-sintered samples

The following part is dedicated to the ASR analysis of 1000 h aged samples.

The plots of ASR over T and ASR values at 750°C are reported respectively in Fig. 48 and Fig. 49. In principle, the ASR increase after 1000 h at 750°C has to be attributed to the thickening of the oxide scale during aging. However, the variation is generally limited for all the samples considered in this study. This evidence suggests that the coatings effectively limit the steel oxidation resulting in a low degradation rate.

As seen for the as-sintered case, the best performances are recorded by the samples in which Fe and Cu are balanced: the final ASR of 5Fe5CuMCO is $13.8 \text{ m}\Omega \text{ cm}^2$ (+8.2 $\text{m}\Omega \text{ cm}^2$ after

1000 h aging), while the one of 10Fe10CuMCO is $18.3 \text{ m}\Omega \text{ cm}^2$ ($+9.4 \text{ m}\Omega \text{ cm}^2$ after 1000h aging). The highest ASR is exhibited by 10Fe5CuMCO ($24.8 \text{ m}\Omega \text{ cm}^2$) with an increase of $+16.1 \text{ m}\Omega \text{ cm}^2$ compared to the as-sintered case. The 5Fe10CuMCO coating shows the highest ASR in the as-sintered case, but a quite low ASR increase after 1000 h at $750 \text{ }^\circ\text{C}$, i.e. $+9.9 \text{ m}\Omega \text{ cm}^2$.

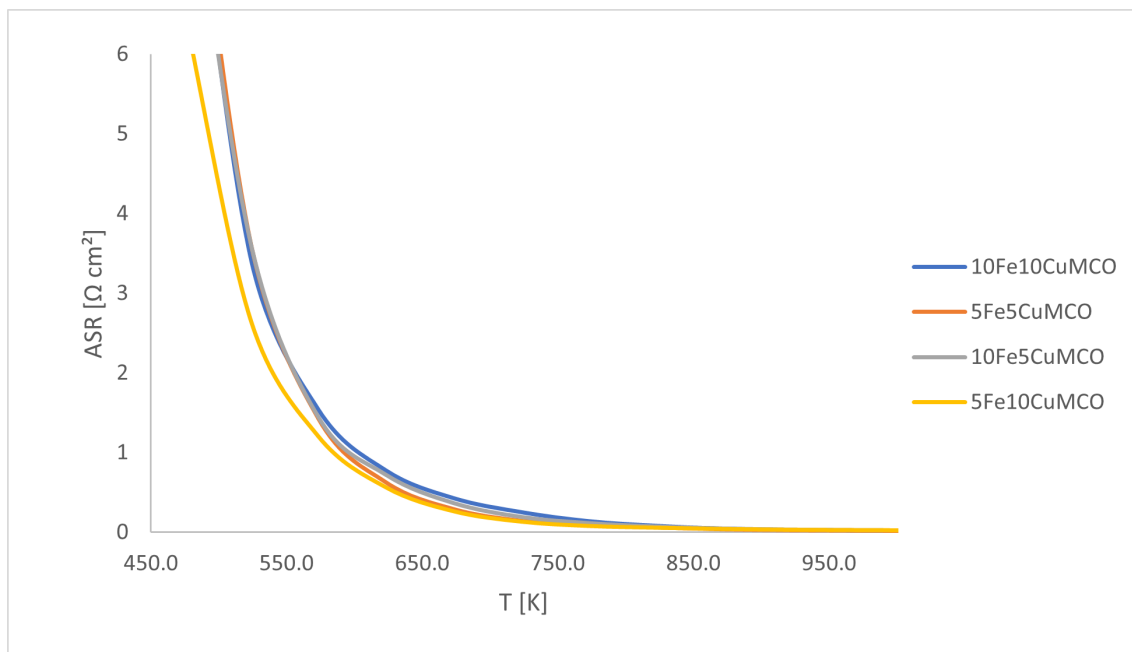


Figure 48: ASR (Pt contacts) over the inverse of T (200-700 $^\circ\text{C}$) of 1000 h samples

The plot of the natural logarithm of ASR/T over the inverse of T is shown in Fig. 50, together with the linear trend from 600 to 750°C . E_a computed following the Arrhenius law are reported in Fig. 51; the comparison with the as-sintered samples reveals that almost no variations in the activation energies happened after 1000 h aging. Only 10Fe10CuMCO coating exhibits a remarkable E_a increase (from 41.23 to 54.37 kJ/mol).

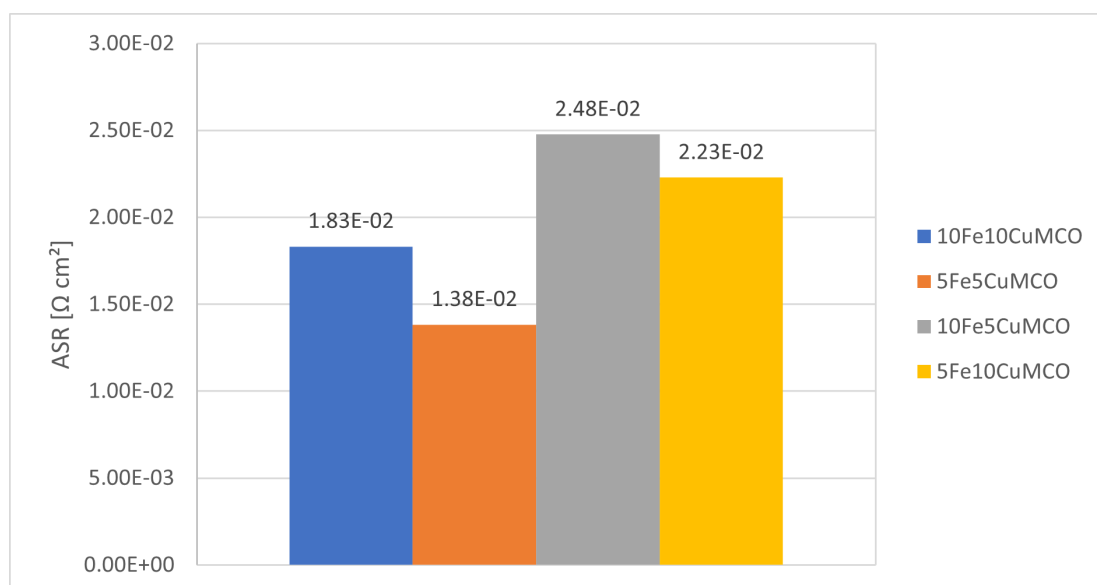


Figure 49: ASR measurements at operating temperature (750°C) of 1000 h samples

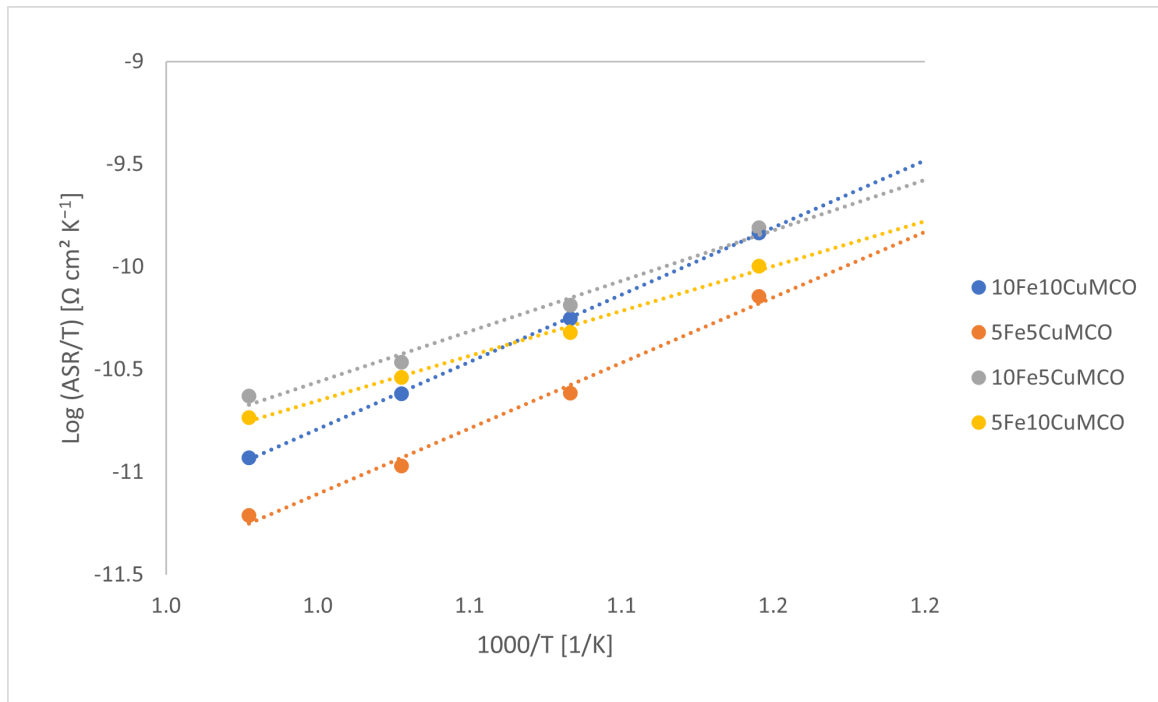


Figure 50: Natural logarithm of ASR/T plotted over the inverse of T with trend lines (600-750 °C) of 1000 h samples

	t = 0 h	t = 1000 h
Samples	E_a [kJ/mol]	E_a [kJ/mol]
10Fe10CuMCO	41.23	54.37
5Fe5CuMCO	53.37	53.04
10Fe5CuMCO	44.56	40.90
5Fe10CuMCO	36.66	36.33

Figure 51: Activation energy overview

3.7 Post-mortem microstructural characterization

Microstructure of the 1000 h aged samples were analysed by XRD and SEM.

The XRD measurements are shown in Fig. 52. Patterns are very similar to those of as-sintered samples. Only the cubic spinel was detected in all coatings as expected, thus proving the stability of the modified spinel.

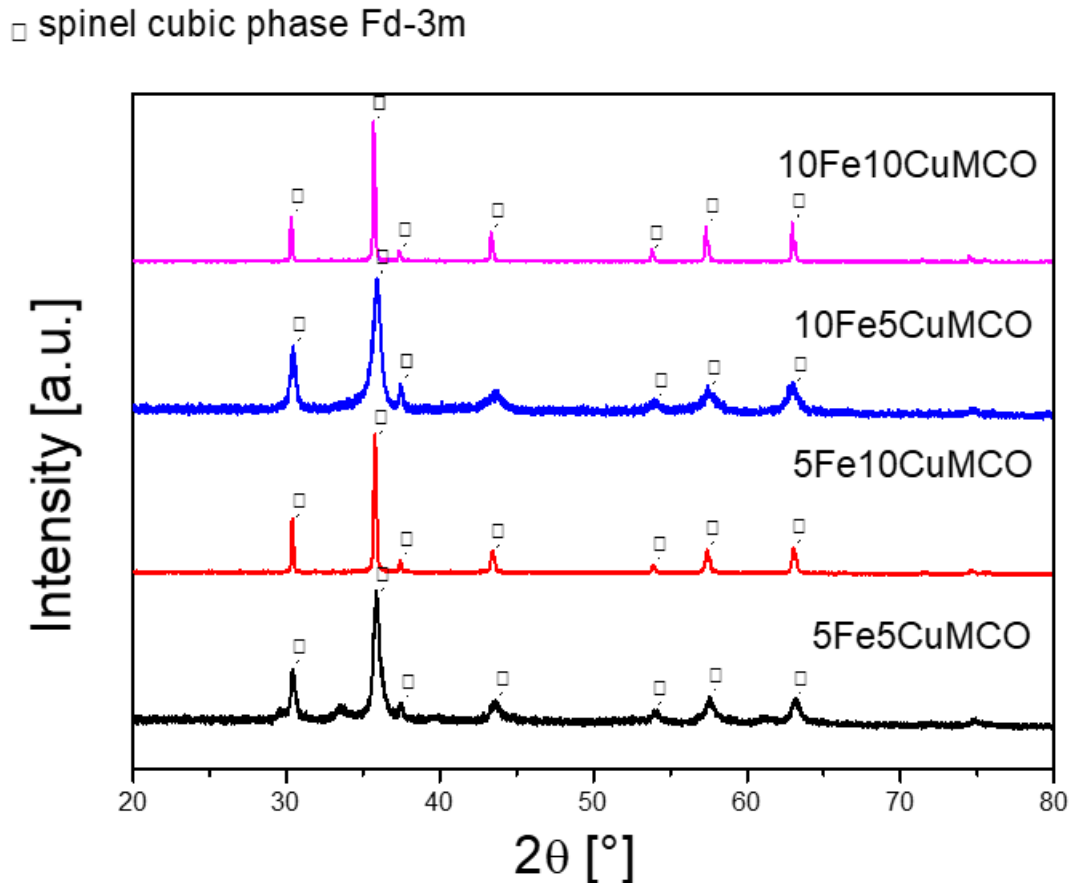


Figure 52: Comparison of XRD patterns of 1000 h aged coatings

Figures from 53 to 56 show the top-view SEM images and EDS elemental maps of all studied coatings after 1000 h at 750 °C. All coatings show a very uniform distribution of the elements on the surface. Chromium is not detected, suggesting that the Cr evaporation/diffusion was limited and had not reached the surface. EDS show the same evidences highlighted in as-sintered samples.

The higher degree of densification can be observed for the 10Fe10CuMCO sample, which presents a homogeneous surface with few pores.

Comparing the EDS of 1000 h aged and as-coated samples, aged samples present about 69 at.% of oxygen while as-sintered samples 50 at.%, demonstrating an oxygen uptake during the thermogravimetric test. The others elements follow the same relationships in both as-sintered and aged samples.

10Fe10CuMCO

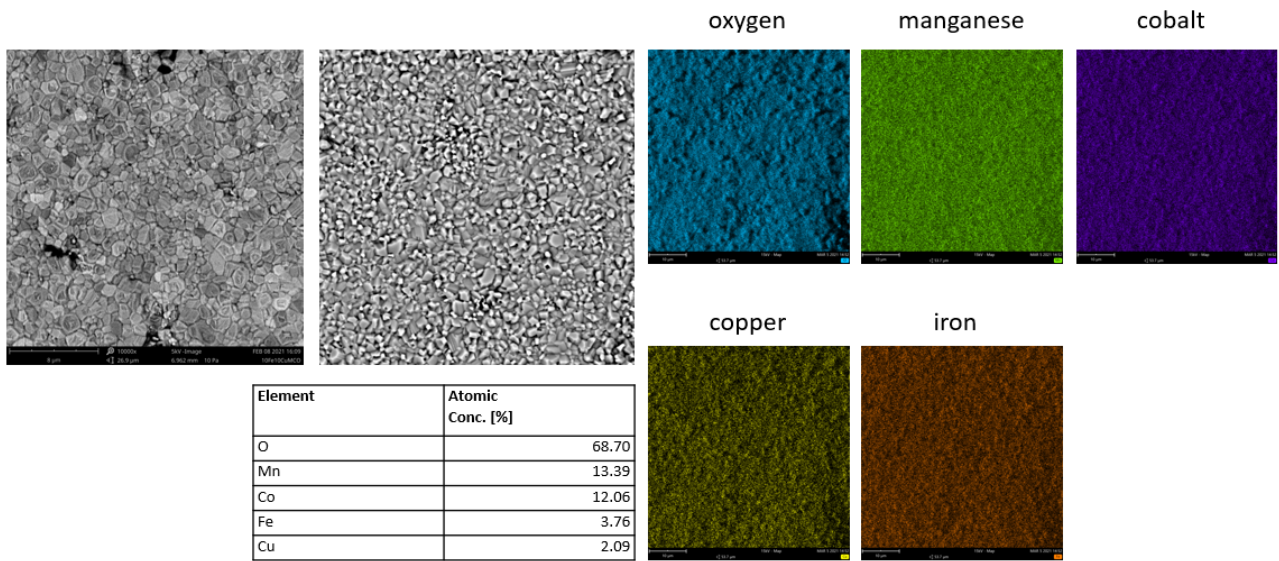


Figure 53: Top-view SEM images and EDS of 10Fe10CuMCO aged coating

5Fe5CuMCO

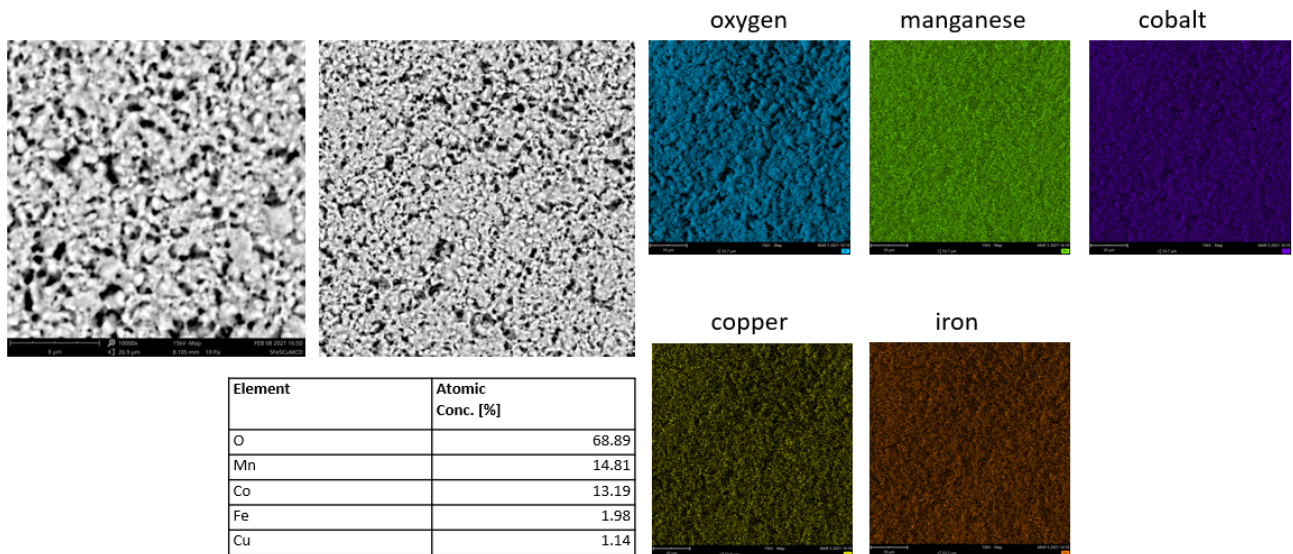


Figure 54: Top-view SEM images and EDS of 5Fe5CuMCO aged coating

10Fe5CuMCO

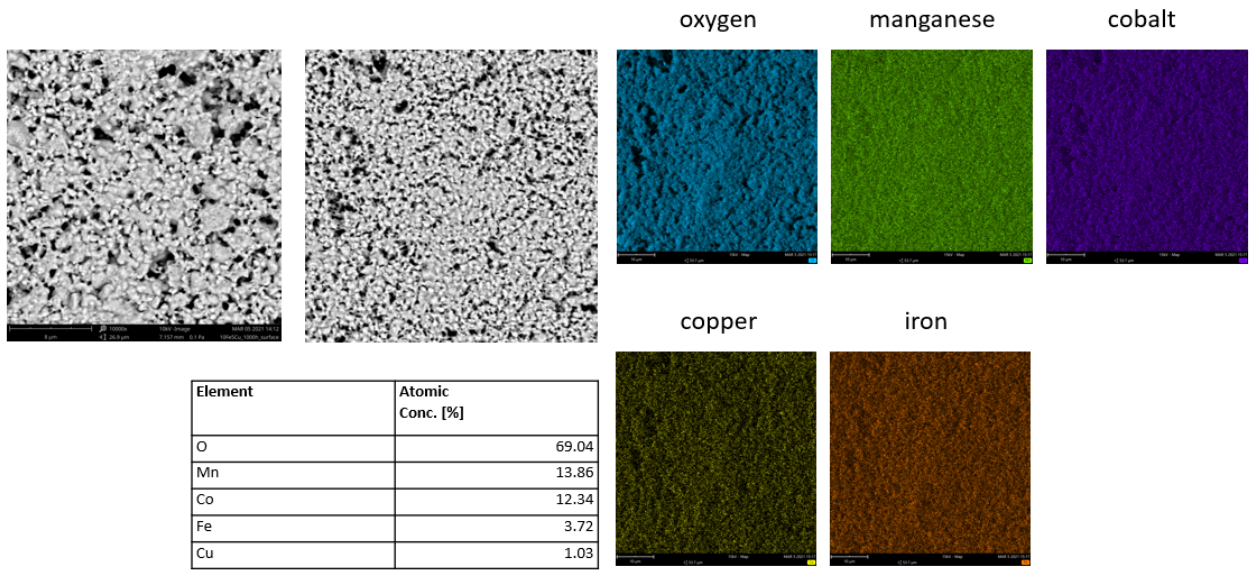


Figure 55: Top-view SEM images and EDS of 10Fe5CuMCO aged coating

5Fe10CuMCO

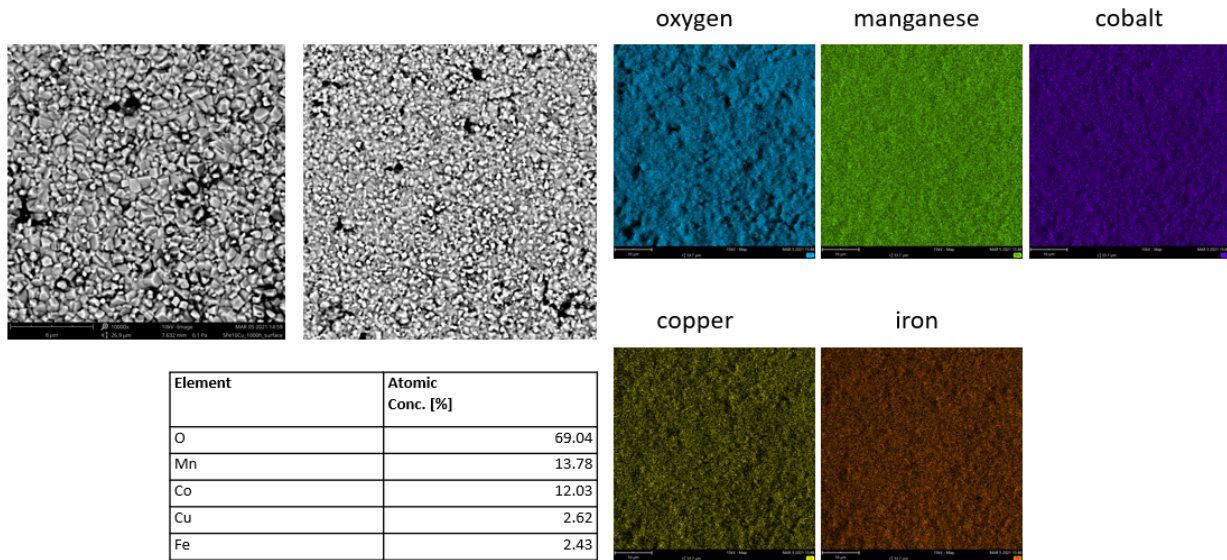


Figure 56: Top-view SEM images and EDS of 5Fe10CuMCO aged coating

4 Conclusions and future perspectives

The main objective of this MSc thesis was to set up and process an effective co-deposition of MCO spinel, Fe_2O_3 and CuO by electrophoretic method in order to obtain a Fe and Cu doped Mn-Co spinel coatings on a Crofer 22 APU metallic interconnect.

Cu and Fe-doped MnCo spinel powders are usually prepared “ex-situ”, i.e. before the deposition process. The use of EPD technique to simultaneously co-deposit the Mn-Co spinel and the dopants (Cu, Fe) by adding controlled amounts of the second phases (CuO and Fe_2O_3) to the suspension represents the novelty of this work.

The effect of simultaneous Cu and Fe-doping was reviewed and discussed with respect to structural, electrical properties, compositional changes and sintering behaviour of the as deposited and aged at 750°C coatings.

Fe and Cu doped Mn-Co coatings obtained after the EPD co-deposition and the heat treatments were found to be homogeneous, with reproducible thickness and without visible cracks. Both as-sintered and 1000 h aged samples (at 750°C) showed XRD peaks attributed to only the cubic phase of the spinel. No residues of the CuO and Fe_2O_3 precursors were detected. These results provide thus further support for the hypothesis that copper and iron becomes incorporated into the manganese cobaltite spinel lattice, thus stabilizing the cubic phase. The best densifications were reached by coatings with higher Cu amounts such as 5Fe10CuMCO. EDS investigations revealed that CuO deposits in a lower amount (with respect to Fe_2O_3) than expected during EPD.

Thermomechanical properties of as modified coatings were evaluated by dilatometry carried out on sintered pellets. The measurements showed that at increasing concentrations of Cu the CTE raises, while high amounts of Fe lead to a lower CTE compared to the undoped MCO spinel. The most compatible compositions with CROFER 22 APU (CTE= $11.7 \times 10^{-6} K^{-1}$) were found to be 10Fe10CuMCO (CTE= $12.66 \times 10^{-6} K^{-1}$), 5Fe5CuMCO (CTE= $12.53 \times 10^{-6} K^{-1}$) and 10Fe5CuMCO (CTE= $11.87 \times 10^{-6} K^{-1}$) respectively, while the 5Fe10CuMCO composition showed a too high CTE (CTE= $13.31 \times 10^{-6} K^{-1}$).

The oxidation analysis carried out by thermogravimetric test revealed that all the coatings were effective in limiting the oxide scale growth. In particular, again 5Fe10CuMCO showed the best behavior and a very low growth of the oxide scale (0.068 μm after 1000 h). The electric characterization showed good performances in all cases, after 1000 h all ASR slightly increased and the coatings with balanced Fe-Cu ratio obtained the best results, 18.3 $m\Omega cm^2$ for 10Fe10CuMCO and 13.8 $m\Omega cm^2$.

Post-mortem microstructural characterization exhibits the same properties (in terms of microstructure and composition) observed for as-sintered samples in XRD and SEM analysis, demonstrating a good thermal stability of the coatings. These results confirm that EPD is an effective and versatile method for SOCs protective coating applications and provide important insights into the critical role played by ceramic components in solid oxide cells performance and durability.

The results reported in this MSc thesis have significant implications for the understanding of how EPD can be used to design and produce new spinel compositions, especially taking advantage of the as described co-deposition doping and modification process. The findings in this thesis provide the following suggestion for future research: The evaluation of the oxidation

behavior by thermogravimetric test for 2000 h in order to study the evolution of the oxide scale in a long-term perspective, thus investigating more deeply the links between deposition method and long-term performance effects:

- An ‘in situ’ analysis of the ASR using LSM contacts, to reveal the behavior of the electrical performances over time;
- Deeper TEM characterization on both as-sintered and aged coatings by means of selected area electron diffraction (SAED) in order to investigate the effect of synergistic Fe and Cu doping on the crystalline structure of the spinel;
- Coatings on Crofer 22 APU could be tested at higher temperature (800-850 °C);
- A different substrate could be used to carry out the tests at lower temperature, such as: CROFER 22 H and AISI 441.

5 Bibliography

1. L. Besra, M. Liu, "A review on fundamentals and applications of electrophoretic deposition (EPD)"
2. S. Hu, W. Li, H. Finklea, X. Liu, "A review of electrophoretic deposition of metal oxides and its application in solid oxide fuel cells", *Advances in Colloid and Interface Science* 276 (2020) 102102
3. H. Hamaker, "Formation of a deposit by electrophoresis", *Trans Faraday Soc* 1940;35: 279–87
4. Y. Hirata, A. Nishimoto, Y. Ishihara, "Forming of alumina powder by electrophoretic deposition", *J Ceram Soc Jpn* 1991;99:108–13.
5. N. Heavens, "Electrophoretic deposition as a processing route for ceramics", Binner GP, editor. *Advanced ceramic processing and technology*, vol. 1. Park Ridge (NJ), USA: Noyes Publications; 1990. p. 255–83 [chapter 7].
6. L. Vandeperre, O. Van der Biest, W. Clegg, "Silicon carbide laminates with carbon interlayers by electrophoretic deposition", *Key Eng Mater* 1997;127:567–74 *Trans Tech Publ.*
7. J.S. Cherng, M.Y. Ho, T.H. Yeh, W.H. Chen, "Anode-supported micro-tubular SOFCs made by aqueous electrophoretic deposition", *Ceramics International* 38S (2012) S477–S480
8. R.W. Powers, "The electrophoretic forming of beta-alumina ceramic", *J Electrochem Soc* 1975;122:482–6.
9. R.N. Basu, C.A. Randall, M.J. Mayo, "Fabrication of dense zirconia electrolyte films for tubular solid oxide fuel cells by electrophoretic deposition", *J Am Ceram Soc* 2001;84(1):33–40.
10. M. Zunic, L. Chevallier, E. Di Bartolomeo, A. D'Epifanio, S. Licoccia, E. Traversa, "Anode supported protonic solid oxide fuel cells fabricated using electrophoretic deposition", *Fuel Cells* 2011;11:165–71.
11. Wang Y-C, Leu I-Chi, Hon M-H, "Kinetics of electrophoretic deposition for nanocrystalline zinc oxide coatings", *J Am Ceram Soc* 2004;87(1):84–8.
12. F. Smeacetto, A. De Miranda, S. Cabanas Polo, S. Molin, D. Boccaccini, M. Salvo, A.R. Boccaccini, "Electrophoretic deposition of $Mn_{1.5}Co_{1.5}O_4$ on metallic interconnect and interaction with glass-ceramic sealant for solid oxide fuel cells application", *Journal of Power Sources* Volume 280, 15 April 2015, Pages 379-386
13. A.G. Sabato, S. Molin, H.Javed, E. Zanchi, A.R. Boccaccini, F. Smeacetto, "In-situ Cu-doped $MnCo$ -spinel coatings for solid oxide cell interconnects processed by electrophoretic deposition", *Ceramics International* Volume 45, Issue 15, 15 October 2019, Pages 19148-19157
14. E. Zanchi, B. Talic, A.G. Sabato, S. Molin, A.R. Boccaccini, F. Smeacetto, "Electrophoretic co-deposition of Fe_2O_3 and $Mn_{1.5}Co_{1.5}O_4$: Processing and oxidation performance of Fe-doped Mn-Co coatings for solid oxide cell", *J. Eur. Ceram. Soc.* 39 (2019) 3768–3777

-
15. M. Bobruk, S. Molin, M. Chen, T. Brylewski, P.V. Hendriksen, "Sintering of $MnCo_2O_4$ coatings prepared by electrophoretic deposition", *Materials Letters* 213 (2018) 394–398
 16. B. Talic, H.Falk-Windisch, V. Venkatachalam, P.V. Hendriksen, K. Wiik, H.L. Lein, "Effect of coating density on oxidation resistance and Cr vaporization from solid oxide fuel cell interconnects", *Journal of Power Sources* 354 (2017) 57e67
 17. R. Sachitanand, M. Sattari, J.E. Svensson, J. Froitzheim, "Evaluation of the oxidation and Cr evaporation properties of selected FeCr alloys used as SOFC interconnects", *international journal of hydrogen energy* 38 (2013) 15328-15334
 18. H. Falk-Windisch, J. E. Svensson, J. Froitzheim, "The effect of temperature on chromium vaporization and oxide scale growth on interconnect steels for Solid Oxide Fuel Cells", *Journal of Power Sources* 287 (2015) 25-35
 19. Opila EJ, Myers DL, Jacobson NS, Nielsen IMB, Johnson DF, Olminky JK, "Theoretical and experimental investigation of the thermochemistry of $CrO_2(OH)_2(g)$ ", *J Phys Chem A* 2007;111:1971-80
 20. K. Hilpert, D. Das, M. Miller, D. H. Peck and R. Weiß , "Chromium Vapor Species over Solid Oxide Fuel Cell Interconnect Materials and Their Potential for Degradation Processes", *Journal of The Electrochemical Society*, Volume 143, Number 11
 21. C. Gindorf, L. Singheiser, K. Hilpert, "Vaporisation of chromia in humid air", *Journal of Physics and Chemistry of Solids* 66 (2005) 384–387
 22. P. Kofstad, "High Temperature Corrosion" Elsevier Science Publishing Co. Inc., 1988
 23. S. Chevalier, "Mechanisms and Kinetics of Oxidation" A2. In B. Stott, M. Cottis, R. Graham, S. Lindsay, T. Lyon, D. Richardson, and H. Scantlebury, editors, "Shreir's Corrosion", pages 132–152. Elsevier, Oxford, 2010
 24. B. Talic, PhD Thesis, "Metallic Interconnects for Solid Oxide Fuel Cells: High Temperature Corrosion and Protective Spinel Coatings", vol. 7. 2016
 25. Alton T. Tabereaux, Ray D. Peterson, "Treatise on Process Metallurgy: Industrial Processes", 2014
 26. J. G. Grolig, "Coated Ferritic Stainless Steels as Interconnects in Solid Oxide Fuel Cells", 2013
 27. Mansoo Park, Ji-Su Shin, Sanghyeok Lee, Hyo-Jin Kim, Hyegsoon An, Ho-il Ji, Hyoungchul Kim, Ji-Won Son, Jong-Ho Lee, Byung-Kook Kim, Hae-Weon Lee, Kyung Joong Yoon, "Thermal degradation mechanism of ferritic alloy (Crofer 22 APU)", *Corrosion Science* 134 (2018) 17–22
 28. Y. Zhang, A. Javed, M. Zhou, S. Liang, P. Xiao, "Fabrication of Mn–Co Spinel Coatings on Crofer 22 APU Stainless Steel by Electrophoretic Deposition for Interconnect Applications in Solid Oxide Fuel Cells", *International Journal of Applied Ceramic Technology* Volume 11, Issue 2 p. 332-341
 29. N.J. Magdefrau, L. Chen, E.Y.Suna, M. Aindow, "Effects of alloy heat treatment on oxidation kinetics and scale morphology for Crofer 22 APU", *Journal of Power Sources* 241 (2013) 756-767

-
30. R. Sachitanand, M. Sattari, J. E. Svensson, J. Froitzheim, "Evaluation of the oxidation and Cr evaporation properties of selected FeCr alloys used as SOFC interconnects", international journal of hydrogen energy 38 (2013) 15328-15334
 31. J. G. Grolig, J. Froitzheim, J.E. Svensson, "Coated stainless steel 441 as interconnect material for solid oxide fuel cells: Evolution of electrical properties", Journal of Power Sources 284 (2015) 321e327
 32. W.Z. Zhu, S.C. Deevi, "Opportunity of metallic interconnects for solid oxide fuel cells: a status on contact resistance", Materials Research Bulletin 38 (2003) 957–972
 33. X. Chen, P.Y. Hou, C. P. Jacobson, S. J. Visco, L. C. De Jonghe, "Protective coating on stainless steel interconnect for SOFCs:oxidation kinetics and electrical properties", Solid State Ionics 176 (2005) 425–433
 34. S. Megel, E. Girdauskaite, V. Sauchuk, M. Kusnezoff, A. Michaelis,"Area specific resistance of oxide scales grown on ferritic alloys for solid oxide fuelcell interconnects", J. Power Sources 196 (2011) 7136e7143
 35. P. Piccardo, P. Gannon, S. Chevalier, M. Viviani, A. Barbucci, G. Caboche,R. Amendola, S. Fontana, "ASR evaluation of different kinds of coatings on a ferritic stainless steel as SOFC interconnects", Surf. Coatings Technol. 202 (2007) 1221e1225
 36. S. Fontana, R. Amendola, S. Chevalier, P. Piccardo, G. Caboche, M. Viviani, R. Molins, M. Sennour," Metallic interconnects for SOFC: Characterisation of corrosion resistance and conductivity evaluation at operating temperature of differently coated alloys" J. Power Sources 171 (2007) 652e662
 37. B. Hua, J. Pu, F. Lu, J. Zhang, B. Chi, L. Jian,"Development of a Fe–Cr alloy for interconnect application in intermediate temperature solid oxide fuel cells", J. Power Sources 195 (2010)2782e2788
 38. K. Huang, P.Y. Hou, J.B. Goodenough,"Reduced area specific resistance for iron-based metallic interconnects by surface oxide coatings", Mater. Res. Bull. 36 (2001) 81e95
 39. S. Molin, B. Kusz, M. Gazda, P. Jasinski, "Protective coatings for stainless steel for SOFC applications", J. Solid State Electrochem. 13 (2009) 1695e1700
 40. I. Antepará, I. Villarreal, L.M. Rodríguez-Martínez, N. Lecanda, U. Castro, A. Laresgoiti, "Evaluation of ferritic steels for use as interconnects and porous metal supports in IT-SOFCs", J. Power Sources 151 (2005) 103e107
 41. P. Wei, X. Deng, M.R. Bateni, A. Petric, "Oxidation and Electrical Conductivity Behavior of Spinel Coatings for Metallic Interconnects of Solid Oxide Fuel Cells", Corrosion 63 (2007) 529e536
 42. S. Molin, A.G. Sabato, M. Bindi, P. Leone, G. Cempura, M. Salvo, S. Cabanas Polo, A.R. Boccaccini, F. Smeacetto, "Microstructural and electrical characterization of Mn-Co spinel protective coatings for solid oxide cell interconnects", J. Eur. Ceram. Soc. 37 (2017) 4781–4791
 43. S. Molin, A.G. Sabato, H. Javed, G. Cempura, A.R. Boccaccini, F. Smeacetto, "Codeposition of CuO and $Mn_{1.5}Co_{1.5}O_4$ powders on Crofer22APU by electrophoretic method: Structural, compositional modifications and corrosion properties", Materials Letters 218 (2018) 329–333

-
44. VDM Crofer 22 APU, "Material Data Sheet No. 4046"
 45. B. Talic, P. V. Hendriksen, K. Wiik, H. L. Lein, "Thermal expansion and electrical conductivity of Fe and Cu doped $MnCo_2O_4$ ", *Solid State Ionics* 326 (2018) 90–99
 46. European Commission, "A Clean Planet for all - A European long-term strategic vision for a prosperous, modern, competitive and climate neutral economy", 2018
 47. IPCC SR15, "Special Report on Global Warming of 1.5°C", 2018
 48. IPCC, 2013: Climate Change 2013: The Physical Science Basis. Contribution of Working Group I to the Fifth Assessment Report of the Intergovernmental Panel on Climate Change [Stocker, T.F., D. Qin, G.-K. Plattner, M. Tignor, S.K. Allen, J. Boschung, A. Nauels, Y. Xia, V. Bex and P.M. Midgley (eds.)]. Cambridge University Press, Cambridge, United Kingdom and New York, NY, USA, 1535 pp
 49. IEA, "CO2 Emissions from Fuel Combustion: Overview", Statistics report July 2020
 50. R. Lindsey, "Climate Change: Atmospheric Carbon Dioxide", 2020, Climate.gov
 51. Our World in Data based on BP Statistical Review of World Energy 2020
 52. R. Banos, F. Manzano-Agugliaro, F.G. Montoya, C. Gil, A. Alcayade, J. Gomez, "Optimization methods applied to renewable and sustainable energy: A review", *Renewable and Sustainable Energy Reviews* 15 (2011) 1753–1766
 53. J. Blazquez, R. Fuentes, B. Manzano, "On some economic principles of the energy transition", *Energy Policy* 147 (2020) 111807
 54. https://ec.europa.eu/info/strategy/priorities-2019-2024/european-green-deal_en
 55. P. Gabrielli, A. Poluzzi G.J. Kramer, C. Spiers, M. Mazzotti, M. Gazzani, "Seasonal energy storage for zero-emissions multi-energy systems via underground hydrogen storage", *Renewable and Sustainable Energy Reviews* 121 (2020) 109629
 56. European commission, "A Hydrogen Strategy for a climate neutral Europe", EU Green Deal 2020
 57. M. A. Qyyum, R. Dickson, S. Fahad Ali Shah, H. Niaz, A Khan , J. Jay Liu, M. Lee, "Availability, versatility, and viability of feedstocks for hydrogen production: Product space perspective", *Renewable and Sustainable Energy Reviews*, 2021
 58. M. Hermesmann, K. Grübel, L. Scherotzki, T.E. Müller, "Promising pathways: The geographic and energetic potential of power-to-x technologies based on regeneratively obtained hydrogen", *Renewable and Sustainable Energy Reviews* 138 (2021) 110644
 59. T. Wilberforce, A.G. Olabi , E. Taha Sayed, K. Elsaid, M. Ali Abdelkareem, "Progress in carbon capture technologies", *Science of the Total Environment* 761 (2021) 143203
 60. Omar Z. Sharaf, Mehmet F. Orhan, "An overview of fuel cell technology: Fundamentals and applications", *Renewable and Sustainable Energy Reviews* 32 (2014) 810–853
 61. M.B. Mogensen , M. Chen, H.L. Frandsen, C. Graves, J.B. Hansen, K.V. Hansen, A. Hauch, T. Jacobsen, S.H. Jensen, T.L. Skaftø and X. Sun, "Reversible solid-oxide cells for clean and sustainable energy", *Clean Energy*, 2019, Vol. 3, No. 3, 175–201

-
62. S. Y. Gómez, D. Hotza, “Current developments in reversible solid oxide fuel cells”, *Renewable and Sustainable Energy Reviews* 61 (2016) 155–174
 63. R. Andika, A. B. D. Nandiyanto, Z. A. Putra, M. R. Bilad, Y. Kim, C. M. Yun, M. Lee, “Co-electrolysis for power-to-methanol applications”, *Renewable and Sustainable Energy Reviews* 95 (2018) 227–241
 64. Mogens B. Mogensen, “Materials for reversible solid oxide cells”, *Current Opinion in Electrochemistry* 2020, 21:265–273
 65. K.H. Tan, H.A. Rahman*, H. Taib, “Coating layer and influence of transition metal for ferritic stainless steel interconnector solid oxide fuel cell: A review”, *international journal of hydrogen energy* 44 (2019) 30591-30605
 66. W.Z. Zhu, S.C. Deevi, “Development of interconnect materials for solid oxide fuel cells”, *Materials Science and Engineering A348* (2003) 227-243
 67. J. Wu and X. Liu, “Recent Development of SOFC Metallic Interconnect - Invited Review,” *J. Mater. Sci. Technol.*, vol. 26, no. 4, pp. 293–305, 2010
 68. R. Jain, B. Mandal, "Studies on Ideal and Actual Efficiency of Solar Polymer Electrolyte Fuel Cell", 2007
 69. A. Gebregergis, P. Pillay, D. Bhattacharyya, R. Rengaswemy, “Solid Oxide Fuel Cell Modeling”, *IEEE transactions on industrial electronics*, vol. 56, no. 1, 2009
 70. JR. Selman, "Research, development, and demonstration of molten carbonate fuel cell systems in fuel cell systems", New York, NY: Plenum Press; 1993. p.419]
 71. Y. Yang, X. Tong, A. Hauch, X. Sun, Z. Yang, S. Peng, M. Chen, “Study of solid oxide electrolysis cells operated in potentiostatic mode: Effect of operating temperature on durability”, *Chemical Engineering Journal* (2021), doi: <https://doi.org/10.1016/j.cej.2021.129260>
 72. Lenser C., Udomsilp D., Menzler N.H., Holtappels P., Fujisaki T., Kwati L., Matsumoto H., Sabato A.G., Smeacetto F., Chrysanthou A., Molin S., "Solid oxide fuel and electrolysis cells", *Advanced Ceramics for Energy Conversion and Storage* (2019) 387-547, Book Chapter
 73. M. Santarelli, "Polygeneration and advanced energy systems", Course 2019